



GEORG-AUGUST-UNIVERSITÄT
GÖTTINGEN

Atomic layer deposition of metal and metal
chalcogenide thin films and nanolaminate
composites

Dissertation

for the award of the degree

“Doctor rerum naturalium”

of the Georg-August-Universität Göttingen

within the doctoral program

of the Georg-August-University School of Science (GAUSS)

submitted by

M. Sc. Christian Volkmann

from Halle, Westf.

Göttingen, 2017

Thesis committee:

PROF. DR. SVEN. SCHNEIDER

PROF. DR. DIETMAR STALKE

(PROF. DR. GUIDO CLEVER)

Members of the Examination Board

PROF. DR. SVEN. SCHNEIDER

PROF. DR. DIETMAR STALKE

(PROF. DR. GUIDO CLEVER)

PROF. DR. INKE SIEWERT

JUN. PROF. DR. SELVAN DEMIR

PROF. DR. THOMAS WAITZ

Date of oral examination: 23.11.2017

Declaration:

I, Christian Volkmann, herewith declare that my doctoral thesis entitled “Atomic layer deposition of metal and metal chalcogenide thin films and nanolaminate composites” has been written independently with no other sources and aids than quoted.

20.10.2017, Göttingen

Sign (Christian Volkmann)

1. November 2017

Danksagung

Vor nunmehr annähernd fünf Jahren saß ich im Büro eines frisch berufenen Professors, zwecks einer eventuellen Promotion und dessen Thema. Mit einer der Situation angemessenen Nervosität verfolgte ich eine 45-minütigen Präsentation, die mir - statt des erwarteten PNP-Metall-Synthese-Themas - eine maßgeschneiderte Aufgabenstellung anbot, die vermutlich ohne jede Übertreibung als „ungewöhnlich“ in der Göttinger Chemie zu bezeichnen war. Der Brückenschlag der Ingenieursleistung einer Reaktorkonstruktion, Synthesechemie und materialwissenschaftlichen Aspekten, bis hin zur physikalischen Betrachtung von Quasi-Teilchen in hergestellten Schichten, die Möglichkeit einer Industriekooperation und Teil des großen SFB 1073 mit all dessen Vorteilen zu sein, machen meine Entscheidung für dieses Thema zu einer der Besten meines Lebens. Mein großer Dank geht daher an *Sven Schneider*, für diese wunderbare Möglichkeit, ferner für vielfältige Hilfe, eine hervorragende Forschungsumgebung und weise Ratschläge.

Für spannende Diskussionen und die Übernahme des Zweitgutachtens möchte ich Dietmar Stalke und Guido Clever danken.

Danke an Markus für die große Hilfe während meines Projektes, vor allem dem Reaktoraufbau. Christian danke ich für ein stets offenes Ohr für meine Probleme. Dalila und Frau Stückl danke ich für die Führung durch die mir nach wie vor unverständlichen Irrwege der Bürokratie.

Eine legendäre Zeit ermöglichten ferner alle Mitarbeiter: Es ist vermutlich schwierig, eine vergleichbare Gemeinschaft zu finden, in der Unterstützung, Spaß und Freundschaft in dieser Weise vorhanden sind. Danke an Markus, Arne, Jan, Schluschi, Bob und Isa, Daniel, Hufi, Christoph, Christian, Flo, Josh, Sebastian, Seb, Gleb und Katy, Suresh, Felix, Max, Richt und Lukas. Ferner alle Studenten, im besonderen natürlich Thorben, Leif und Menno, die Zusammenarbeit mit euch war großartig.

Ein besonderer Dank geht an die Korrekturleser meiner Arbeit, die mein Englisch auf ein dem Leser hoffentlich erträgliches Maß anhoben: Filip, Christoph, Torben, Jan und Arne.

This thesis originated in the time between February 2013 and August 2017 at the
Institute for Inorganic Chemistry of the Georg August Universität Göttingen.

Contents

Contents	vii
1 Introduction	1
1.1 Atomic Layer Deposition	1
1.1.1 Principles of ALD	3
1.1.2 ALD-Precursors and Properties	6
1.1.3 Oxides, Nitrides and Sulphides Grown by ALD	9
1.1.4 Metallic Films Grown by ALD	10
1.2 Design of ALD Reactors	18
1.3 Application of ALD Materials	22
1.3.1 Sandwich Layer Tuning Phonon Spectrum	22
1.3.2 Tantalum Sulfide ALD for CV-Electrode Coating	31
1.4 Motivation and Scope of This Work	33
2 Results and Discussion	37
2.1 A Novel Reactor Design for Thin Film Deposition	37
2.1.1 Design and Construction	37
2.1.2 Reactor Control: Software	43
2.2 Chamber Testing and Improvement of Depositions	51
2.2.1 Aluminum Oxide	51
2.2.2 Iridium	59
2.2.3 Platinum	64

2.3	Materials for Phonon Spectrum Tuning	69
2.3.1	Application for ALD Thin Films: Nanolaminates	69
2.3.2	Silicon Oxide Deposition	83
2.4	Precursor Development and Testing	84
2.4.1	Cobalt	84
2.4.2	Tantalum Sulphide	93
3	Summary	101
4	Experimental Methods	105
4.1	<i>In Situ</i> Analysis: EI-MS and QCM	105
4.2	External Methods	108
4.2.1	X-Ray photo-electron spectroscopy (XPS)	109
4.2.2	Transition Electron Microscopy (TEM)	109
4.2.3	Elemental Analysis (EA)	110
4.2.4	Atomic Force Microscopy (AFM)	110
4.2.5	Secondary Electron Microscopy with Energy Dispersive X-Ray Spectroscopy and Fast Ion Bombardment (SEM with EDX and SEM with FIB)	110
4.2.6	Ellipsometry	112
4.2.7	Profillometry	112
4.2.8	Scanning tunneling Microscopy (STM)	112
4.2.9	Resistivity	113
4.2.10	High Resolution Rutherford Back Scattering (HR-RBS)	113
4.2.11	Auger Spectroscopy	115
4.2.12	X-ray Powder Diffractometry and Reflectometry (XRD and XRR)	115
4.2.13	Schlenk Technique and Inert Gas Box	116
4.2.14	Nuclear Magnetic Resonance (NMR)	116
4.2.15	Thermogravimetric Analysis (TGA)	117
4.3	Chemicals	118

5	Experimental Section	119
5.1	General Preface	119
5.2	Metals	121
5.2.1	Platinum Deposition	121
5.2.2	Iridium Deposition	123
5.2.3	Cobalt Deposition	125
5.3	Oxides and Sulfides	126
5.3.1	Aluminum Oxide Deposition	126
5.3.2	Cobalt Oxide Deposition	128
5.3.3	Tantalum Oxide Deposition	134
5.3.4	Tantalum Sulfide Deposition	135
6	Appendix	139
6.1	Abbreviations	139
	List of Figures	145
	List of Schemes	149
	List of Tables	151
	Bibliography	153
6.2	List of Scientific Contributions	174
6.2.1	Patents	174
6.2.2	Publications in Scientific Journals	175
6.2.3	Oral Contributions to Conferences and Workshops	176
6.2.4	Poster Presentations on Conferences	177
6.3	Curriculum Vitae	179

Abstract

The construction of a novel “hot and cold wall, cross laminar flow multiple substrate atomic layer deposition reactor” is presented including a LabView based control program and an user-optimized graphical user interface. The chamber was successfully tested by the improvement of three different materials with respect to growth rates and impurity content by well chosen depositional parameter (AlO_x , Pt and Ir). The synthesis of a new multilayer system is introduced by forming nanolaminates made with alternating platinum and aluminium oxide ALD. These structures were probed by transient temperature-dependent reflectivity (TTR) and Rydberg atom tagging (RAT), respectively. The outstanding decrease in heat conductivity as well as the possibility of the formation of a super thin isolation layer on metals for atom scattering purposes were proven with these techniques.

Deposition experiments aiming for cobalt or cobalt oxide thin films using a new kind of precursor design within the elusive ALD procedure are discussed. Thin films are presented with growth rates comparable to the literature values, being very small. However, the examination of this procedure revealed a possible decomposition pathway prohibiting ALD.

Beyond that, an ALD strategy is investigated to generate thin tantalum oxide and the still unreported sulphide films with outstanding qualities, such as lowest roughness, unequalled mild deposition temperature and sufficient growth rates.

1 Introduction

1.1 Atomic Layer Deposition

Atomic Layer Deposition (ALD) is a gas phase deposition technique^[1] known for self-limiting, surface invariant growth of nanoscale films of outstanding quality.^[2] It was developed in the 1970s by T. SUNTOLA^[3] as Atomic Layer Epitaxy (ALE) for the growth of high-quality polycrystalline zinc sulphide thin films^[4] for electroluminescent flat panel displays. The same concept arose in the 1960s under the name “molecular layering” in the Soviet Union.^[5] Decades later, over one hundred reviews were written^[3] and more than thousand published articles per year prove ALD to be one of the most important thin film generation techniques. Especially the microelectronic industry^[6] and its demand for down-scaling device dimensions kept pushing ALD forward, including high- κ gate dielectrics for transistors,^[7] diffusion barriers for metal interconnects, and high aspect-ratio memory devices (see chapter 1.1.4).^[8,9] Furthermore, electro-catalysts,^[10] fuel^[11] and solar cells^[12] were improved by ALD materials. Today, nearly every element can be used in an ALD cycle to form metallic, oxide, nitride and carbide thin films, and also their heavier analogs, displayed in figure 1.1.^[13] Not only elemental or binary systems, but also more complex structures like phosphates or polymers^[14] can be deposited. Still, ALD is deemed as a novel method, since most of the strategies lack deeper mechanistic insights and still a variety of materials await their process discovery.

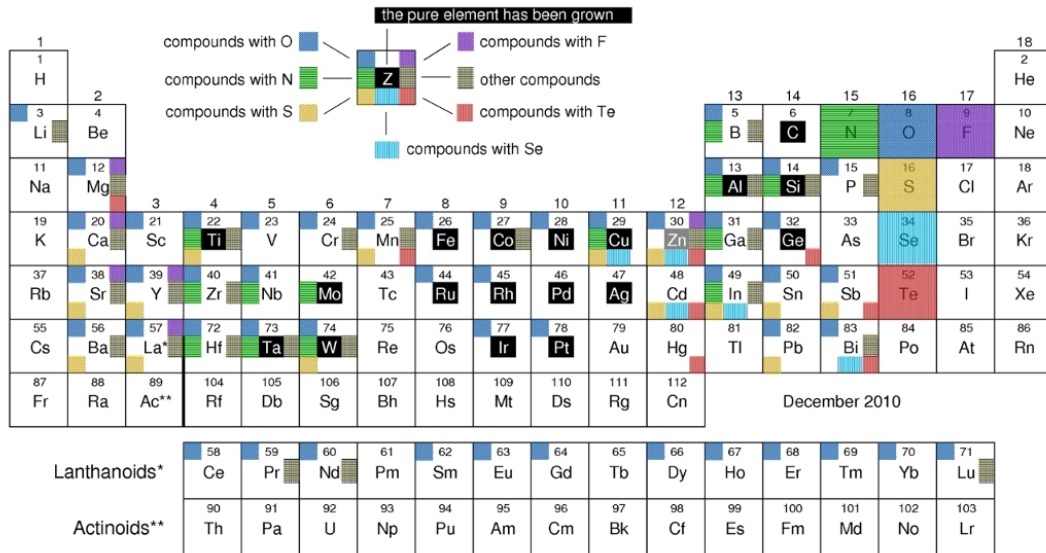


Figure 1.1: Possibilities of thin film generations with ALD for different materials, namely pure and binary compounds of O, N, S, F, Te, and Se. Adepted from MIIKKULAINEN *et. al.* with changes.^[15,16]

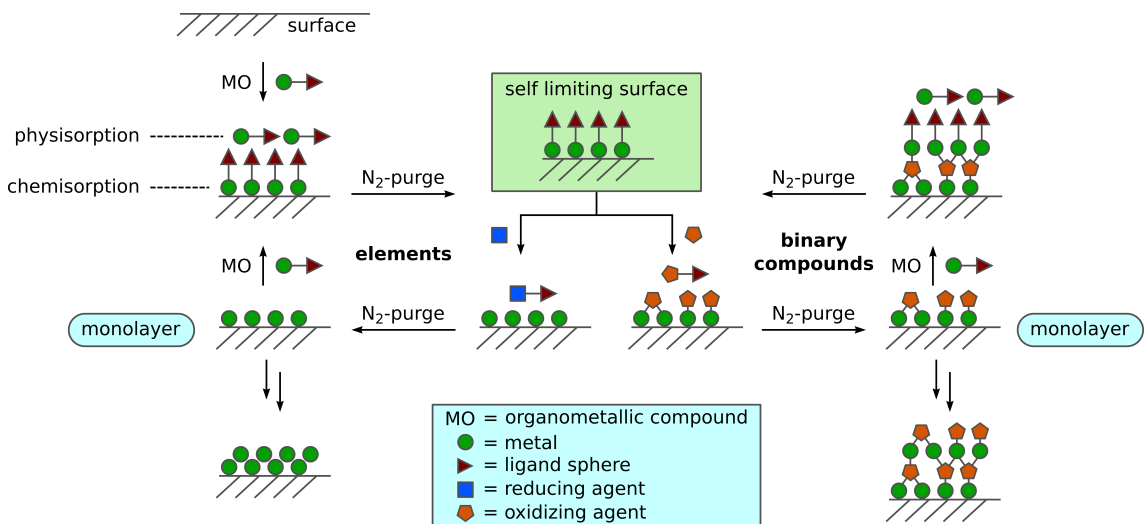


Figure 1.2: Idealized concept of Atomic Layer Deposition: The organometallic compound chemisorbs on a substrate without further decomposition. The second precursor subsequently reactivates the new surface in the next step. On the left hand side the deposition of elements like Pt and Ir is shown, as well as binary compounds like Al₂O₃ or TaS₂ on the right hand side.

1.1.1 Principles of ALD

Unique properties ascertained ALD to one of the most important thin film deposition techniques. These will be discussed using the scheme of an idealized cycle in the ALD procedure, displayed in figure 1.2. Condensing the procedure, the unique idea of ALD is the sequential pulsing of precursors, separated by a complete removal of not chemically bound compound by pump/purge procedures resulting in a pure surface reactivity.^[17]

In more detail, a generalized ALD experiment utilizes two or more precursors reacting on and with a substrate. This gives rise to a surface reaction only observed in ALD: A self-limiting mechanism can be achieved by intelligent precursor choice. Unlike other thin film preparation procedures, e.g. chemical vapour deposition (CVD), pulsed laser deposition (PLD) where precursors react in the gas phase, ALD provides a tighter control due to the reaction only taking place on the surface. As shown in scheme 1.2 in the first step, also called “half-reaction”, a metal-containing precursor is reacted with the substrate, releasing a ligand. Stable bonding of one or more remaining ligands with the metal attached to the surface prevents further reaction due to inhibited interaction between this ligand sphere and gas-phase metal precursor leading to the effect of monolayer formation with respect to the ligand. This reaction with the substrate can either be described by an acid-base or as a redox reaction. The dominating pathway is given by the product forming: deposition of elements require alteration of the precursors metal oxidation state. However, this thesis presents a concerted mechanism in chapter 2.4.1, protonation followed by redox decomposition. In both cases, a highly volatile exhaust species is formed and released from the surface.^[18]

In conclusion, ALD requires precursors, whose ligands can be cleaved via surface reactions on the one hand and form an inert cover to the gas phase on the other hand.^[19]

Although ALD is often described as a monolayer growth technique, steric effects of bulky protecting ligands prevent total surface coverage with respect to the metal.

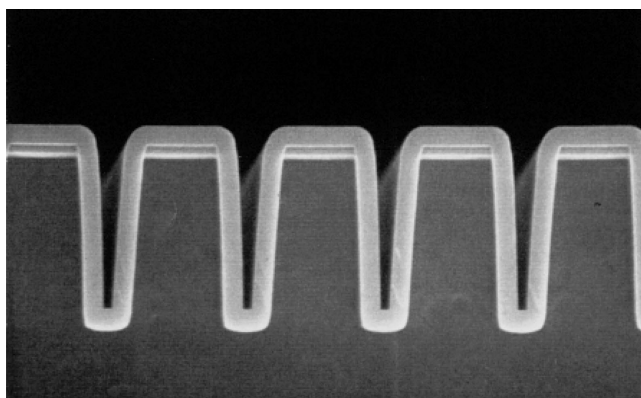


Figure 1.3: Cross sectional SEM image of an ALD film, showing perfectly surface invariant deposition: Al_2O_3 (300 nm) covers the trench structure consummately homogeneous.^[20]

Even with very small ligands like methyl (CH_3 , see 1.1.3) a maximum surface site occupation of 50 % can be reached. Most transition metals require even bulkier precursors to be stabilized (see e.g. 1.1.4) in the gas phase, reducing the “monolayer” to a 10 % active site occupation.

In particular, this self-limiting, protected surface leads to the effect that the deposition is evidently independent of kinetic aspects: while special surface sites like terrace ends, hills etc. have a higher and holes a far lower probability to be occupied in other deposition techniques, ALD is surface invariant as shown in picture 1.3. Here, the SEM image shows perfectly homogeneous ALD coverage of the comb structure with aluminium oxide (published by RITALA *et al.*, 1999).^[20] This effect is enabled, since there are no competing reactions on different surface sides in the ALD experiment. Despite easier to reach or thermodynamically more active surface atoms are also occupied first here (e.g. the top of the branch structure in figure 1.3), this reaction runs into a saturation since they are not reactivated. The occupation of remaining vacancies therefore is only dependent on precursor’s exposure duration, diffusion rate and substrate material.

In the second step of the cycle, remaining physisorbed precursor and precursors in the gas phase are purged. The small fraction of precursor used is a notable difference to other vapour deposition techniques. As the saturation of active surface sites

is slow due to decreasing amount of reaction partners and the balance of cleavage and stability of the precursors, ALD uses a fairly high quantity and concentration of the precursor in the gas phase compared to its actual deposition of molecules on the substrates. Consider the example of trimethylaluminium (TMA), reacting with a flat surface of SiO_2 with an atomic surface density of about 10^{19} atoms \cdot m⁻².^[21] Here, the amount of 0,001 g TMA would be sufficient to cover one square metre with a perfect Al monolayer. In the presented procedure (2.1.1) with an approximate chamber surface of < 0.1 m² and a use of about 0.003 mL/cycle, about 99 % of the precursor is pumped as exhaust gas in every cycle, especially considering the surface not to be completely covered. Nevertheless, this is necessary to ensure that the surface is fully coated. It has to be considered that not every collision with the surface is followed by chemical binding reaction, especially keeping in mind the increasing self-limitation.

In the third step, a second precursor re-activates the altered surface. This can be either oxidative (see chapter 1.1.4 and 1.1.3) or reductive (chapter 1.1.4) or in a ligand exchange procedure. In all cases, the terminating ligand monolayer is cleaved in this reaction. The second precursor additionally covering the surface with a reactive species to enable reiteration of the cycle. Although the second precursor (figure 1.2, blue) is disregarded in many papers, its choice has major influence on the growth conditions. Impurities with oxygen, for example, arise from too harsh oxidizing agents, while the growth of the deposited layer may be limited by the low reaction rates of ligand exchange.

The chemical control of every step in the ALD-cycle allows for perfect reproducibility of layer thicknesses in the order of Angströms, independent of precursor dose, reaction time, surface shape and temperature. Limits with respect to the precursor choice will be discussed in the next paragraph.

1.1.2 ALD-Precursors and Properties

To ensure self-limited deposition, the precursor has to fulfil different demands.^[22] The figure 1.4 shows different limitations for growth per cycle [$\text{\AA}/\text{cycle}$] (gpc) ratio in various temperatures regimes. The “ALD window”, describes a temperature range ALD can be observed (T_{\min}

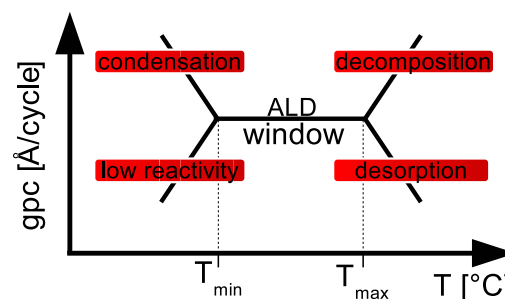


Figure 1.4: Potential growth per cycle observations in dependence of the substrate temperature.

to T_{\max}).^[23] Changing substrate temperatures to lower or higher values, two different mechanisms can be described for each limit, reducing and increasing the gpc-ratio (figure 1.4, red boxes). For lower temperatures, $T < T_{\min}$, risk of condensation and low reactivity has to be taken into account. While condensation results from the increased strength of physisorption and therefore the insufficiency to purge such bound molecules, self limitation is lost: the amount of the precursor or its fragments on the surface exceeds a monolayer. During the second precursor pulse, the deposited material quantity increases as well as impurity content due to poor diffusion into the layer. The initial ALD step, forming a saturated surface, is temperature dependent. Even though this reaction is thermodynamically favoured, the time constants for saturation may decelerate and furthermore surface mobility may be diminished.

Typical set-ups for ALD work at fine vacuum. Therefore, observed growth rate is often limited by the reduced chemical reactivity between the surface and precursor at low temperatures and not a factor of increased amounts of condensation (see 1.2),^[24] especially in precursor developing processes.

For high temperatures, $T > T_{\max}$, reactions with the hot substrate are confined by the precursor’s stability. For most cases the risk of decomposition dominates. As shown previously, precursors in between T_{\min} and T_{\max} need labile ligands for substrate bonding and stable ligands for self limitation.

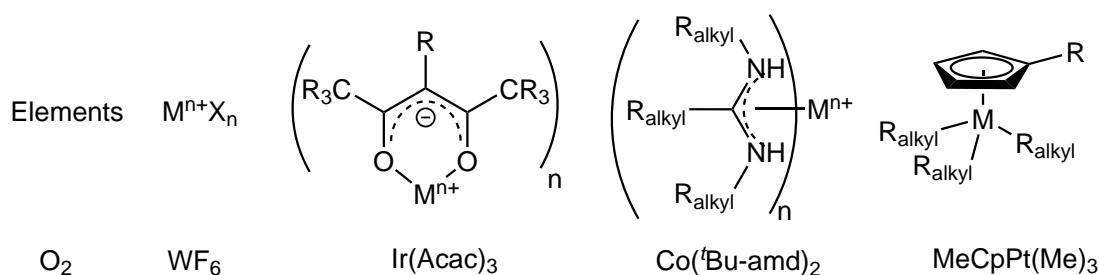


Figure 1.5: Overview of the five main ALD precursor classification by their ligand. Namely pure elements, halides, β -diketonates, amidinates and organometallic compounds with examples.^[25]

At higher temperatures these resilient ligands decompose and detach, thwarting self limitation and therefore increasing gpc. Often CVD precursors are solely used at low temperatures in ALD mechanisms, the decomposition pathway shows the well known CVD chemistry. If the compound is thermally stable, it is reflected from the surface, since bond formation is less favourable than bond cleavage. In other words, the resting time, limited by desorption is too small for ligand exchange reactions.

Another important aspect of temperature dependency is not reflected by figure 1.4, which is a fundamental alteration of reactivity. Mainly observed in metal deposition studies, there may be a crossover-point at which e.g. the oxide is formed instead of pure metal. Thermal ALD^[26] of platinum is a prominent example using $\text{Pt}(\text{Acac})_2$, where a temperature drop of the substrate to 140 °C result in PtO_x deposition with increased gpc.^[27] In general, an ALD precursor need to exhibit a variety of tailored properties, namely a compromise of stability, reactivity and volatility. Using common CVD precursors, reactivity is the challenging part, whereas volatility and stability in gas phase have been proven by CVD experiments. As implied previously, the interaction with the substrate surface and the reaction of stable ligands with the second precursor are the two vital reactions. The change from CVD to ALD behaviour is mainly obtained by the exchange of ligands or shift in metal oxidation state, retaining volatility and stability.^[28]

In literature, ALD precursors are categorized by their ligands in the displayed five groups (figure 1.5) ranging from highly symmetric early arrangements, like pure el-

ements, metal-halides or beta-diketonates to novel true organometallic or nitrogen containing antisymmetric metal organyls.

Lower evaporation temperatures are achieved by lowering of symmetry and a heterogeneous ligand sphere, which gives rise to a broader ALD window because of distinct cleaving behaviour with respect to surface reactivity.

1.1.3 Oxides, Nitrides and Sulphides Grown by ALD

Since the mechanism of binary compound deposition inhibits surface reactivation half-cycle by nature, these materials constitutes by far the largest group. In this work, they will only be described theoretically but can be reviewed in the PSE-figure 1.1 or in many overview articles.^[29,30]

Most binary materials show “Frank-van-der-Merwe”-growth^[31,32,33] featuring perfect layer by layer bottom up generation, only limited by the sterical hindrance of precursor ligand size, blocking surface sides. This already results in complete substrate coverage after very few deposition cycles, very low roughness and minor impurities. Oxide depositions can generally be run at lower temperatures, since there is no decomposition step involved. Therefore, the use of smaller precursors is accessible, increasing the monolayer coverage and gpc-rates of binary compounds compared to elemental depositions. Additionally, the gpc-rate is affected by the simple fact, that two atoms are deposited per surface site and cycle. Furthermore, due to the evidence of a low annealing process due to low deposition temperatures and open surface sides on the basis of sterics, binary compounds often are amorphous and lower in density compared to crystallized compounds (density of e.g. Al_2O_3 films is 3.0 g/cm^3 using Atomic Layer CVD^[34] and 3.5 g/cm^3 ^[35] with ALD, which is lower than the standard bulk density of 3.96 g/cm^3 in sapphire). The deposition of Al_2O_3 ^[20,36] often acts as a model system in various reviews and is studied intensively.^[15,37,38] The combination of a well understood system forming layers with interesting properties for further investigations, fast growth rates with cheap and volatile precursors renders a perfect candidate for test depositions in the novel set-up described in chapter 2.1.1.

1.1.4 Metallic Films Grown by ALD

ALD turned out to be the most promising technique generating conductive films, which is especially of interest for microelectronic devices^[39] and their demand for downscaling components, e.g. for nanocapacitors or metallization diffusion barriers.^[40] Still, as mentioned before, ALD of metals is more challenging due to their complex surface reactivation. While oxide surfaces are reactivated by means of their nature, the reaction of a metal precursor and its oxidized gas phase state undergo a variety of oxidation state changes, where the catalytic property of the metal plays a vital role e.g. in dissociatively adsorbed oxygen reactions.^[26] Metallic films can be deposited either by “thermal-”, “plasma-enhanced (PE)-”^[41] and “low-temperature” ALD. Mainly noble metals are deposited via thermal ALD: HÄMÄLÄINEN *et al.* collected precursor, deposition parameter and much more in a comprehensive review,^[26] a summary is displayed in figure 1.6, namely for Ru,^[42,43,44] Rh,^[45] Os,^[46] Ir^[47,48] and Pt.^[49] An overview of surface chemistry, predictions and calculations is given by ELLIOT.^[40]

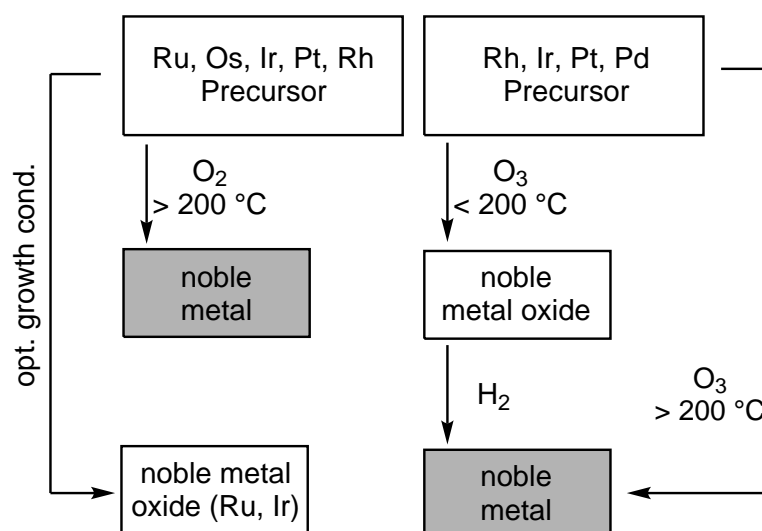


Figure 1.6: Flow chart of noble metal procedures in thermal ALD.^[26]

Another unique feature of noble metal deposition is a different initial phase be-

behaviour on oxide substrates. Due to the major difference in lattice constants, the adhesion is expected to be low. Therefore surface mobility is high and single atoms of the metal merge to larger droplets after reactivation and ligand cleavage during the oxygen pulse. This is further supported by the high deposition temperatures.

This growth is named “Volmer-Weber-wetting”,^[51]

although this model only describes the adhesion difference of substrate and film but no thermodynamic aspects of wetting, it can be applied to most noble metals. As a result of this growth behaviour, different rates can be found if one

compares the growth on pure oxides (first cycle)

with the growth on accreted nanoparticles. As a

consequence of true “Volmer-Weber wetting”,^[51]

where only binding to nanoparticles is possible,

the virtual growth can be delayed by several cy-

cles as depicted in figure 1.7. In contrast to this, early transition metal’s negative electrochemical potentials do not allow the use of oxidizing agents due to the immediate formation of oxides instead of dissociative adsorption at ALD temperatures (especially for Fe, Mn, Cr, V and Ti).^[25] Therefore, this procedures demand reducing

agents. A few metals that can be used for ALD are shown in a scheme in figure 1.8, while no procedures for vanadium and chromium have been documented yet. Es-

pecially hydrogen gas leads to successful deposition but still most temperatures do not allow for the use in layered structures necessary for applications: diffusion in

between layers is still a major problem constructing e.g. interconnects in transistors, seed layers etc. with ALD.^[70] For various metals GORDON and coworkers could

show the possible use of homoleptic *N,N'*-dialkylacetamidinato metal compounds together with H₂ forming metallic nano-islands but still with negligible gpc-rates of about 0.2 Å.^[62]

Nevertheless, further indirect routes have been published, in which the grown oxide

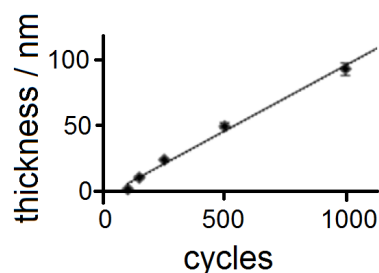


Figure 1.7: Example of a 100 cycle initiation phase during cobalt deposition with bis(1,4-di-*t*-butyl-1,3-diazabutadienyl)cobalt and formic acid, shown by WINTER and coworkers.^[50]

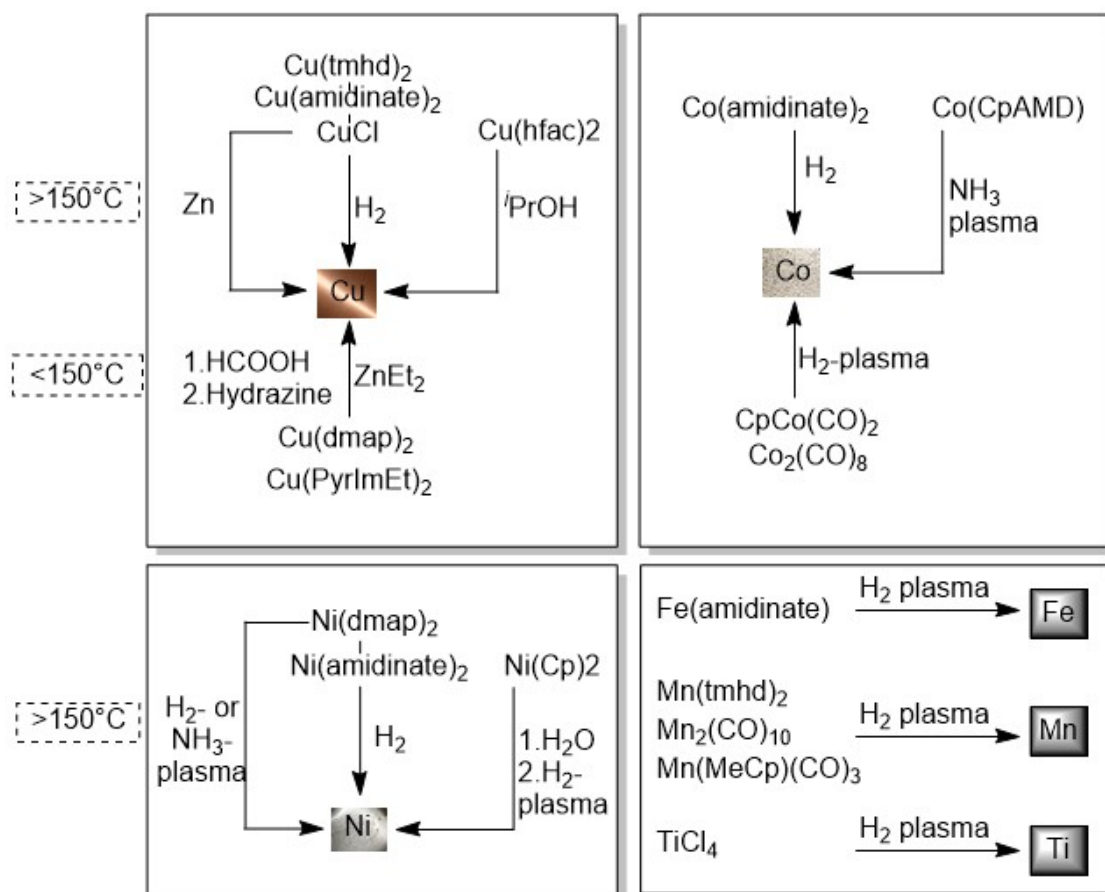


Figure 1.8: Display of direct third row transition metals ALD for various metals. Structural features have been discussed in figure 1.5.

For **Copper** with $\text{Cu}(\text{tmhd})_2$ (tmhd = 2,2,6,6-tetramethyl-3,5-heptanedionate) at $190\text{--}260^{\circ}\text{C}$ ^[52], $\text{Cu}(\text{amidinate})_2$ (Amidinate = *N-N'*-di-*sec*-butylacetamidinate) at $150\text{--}250^{\circ}\text{C}$ ^[53,54], $\text{Cu}(\text{hfac})_2$ (hfac = 1,1,1,5,5,5-hexafluoroacetylacetonate) at 300°C ^[55], $\text{Cu}(\text{dmap})_2$ (dmap = 3-dimethylamino-2-butoxide) at $100\text{--}120^{\circ}\text{C}$ ^[56,57] or with 3-step ALD at $100\text{--}160^{\circ}\text{C}$ ^[58] and $\text{Cu}(\text{PyrIm})_2$ (PyrIm = *N*-ethyl-2-pyrrolylaldiminato) at $120\text{--}150^{\circ}\text{C}$ ^[59].

For **Nickel**, $\text{Ni}(\text{Cp})_2$ (Cp = cyclopentadienyl, C_5H_5) at 165°C ^[60], $\text{Ni}(\text{dmap})_2$ is used at $200\text{--}240^{\circ}\text{C}$ ^[61] and $\text{Ni}(\text{amidinate})_2$ at 250°C ^[62].

For **Cobalt**, $\text{Co}(\text{amidinate})_2$ is used at 350°C ^[62] as the only thermal and $\text{Co}(\text{CpAMD})$ (cyclopentadienyl isopropyl acetamidinato)^[63] $\text{CpCo}(\text{CO})_2$ and $\text{Co}_2(\text{CO})_8$ at $125\text{--}175^{\circ}\text{C}$ and 100°C ^[64] as plasma enhanced ALD procedures respectively.

For **Fe**, **Mn** and **Ti**, only plasma amplified procedures are known^[65,66,67,68,69].

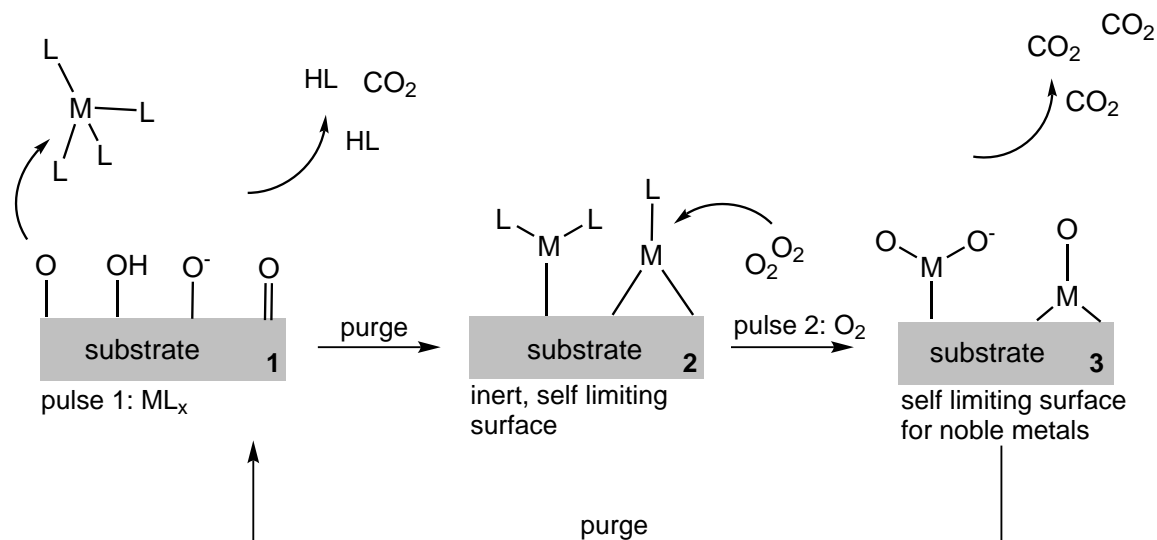


Figure 1.9: The general mechanism of a noble metal deposition with reference to the reproduced material in this work. **1:** Reaction with the surface consisting of different oxygen sites being protonated or basic releasing Ligand or CO₂ depending on reaction pathway. **2:** self-limiting ligand protected surface after purge phase. **3:** Ligand oxidation and reactivation of the metal surface. For metallic surfaces dissociative chemisorption of oxygen.

is reduced by isopropanol or formalin^[71] and hydrogen gas^[72] in case of copper at much higher temperatures. Furthermore, formic acid can act as a reducing agent supported by metallic substrates that facilitates the pre-activation to H₂ and CO^[73] which may allow access for elusive metal deposition in future.

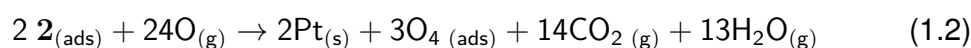
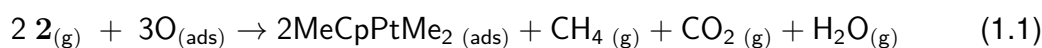
In this thesis three metals were deposited, namely platinum (2.2.3) and iridium (2.2.2) using thermal ALD and cobalt (2.4.1). As displayed in figure 1.9, MeCpPtMe₃ and Ir(Acac)₃ were used together with O₂ as model systems for high temperature noble metal deposition using a highly and weakly volatile precursor, respectively. With these materials, it was possible to evaluate the limits of the novel set-up of the deposition chamber. Especially platinum was subject of many studies and half reactions were investigated comprehensively. Therefore, platinum may act as a model providing deeper insights in the mechanistic of noble metal ALD and will be discussed in the next chapter. With a novel route for Co deposition utilizing a highly moisture sensitive Co(NTMS₂)₂PR₃ complex the chamber was tested with respect to oxygen contribution.

Platinum

Platinum ALD, as invented by AALTONEN *et al.*^[49] uses the CVD precursor MeCpPtMe₃ (**2**) and oxygen alternately pulsed onto a 300 °C substrate.

This procedure is amongst the most widely applied and studied processes and can be considered a model

system for noble metal ALD based on chemisorped surface oxygen.^[77,78] Furthermore, it stands for the exclusively completely understood noble metal ALD mechanism. The growth rate is reported to be about 0.5 Å per cycle comparable with other noble metals. Whilst twelve years of intensive usage, the pathway remained unclear as displayed in figure 1.10: [A] claims the partial oxidation by surface activated oxygen and is limited by this amount. The finding of a strong dependency of gpc-rates on surface temperature lead to this suggestion, because the amount of oxygen on elemental platinum is temperature dependent.^[40,75,79] This finally results in the observation of no platinum forming for temperatures lower than 200 °C^[78,80]. In more detail, KESSELS *et al.*^[75] defined a possible pathway, describing the nature of self-limiting mechanism:



where equation 1.1 denotes MeCpPtMe₃ pulse and equation 1.2 O₂ dose. This was derived from the intensity of exhaust gas, most importantly by the release of one equivalent of carbon atom per MeCpPtMe₃ as CH₄ and CO₂ in a 1:1 ratio while O₂

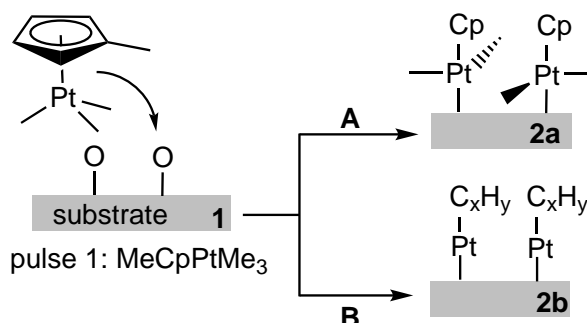


Figure 1.10: Discussed Platinum ALD self-limiting mechanisms using thermal ALD with **2** and O₃^[74] imaging pathway presented by KESSELS (**A**) and MACKUS (**B**).^[75,76]

releases the remaining 87 % by combustion. This was furthermore backed with quartz crystal microbalance (QCM) investigations, confirming the majority of mass loss occurs in the O₂-step^[81] although the detected exhaust-gas-ratio is significantly different.

The second pathway [B] claims the saturation driven by dehydrogenation of MeCpPtMe₃ and the formation of partially dehydrogenated carbon saturation layer. This was derived from previous reactions on platinum: In this description the adsorbed oxygen reacts with MeCpPtMe₃ as in [A], but then reacts further to form a growth inhibiting hydrocarbon film.^[76] The existence of unidentified carbon chains supporting [B] were detected by BENT *et al.* with *in situ* Photoemission Studies (PES), observing broad bands for the carbon 2 s region.^[74,82] While sometimes analytical approaches did contradict each other, [B] remains mostly accepted nowadays.^[77]

Nevertheless, the described pathways are futile to delineate initial steps, growing platinum on oxide substrates. It is observed that nanoparticles are grown by “Volmer-Weber growth”^[51] which can be related to different surface energies or the simple absence of catalytic metallic platinum may play a role since nanoparticles were observed in plasma enhanced ALD (PEALD) and ABC-type ALD using **2**, O₃ and H₂ respectively. KESSELS *et al.* got insights of first step mechanism recently, using *in situ* Fourier transform IR (FTIR) measurement confirming C_xH_y species after the pulse of **2** only on pure Pt, Pt-OH after oxygen exposure and a Langmuir-Hinshelwood process of CO reacting with Pt-O(H) to CO₂ forming metallic platinum.^[77]

As mentioned previously the thermal growth was extended by different platinum sources (Pt(Acac)₂^[83]) with slightly higher growth rate (0.6 Å per cycle) using bulkier ligands which was assigned to the lower valency of the metal^[40]. The utilization of ozone allowed for platinum oxide deposition.^[83] Furthermore, three step ALD utilizing a reductant and PEALD offer deposition temperatures below 200 °C.^[84]

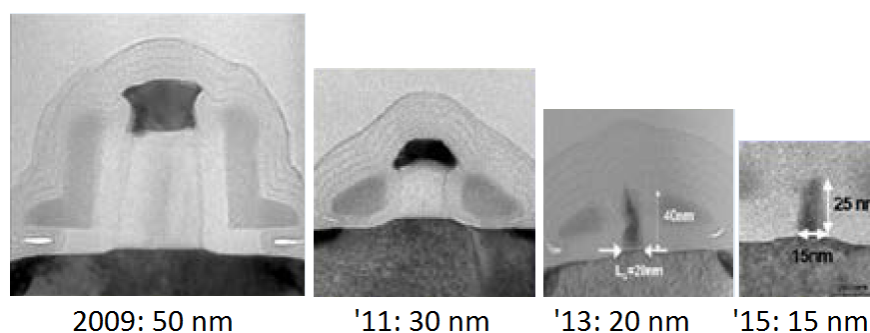


Figure 1.11: SEM image showing the size of a transistor developing in the last years.^[85]

Cobalt

Metal deposition is more challenging than their corresponding oxide precipitation and some applications demand for still elusive materials. An example for this turned out to be a cobalt or nickel layer for microelectronic devices. These layers in transistors are mainly made with physical vapour deposition (PVD) reaching a limit for smallest device possible at around 17 nm, as shown in figure 1.11. Following “Moore’s Law” shrinking feature size to even lower dimensions, keeping the same or even higher performance is a challenge only ALD can address.

In cooperation with BASF (Ludwigshafen am Rhein, Germany) we decided to improve the Co or Ni diffusion barrier in between conducting tungsten and silica in transistors by means of their thickness. Nowadays, this is still performed by Ni-sputtering followed by rapid annealing forming the NiSi barrier, although the coverage of this high aspect structure formed by the SiO₂-mask demand for a surface invariant technique like ALD. Since tests using the CVD Co(Acac)₂ precursor^[86] together with hydrogen turned out not to be successful, the expansion of the ALD toolbox using a novel strategy is essential. Since the start for this project three years ago, a strategy for Co-ALD arose. A variety of ALD procedures, showing very low growth rates in the range of < 0.01 nm were reported recently, using Co(ⁱPrNCMeNⁱPr) and H₂ or NH₃^[62,87,88,89]. Co((Me)(ⁱPr)COCNtBu)₂ and BH₃(NHMe₂) at 180 °C show comparable growth rates^[90]. Yesteryear, WINTER and coworkers published acceptable growth rates (0.95 and 0.98 Å/cycle) using bis(1,4-di-tert-

butyl-1,3-diazabutadienyl)cobalt(II) and formic acid with optional 1,4-Bis-(trimethylsilyl)-1,4-dihydropyrazine as precursors within an ALD-window of 170-180 °C.^[50,91] Our approach was based on well known cobalt hydride properties and the metal's behaviour on coordinating ligands with α - or β -hydrogen atoms. Investigated as a decomposition mechanism already twenty years ago, it was found that Co undergoes α - or β -hydrogen elimination,^[92] forming a Co-hydride intermediate which rapidly decomposes to Co nanoparticles. Based on this chemistry, in our approach, shown in scheme 1.4.1, we transformed a stable Co-ligand self-limiting surface (result from step A) via ligand exchange within the second pulse to an unstable intermediate. This is proposed to primarily form a metal layer and can be reactivated to interact with next-step gas phase metal-organic compounds (result from step B). Neglecting surface activation chemistry as shown in chapter 1.3.2 this is one of the first approaches of metal ALD incorporating complex reactivity of the utilized molecules.

1.2 Design of ALD Reactors

ALD-reactors are generally classified by their flow condition. Two limits are defined in literature^[24] by vacuum and flow condition: early reactors often expose substrates to the ALD precursor without carrier gas and pumping. In the first chambers, a revolving sample holder rotates the substrate through two cells, filled with reactant gas and optimally in-between purge cells^[4] as shown in figure 1.12, but later more simple

single chamber reactors with alternating pulse- and pump-times were constructed.^[93,94,95] This

leads to the benefit of very long exposure and

reaction times of the surface with a high concentration of the precursor in the gas phase. However, the evacuation time to remove gas phase remainders is found to be very long since the molecule flight trajectory is merely undirected at low pressure.^[24]

Therefore, most chambers are run with a carrier gas flow of Ar or N₂, shortening cycle times by orders of magnitude.^[96,97,98] Usually, a gas flow of about 100 standard cubic centimeter per minute (sccm), generating a background pressure of one Torr, which results in an approximate interdiffusion value of $D = 132 \text{ cm}^2 \cdot \text{s}^{-2}$ at 273 K for O₂ in N₂ since diffusion is inversely proportional to the pressure^[99]. This calculates the mean squared displacement (MSD) x , using $\langle x^2 \rangle = 6Dt$, where t is time, to $x = 28 \text{ cm}$ in 1 s indicating sufficient removal properties in acceptable time. Although this approximation comprises vague assumptions, values can act as limits since interdiffusion of disparate molecules is slower.

Since the optimum vacuum parameters are mainly a trade-off between the described maximized interdiffusion and entrainment, the mean free path (λ) has to be consid-

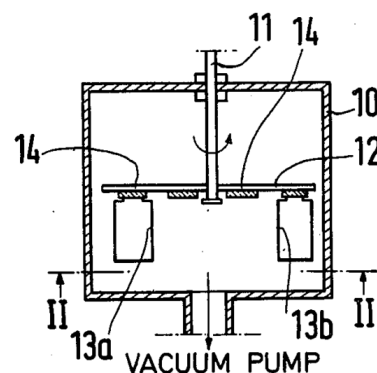


Figure 1.12: First ALD chamber rotating (11) two substrates (12/14) in a vacuum chamber (10) exposing them to precursor gas in separate evaporation cells (13a+b).^[4]

ered as small as possible. For one Torr this can be calculated to $\lambda \approx 50 \mu\text{m}$.^[100]

However, applying laminar flow condition reduces the need for interdiffusion drastically and allows for higher pressure set-ups. Although macropores e.g. in structured substrates still need diffusional purging, flat surfaces can be coated faster in the idealized image of certain flow domains in the scale of the precursor's pulse time, carrying precursor molecules without mixing/propagation. Since $D \sim p^{-1}$ in a cylindrical flow tube, Reynolds number (R_e) gives an impression whether flow can be laminar, being the fraction of inertial and viscous forces^[101]:

$$R_e = \frac{\rho \cdot u \cdot L}{\mu} \stackrel{\text{tube}}{=} \frac{Q \cdot D_H}{\nu \cdot A} \quad (1.3)$$

where ρ is the density, u (Q) is the velocity (volumetric flow rate), μ (ν) is the dynamic (kinematic) viscosity of the fluid and L is a characteristic linear dimension, e.g. the dimensions of a tube like the hydraulic diameter D_H and its cross section area A . Low pressure changes the density of the fluid and heating its viscosity. The stream is considered laminar when $R_e < 2300$, transient when $2300 < R_e < 4000$ and turbulent when $R_e > 4000$. Applying the ideal gas law the density can be approximately determined to $\rho \approx 1.3 \text{ g} \cdot \text{m}^{-3}$, $Q \approx 100\text{-}200 \text{ cm}^3 \cdot \text{s}^{-1}$ as described previously and D_H and A are in the range of cm. Dynamic or absolute viscosity is mainly a function of temperature (the kinematic viscosity increases with higher temperature) and pressure increase by orders of magnitude shows a less than 10% effect on viscosity correction and can be discarded^[102]:

$$\mu_T \approx \mu \cdot \left(\frac{T}{T_0} \right)^m \Big|_{-200 \text{ }^\circ\text{C to } 500 \text{ }^\circ\text{C}} \quad (1.4)$$

with $m = 0.76$ for air and

$$\mu_T \approx \frac{\nu_T}{\rho} \quad (1.5)$$

The increase of temperature, diameter and pressure (density) reduces R_e while an increase of flow rate increases it. The novel ALD reactor, described in chapter 2.1

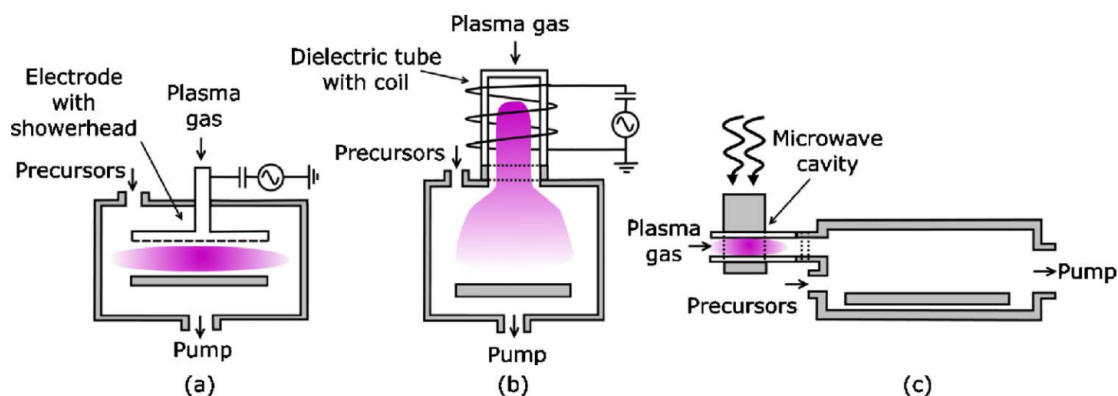


Figure 1.13: Schematic representation of the three different types of plasma-assisted atomic layer deposition reactors that can be distinguished: (a) direct plasma, (b) remote plasma, and (c) radical enhanced.^[105]

with corresponding R_e for different experiments, was built and operated, following the before mentioned motives.

Special chambers, addressing the problem of long residence time, can be found in literature: novel synchronously modulated flow and draw (SMFD)-reactors were constructed altering the flow direction of the inert gas stream by injecting the carrier gas before the substrate during purge mode and behind in pulse mode with continuous pumping. This leads to high relative exposure times and low flow speed combined with fast cycle times of less than a second for well understood systems.^[103] Similar flow condition can be found in inductively coupled plasma (ICP)-chambers where often a carrier-free plasma pulse is followed by a normal metal-organic ALD half-cycle (e.g. $TaCl_5$ or $TiCl_4$) with inert gas usage.^[67,104] Large scale commercial PEALD reactors operate with H_2 , N_2 , O_2 , SF_6 , N_2O , and NH_3 plasma at pressures of approximately 100 mTorr and various metals nowadays.^[105]

As furthermore presented in figure 1.13, the gas flow direction, relative to the substrate surface can act as classification argument: thus “*showerhead*”- (guiding the gas stream perpendicular to the substrate plane, often with the use of a distributor plate, figure 1.13 (a+b)) and “*cross-flow-chambers*” (c) (leading reactants sideways onto the substrate surface). “*hot-*” and “*cold-wall*”-reactors discriminates between chamber and substrate heating.^[24]

In Situ Methods

An increasing number of chambers features *in-situ* analysis for different purposes and beside vacuum, flow and heating this can act as a classification argument. Measuring the film's thickness increase can be calculated by mass gain with QCM^[106,107], but also spectroscopically using spectroscopic ellipsometry (SE)^[108,109], X-Ray photoelectron spectroscopy^[110], ultraviolet photoelectron spectroscopy (UPS)^[111], X-Ray fluorescence (XRF)^[82,112], or more accurate synchrotron radiation photoemission spectroscopy (SR-PES)^[113] are methods presented in literature. Characterization of surface, interface, and thin film structure and morphology can be applied by low angle electron-electron diffraction (LEED)^[114] or X-Ray reflectometry (XRR)^[115] can be used to study layered growth revealing micro-structures whereas grazing incidence (GI)-small angle X-ray scattering (SAXS)^[116,117] is especially sensitive to the formation of discrete nano-particles, and therefore particularly useful in investigating nucleation, growth, and coalescence of nano-particles during the early stages of ALD growth X-ray absorption spectroscopy (XAS)^[82,116]. Furthermore, the evidence of film closure afterwards can easily be detected by four-point probes electronic resistivity investigation^[118]. Measurements like X-ray absorption near-edge spectroscopy (XANES) and X-ray absorption fine structure (XAFS) provide information regarding the oxidation state, ligand influence on orbital environment, and symmetry of the probed atom^[116]. Surface molecules like ligand fragments or their reaction products can be additionally detected by FTIR^[77,106,119,120,121,122] or surface-enhanced Raman spectroscopy (SERS)^[123], gas phase fragments by mass spectrometry (MS)^[124,125], resulting from surface reactions, or optical emission spectroscopy (OES)^[126] and can thereby give insight in mechanistical properties. Thermodynamics of a half cycle reaction have been investigated by calorimetric heat detection^[127] and theory providing insights of reaction pathways and continuation in precursor improvements.^[128] tunable diode laser absorption spectroscopy (TDLAS)^[129] is used as a mass flow control unit to guaranty for a highly reproducible precursor inlet.

1.3 Application of ALD Materials



1.3.1 Sandwich Layer Tuning Phonon Spectrum

Fundamental understanding of atomic-scale energy transport in different materials is the key aim of the CRC 1073 “atomic scale control of energy conversion” with the long term goal to develop control tactics steering energy conversion via tunable excitations and interactions. A variety of methods is applied, dichotomously split into material generation and investigation of their properties. This allows for the development of novel theoretical and experimental methods to precisely control for example thermal energy transport, important in multiple research fields, including highly efficient thermoelectrics^[130,131], nanoelectronics,^[132] fuel cells,^[133] thermal barrier coatings,^[134] and ultra-low thermal conductivity materials^[135] and much more described by MALDOVAN.^[136]

Generally, energy transport in condensed matter is driven by free electrons (only in metallic structures) and phonons. In an elastic arrangement of atoms (solid state and special liquids), a phonon is defined as an excited state of lattice vibration and can be understood as a bosonic quasi-particle in a wave–particle duality fashion. Energy transport can furthermore be understood as phonon propagation through the material and reduction of the thermal conductivity can only be achieved by the reduction of phonon velocity or its mean free path as a consequence thereof. This reduction is driven by scattering of phonons which happens by different pathways (see equation 1.6), reducing the lifetime τ resulting in a propagation length of about 10-100 nm (at room temperature (rt)).^[137] Phonon-Phonon interaction in which two phonons merge to one or one phonon decays in two (conservation of momentum) cannot explain the finite thermal resistance. Therefore, diffuse boundary scattering τ_B , dominating at low T with low frequency phonons, impurity scattering τ_I , and Umklapp scattering τ_U at higher temperatures have to be taken into account. The

overall relaxation time τ can then be expressed as

$$\frac{1}{\tau} = \frac{1}{\tau_B} + \frac{1}{\tau_U} + \frac{1}{\tau_I} \quad (1.6)$$

It has been proven experimentally that τ and thus phononic thermal conductivity can be artificially changed, dependent on the materials temperature: doping materials with impurities^[138] scattering short wavelength phonons, interfaces^[135], and nanoparticles^[139] scattering longer wavelength phonons diffusely (incoherent)^[140] as nicely depicted by VINEIS *et al.* (figure 5 in^[139]), lead to this effect. Introducing phonons, it may be stated at this position, that the Debye temperature Θ_D for Al_2O_3 is 1047 K^[141], whereas Θ_D is 240 K for platinum.^[141] However, this work will focus on phonons in nanolaminates in which boundary scattering dominates if the lattice fulfills parameters discussed in the next paragraph.

In superlattices, thermal transport can be varied by the materials chosen, mainly the acoustic mismatch (crystallinity, density, mass of elements, roughness...) at the interface, by the periodicity of the lattice and by the layer spacing dimension. As displayed in figure 1.14, surface roughness and periodicity of the multilayered structure define the pathway of scattering: An interface roughness that fulfills $d > R$ and a periodicity satisfying Bragg's law, leads to constructive interference ($\hat{=}$ no transmission due to total energy reflection). Especially for nanolaminates of $r_L \gg P$ (with $r_L = v \cdot \tau$ where v is the group velocity and τ the phonons lifetime limited from scattering), allowing for multiple secondary wave reflections.^[136] The group of this d is then defined as the "bandgap".^[142] This is naturally broadened, taking aperiodic lattices into account (see figure 2.26). As the second property, the periodicity of the lattice defines two limits for the heat transport, namely the incoherent diffuse regime and the coherent ballistic limit. Considering a phonon mean free path r_L being much shorter than the lattice parameter P , scattering occurs both in between and at the interfaces (As shown in figure 1.14 B) and phonons should be treated as particles.

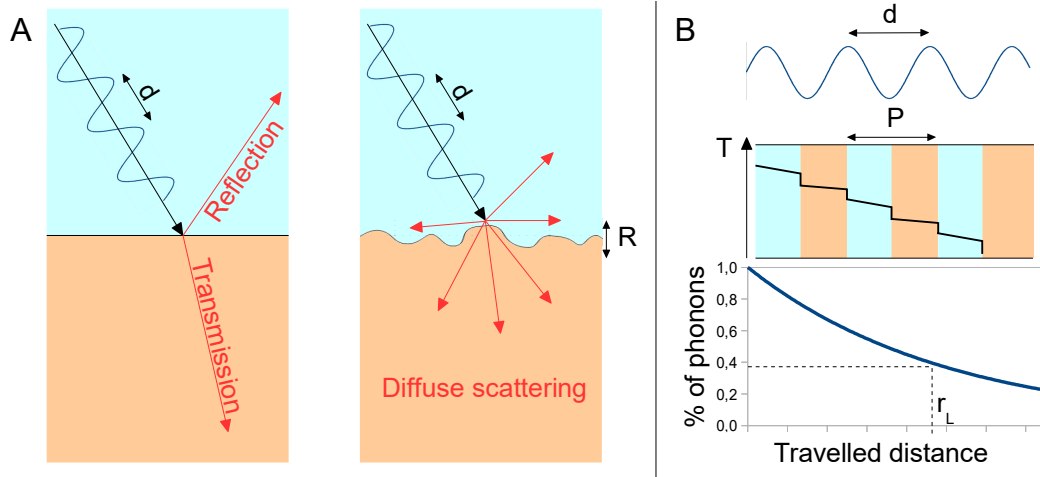


Figure 1.14: [A]: Specular versus diffuse scattering at the interface of two materials (black line): for $d > R$ thermal vibration maintain its phase, is reflected and transmitted into the second material. For $d < R$ diffuse scattering dominates. [B]: Phonon mean free path r_L in a layered material and resulting energy transport displayed as temperature in the diffuse scattering model.^[136]

If $r_L > P$, then ballistic transport is dominating and the phonon has to be treated as a wave.^[143] Since temperature and phonon frequency influence the ratio, both models have to be considered in a real system.^[144]

Although the scattering in between layers can be derived from bulk properties, the treatment of interface influence is challenging and intensively discussed in literature: Considering a phonon wave incidence perpendicular to an interface (surface), the energy or heat flux (J_Q) through this junction, with a boundary conductance G is^[145]:

$$J_Q = G \cdot \Delta T \quad (1.7)$$

G can be predicted by the acoustic mismatch model (AMM) (perfect interface, no scattering^[140]) and diffuse mismatch model (DMM) (all phonons scatter^[146]) respectively, both originally only taking phonons into account, ignoring electrical contributions (e.g. in metals) relying on sound velocity ν and density ρ ,^[147,148,149,150] which is also related to Young's modulus.^[151] Overall the phononic density of states on each

side A and B give the scattering probability proportional to the mismatch,^[152]

$$t_{A \rightarrow B} = \frac{4 \cdot Z_A \cdot Z_B}{(Z_A + Z_B)^2} \quad \text{with} \quad Z = v \cdot \rho \quad (1.8)$$

where Z is the acoustic impedance. Calculations predict thermal conductivity in cross plane to be about ten times smaller compared to bulk material^[153] but is limited as a function of atomic layers per superlattice layer.^[154] Further experimentally proven factors are tunnelling^[155], mode conservation^[156] or the formation of phonon minibands, in which phonons transmit across interfaces with high probability but with reduced group velocity^[157], that can lead to an increase of conductivity Λ with smaller P which was both proven^[158] and refuted^[159] on similar materials. This describes exquisitely how poorly the understanding of energy transport is.

For materials with small heat carrying phonon wavelength, e.g. metallic silicon ($d \approx 1 - 10 \text{ nm}^{[160]}$), bandgaps become measurable with ten interfaces (e.g. in Si/Ge^[161]) defining the bottom line of possible materials. Experimentally intensively studied, since heat transfer is only driven by phonons, are superlattices mixing two insulators. Recently, metal-metal^[162] interfaces were studied (Pd/Ir interfaces show linear regression in double logarithmic scaling and the boundary conductance perfectly fulfils the DMM^[163]), as well as metal-insulator laminates.^[164]

Generation of Superlattices and Conductivity Measurement

Since there are a lot of thin film generation techniques, such as PLD, CVD, sputtering and so on, the following paragraph will focus on the outstanding possibilities, only provided by ALD, based on the theory in the previous chapter. As stated here, thickness, roughness, density and atomic weight mismatch as well as impurities influence phononic heat conductivity. In this work, the first superlattice with metal-insulator interfaces by ALD both with periodic and aperiodic periodicity is presented. The generated laminates consist of Al_2O_3 and platinum, leading to a huge mismatch in atomic weight. Furthermore, the presented platinum layers show highly ordered crystallinity parallel to phonon propagation while Al_2O_3 is amorphous. This leads to a huge mismatch at the boundary site. Due to the deposition mechanism, discussed in chapter 1.1, the interface is expected to consist of chemical bondings between both materials, which is an unique feature of ALD. Furthermore, the roughness of ALD-layers can be very different depending on the chosen material. Especially metallic interlayers form quite rough surfaces due to the previously described island growth. However, oxide surfaces often turn out to be atomically flat, where $d > R$ may always be the case (figure 1.14). Impurity scattering like isotope scattering, due to three platinum isotopes cannot be excluded as well as boundary scattering at platinum grain boundaries perpendicular to the metal-insulator interface. Although ALD reproduces the stoichiometry of oxides far better than most other techniques, their density is often lower than single crystalline Al_2O_3 leading to layer defects but also to a larger density mismatch and therefore different phononic density of states decreasing G .

This effect is measured in a cooperational project within the CRC 1073 with transient temperaturedependent reflectivity (TTR) by Florian Döring.^[165] TTR is a frequently applied technique on a variety of structures but this work can present the first example of ALD-deposited multilayers investigated by TTR. As depicted in figure 1.15, a probe laser continuously measures the fraction of 643 nm light absorbance and

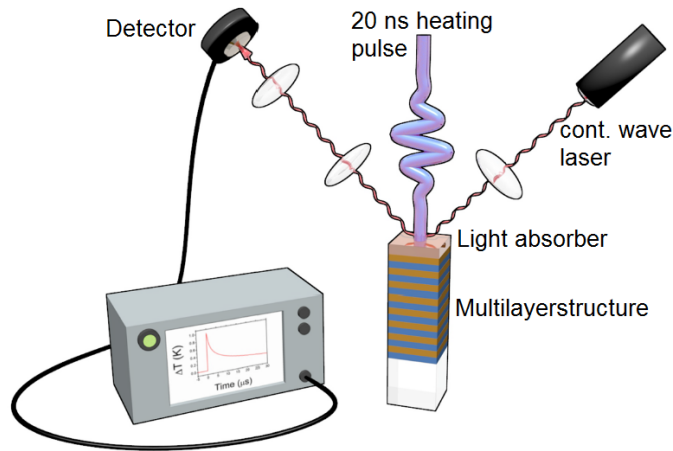


Figure 1.15: Set-up of the TTR experiment: A multilayer structure is irradiated by an intense laser pulse with 248 nm for 20 ns while reflectivity is traced by continuous wave laser analysis by fast oscilloscope.^[165]

reflectance R ^[166,167] leading to a surface temperature at the position x

$$T = \frac{J(1 - R)}{c \cdot \delta} \cdot r^{-x/\delta} \quad (1.9)$$

with light penetration depth $\delta \propto \lambda$ of the laser flux J . The temperature is then changed by short but intense irradiation with the 248 nm laser and the reflectivity or the temperature change is followed respectively.^[168] For ALD-samples due to low thermorefectance coefficients C with

$$\frac{\Delta R}{R} \approx C \cdot \Delta T \quad (1.10)$$

a copper transducer with highest possible C and R had to be added by PLD as a rough 20 nm layer.

Comparing the changes of thermorefectance in materials with and without interfaces perpendicular to the one-dimensional heat flow enables conclusions for phonon propagation and boundary scattering which will be discussed in chapter 2.3.

Hydrogen Scattering on Nanoscale Thin Oxides

Rydberg atom tagging (RAT) is a powerful novel tool in the CRC 1073 to investigate the energy transfer from an accelerated hydrogen atom to the surface of different materials. The scattering experiment was done at the novel RAT-machine by Y. DORENKAMP, generating H-Atoms^[169] from homogeneous laser-light induced splitting of HCl. These collide with the assay (Al_2O_3 -sample) and energy loss is detected as well as the scattering angle. From previous findings, there is a major difference in scattering of orientated^[170] two-atomic molecules from metals^[171] which result in high vibrational energy loss to the junction.^[172] In contrast to this, insulator scattering leads to almost no excitational change.^[173] It was therefore postulated that also atomic scattering may show this effect with ALD samples, as described previously for gold and xenon^[174] as shown in figure 1.17. Since 1979 it is agreed that adsorption of e.g. hydrogen atoms is influenced by electronic^[175] and phononic excitation of the surface material.^[176] With the presented approach, covalently bound materials in thickness of several monolayers of an insulator on a metal were investigated for the first time. This very thin layer cannot be populated with phonons and insulator's absence of free electrons made energy transfer unlikely. With this, we aim for further understanding in adsorption mechanisms, as well as fundamental insights in energy transport of excited atoms to junctions of different materials. With the previously intensively investigated single crystalline platinum in the group of WODTKE and BÜNERMANN, we also chose this metal as the underlying material in the ALD approach for good comparison. Since we know from sandwichlayer generation the strong adhesion of Al_2O_3 and its perfect ALD-behaviour (compare chapter 2.2.1 e.g. figure 2.10 or 2.9) in early experiments, we chose this oxide for investigations. Additionally to this, Al_2O_3 is also commercially available as crystalline sapphire for comparison experiments of the bulk scattering. With further investigations of energy dependent scattering from various surfaces, we aim for a deeper understanding of adsorption mechanisms playing an important role in e.g. heterogeneous catalysis.^[177] The correlation between work function of the surface, vibrational or kinetic

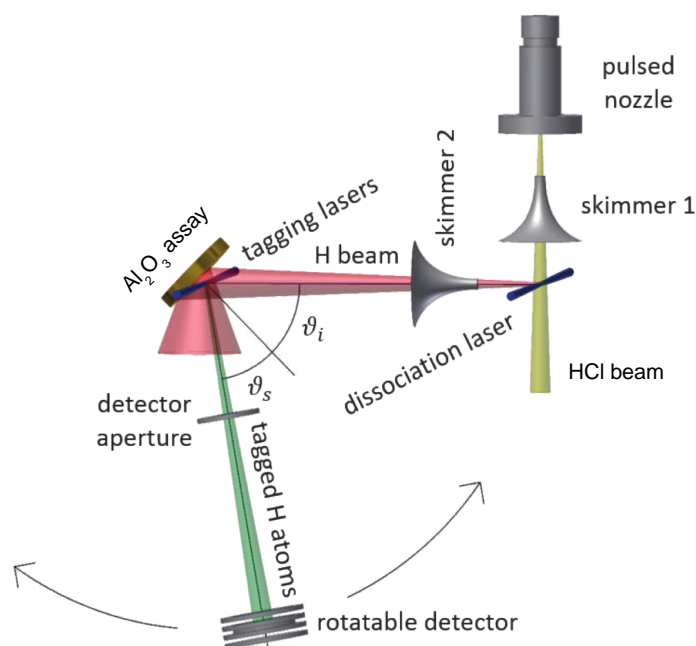


Figure 1.16: Schematic image of the RAT-experiment: A molecular beam of HCl is split by a laser (blue) and hydrogen atoms (red) are accelerated towards the ALD sample and scattered. A small fraction dependent on the detector position is measured (green). Taken from BÜNERMANN *et. al.*, 2015, Fig 2^[174] with small changes.

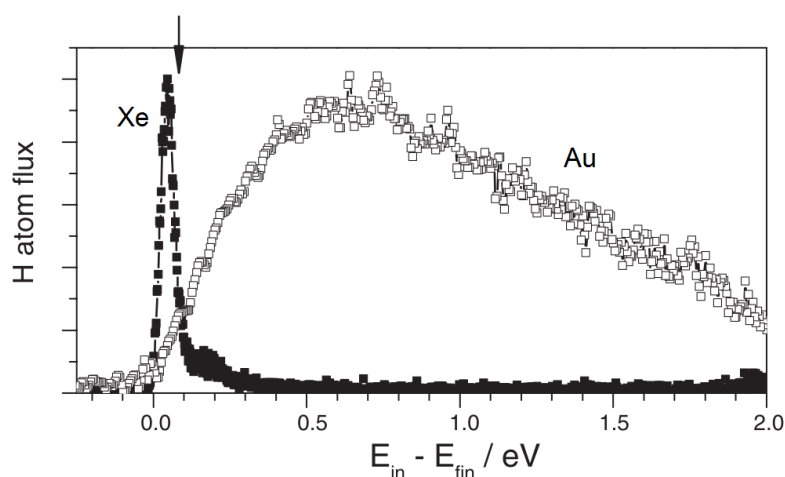


Figure 1.17: Energy loss spectrum of scattered Hydrogen atoms from a Gold (open squares) and Xenon (filled squares) surface showing kinetic energy and conductor or insulator behaviour, derived from TOF by Jacobian transformation. The experimental conditions are $E_{in} = 2.76$ eV, $\nu_i = 45^\circ$, $\nu_s = 45^\circ$ and $\phi_i = 0^\circ$, with respect to the $[10\bar{1}]$ -direction. Taken from BÜNERMANN *et. al.*, 2015, with minor amendments.^[174]

energies of the substance converted and structural properties such as roughness, film thickness, and density may once lead to a model predicting perfect combination of heterogeneous catalysts materials.

1.3.2 Tantalum Sulfide ALD for CV-Electrode Coating

Transition metal dichalcogenides (TMDs)^[179] attracted considerable attention over the past few years because of their unique properties as two dimensional materials.^[180,181] However, the synthesis of thin films using exfoliation^[182,183] as a top-down procedure lacks the existence of a well connected substrate, making property investigations challenging. Other approaches, e.g. chemical decomposition^[184] or CVD^[185] often produces several non-uniform multilayer, requiring post annealing. In contrast to the predominant amount of accessible oxygen containing materials, less than twenty binary sulphides generated by ALD were published by the time this thesis was written.^[30] However, especially MoS₂ was studied intensively and a recently presented ALD procedure including surface activation with a R-SH seed layer and annealing was able to produce very thin films of acceptable quality.^[186] Applications, such as anode coating for lithium-ion batteries^[187] or improving TiO₂-catalysts in e.g. hydrogen evolution reaction (HER) shown recently^[188,189,190] prove the value of transition metal dichalcogenides (TMDs).^[191] Furthermore, low temperature phenomena such as superconductivity and charge density wave effects have also been observed in TaS₂.^[192] TMDs are investigated in the CRC 1073 to study energy conversion after excitation in respect of the Mott- or charge density wave (CDW)-gap in the TaS₂-band structure with time-resolved photoemission electron microscopy (PEEM) leading to the ratio of electron to phonon transport in correlated materials (B07, MATHIAS).^[193,194,195] Both, the discussed chemical and the physical properties of TMDs, motivated us to study the still elusive deposition strategy of thin film TaS₂-ALD. This work will show first steps of precursor testing and TaO_x and TaS_x test deposition, which will be continued by J. GERKENS generating TaS₂ film based electrodes for electro-catalysis following the

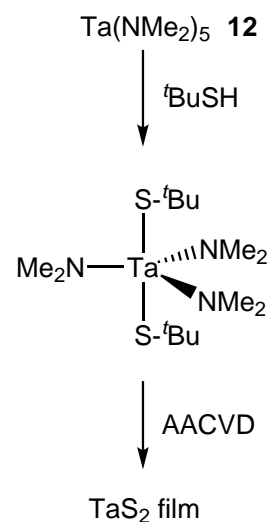


Figure 1.18: Tantalum AACVD shown by PETERS *et al.*^[178]

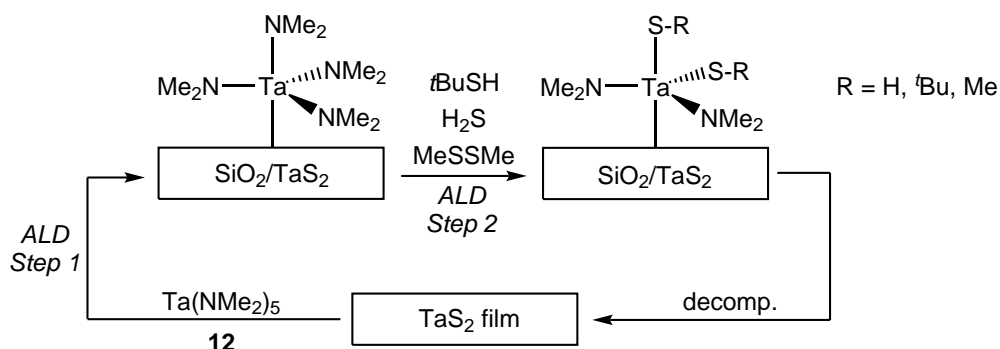


Figure 1.19: Proposed ALD-cycle forming TaS₂ thin films. In the second step the utilized sulfur sources in different experiments are displayed.

presented findings.

CVD-method originated, displayed in figure 1.18, we chose amide precursors and various sulfides to form TaS₂ and also water and oxygen as a coprecursor to deposit TaO₂ respectively. Due to the separated use of Ta- and S-source we aimed for the reproduction of the homogeneous reaction presented by PETERS *et al.* on the substrates surface, followed by the already known decomposition at higher temperatures, as presented in figure 1.19.^[178] Self limitation is achieved by the more stable Ta(NMe₂)_x surface, forming after the substrate reacts with Ta(NMe₂)₅, **12**. This was shown earlier, e.g. by the work of TOLBERT *et al.*, depositing Ta₂O₅ and Ta₃N₅ with the use of water and ammonia.^[196] The reaction with mercaptane and other sulfur sources is known in solution and the product is shown in figure 1.18 as well as the final thermal decomposition at around 300 °C^[178], reactivating the surface, changing SiO₂ to a TaS₂ surface.

1.4 Motivation and Scope of This Work

Several examples for transition metal (TM) ALD procedures were described in the previous sections. However, defined systems and deposition parameters for some materials still remain uncharted. Beyond that, elusive substances often feature interesting qualities which have been betokened in the earlier chapters of this work. Aim of this thesis is the extend of available ALD methods by the application of a novelistically designed ALD reactor.

In more detail, this work can be structured in four parts, namely the development of the reactor followed by several testing procedures which define the constraints of the machine. Here, Al_2O_3 , Pt and Ir were chosen as literature procedures. As a second section, these materials were combined to high interface density materials and analysed in the scope of the CRC 1073 with respect to energy exchange. To turn over a new leaf by veering away from literature, in the third and fourth part, novel ALD procedures were investigated. These are thin films of Co for transistor size miniaturisation in cooperation with BASF and secondly we aimed for TaS_x deposition which can be utilized on the one hand in charge density wave investigation within the CRC 1073 but also act as an interesting candidate for electrode coating in heterogeneous catalysis on the other. Since the motivation for every entity is different, they will be discussed separately in the following sections.

Part 1: Construction and Testing Procedures

To apply Occam's razor, there are two different kinds of deposition chambers. One handles highly textured structures with long resting times of precursors and separated pump and purge times. Albeit the benefits of this settling chamber are interesting, it did not match the planned applications. For the presented experiments, the second type will be constructed which unites a constant, laminar flow and exhaust development with the potential to deploy up to six different precursor inlets. This will be constructed as a compilation of all beneficial properties, presented in recent

literature. The chamber can be run as a “hot-” or “cold-wall” chamber with a temperature window ranging from 20 to 450 °C. It is constructed for process pressures from 0.1 mbar to 100 mbar with the corresponding flow rates of 1-500 mL · min⁻¹. Testing the set up and setting a network for thin film analysis methods in the group of S. SCHNEIDER, we will apply several well understood ALD procedures. However, these materials should not only act for chamber examination but also should be usable building nanolaminates (see part 2). Because of their huge difference in the Young modulus, their Debye temperature, crystallinity, phononic density of states (DOS) and deposition parameter, we will choose Al₂O₃, platinum and iridium as first targets.

Part 2: High Interface Density Nanolaminates

Still, fundamental understanding of energy transport in condensed matter is debated. Models describing the effect of structural probabilities still only touch threshold regions only applicable for some simple materials with sufficient compliance. Therefore, energy dissipation delivered by photons and molecules will be investigated using ALD-prepared multilayer structures together with TTR and atomically thin isolators on metallic ALD-substrates with RAT. With optimized procedures of aluminium oxide and platinum in hand, a strategy will be examined generating usable materials.

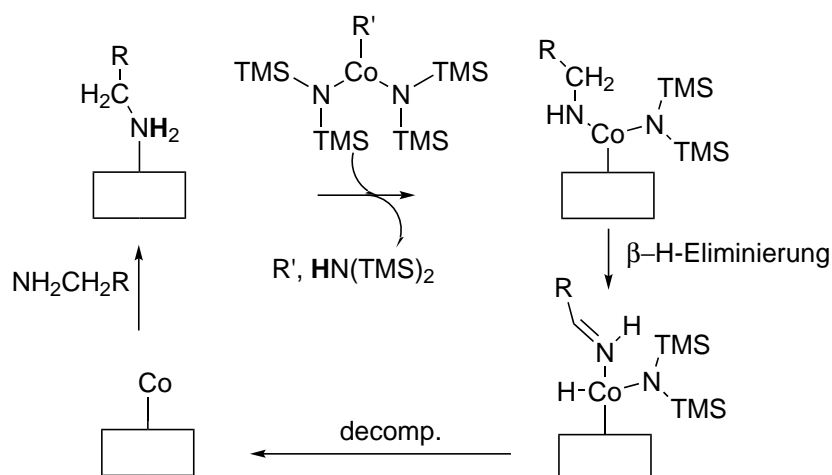
Part 3: A Synthetic Route for Thin Cobalt Films

Elusive ALD strategies for conductive elements in microelectronic industry limits the trend of downscaleable components following Moore’s law. Other deposition techniques applied result in layer thicknesses far above the 1 nm scale, which is often published for ALD materials. In this thesis, we will try to find a way to shrink the thickness of a cobalt diffusion interlayer in transistors which hold a diameter of about 15 nm the time this thesis was written. For this purpose, a variety of precur-

sors will be synthesized and tested in the reactor with respect to their evaporation, stability and deposition properties. Generally we will focus the project on cobalt amides, stabilized by a labile phosphine ligand. These complexes feature the absence of close to metal hydrogen atoms. We aim for the reconversion of the stable Co-amide self-limiting structure on the surface during the application of an amide forming highly unstable Co hydrides after ligand exchange reaction. This is depicted in scheme 1.4.1.

Part 4: A Novel Strategy Accessing Tantalum Sulphide Films

Due to their unique electronic (band gaps, heterogeneous catalyst) and structural (2D material, CDW) properties transition metal dichalcogenides are studied intensively. Furthermore, considering the quantity of binary metal materials, sulphides lie far behind oxides and nitrides in this respect. Initially, we will direct our focus on published CVD and ALD precursors, e.g. utilized in TaO_x or TaN_x depositions. There we will start with simple systems like TaCl₅ and Ta(NMe₂)₅ with various sulphur sources, ranging from H₂S to thiols and disulfides.



Scheme 1.4.1: The general idea of Cobalt deposition based on the decomposition reaction of close to metal hydrogen atoms, using protected Cobalt-amides and primary amines.

2 Results and Discussion

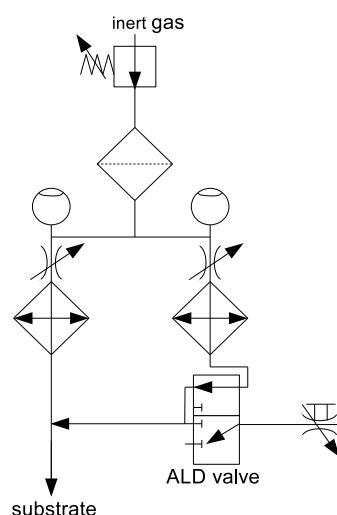
2.1 A Novel Reactor Design for Thin Film Deposition

2.1.1 Design and Construction

To establish a thin film generation technique in the group of S. SCHNEIDER, using untextured substrates, a viscous flow ALD reactor was designed. Following literature terms, described in chapter 1.2 this can be classified as a “hot and cold wall, cross laminar flow multiple substrate reactor”.

For the purpose of stacking different layers, as presented in chapter 2.3, up to six different precursors can be sequentially pulsed within milliseconds. They are mixed in the laminar flow tube with

the separately heated inert gas. The oxygen-free (Agilent oxygen trap, 20 cm, figure 2.1.1) Ar stream is then split, thus about 10-20% is directed through the ALD valves to provide fast transport to the laminar flow tube avoiding contamination and long diffusion times as depicted in scheme 2.1.1 and figure 2.1. The exact distance of 12 cm to the first wafer position was chosen because calculations predict the gas



Scheme 2.1.1: Schematic drawing of the flow conditions in the presented chamber (ISO 1219:2012).

mixture to form a laminar flow (figure 2.2) after this pathway length after recombination. The inlet ports 2-6 were attached in minimal additional distance. Bending of the inert gas tubes and valve construction geometry demand for 6 additional cm per valve inlet. As displayed in figure 2.1 (O_2/O_3) gaseous or highly volatile precursors are attached to port 5 and 6 because a higher amount of precursor gas required a longer way to become laminar.

Applying theory described in section 1.2, the corresponding R_e for both tubes ($d_{\text{mix-tube}} = 10 \text{ mm}$, $d_{\text{tube}} = 6 \text{ mm}$) can be calculated to be $R_e = 48 / 139$ for Ar and $R_e = 21 / 106$ for N_2 , respectively, using dynamic viscosity of $17.1 \text{ (N}_2\text{)}$ and $22.1 \text{ } \mu\text{Pa} \cdot \text{s}$ (Ar),^[197] as described in the following calculation (pressure assumed to be 4 mbar).

$$R_e^{\text{Ar}}_{\text{mix-tube}} = \frac{Q \cdot D_H}{\frac{\nu_{\text{dyn}}}{\rho} \cdot 2\pi r_{\text{tube}}^2} = \frac{10^{-4} \frac{\text{m}^3}{\text{s}} \cdot 1.32 \frac{\text{m}}{\text{s}}}{\frac{22.1 \cdot 10^{-6} \frac{\text{kg}}{\text{m} \cdot \text{s}^2}}{5 \cdot 10^{-3} \frac{\text{kg}}{\text{m}^3}} \cdot 2\pi (0.01 \text{ m})^2} \approx 50 \quad (2.1)$$

Flow conditions are best described as predominantly laminar since values for all reactor parts calculate to be smaller than the critical $R_e = 2300$. (value at which the laminar flow could turn turbulent). Nevertheless, $R_e > 1$ are always effected by turbulence, which has to be taken into account for the evaluation of diffusion and purge phases. Decreasing R_e are furthermore achieved by consistent use of electropolished steel (smallest roughness, low surface mobility) and dislodged weldseams with high stability against rapid temperature change and heat.

The reactor has 24 independent heating zones, controlled by a self-written program using independent and experimentally found PID parameter for every zone (for a detailed explanation review chapter 2.1.2 and equation 2.2). Due to the formation of corrosive gases in the ALD process the chamber is pumped by a chemical resistant scroll pump (Edwards, nXDS) resulting in a 2-10 mbar total pressure and about $1 \text{ m} \cdot \text{s}^{-1}$ flow velocity at the substrate position. The pump speed can be controlled by either reducing the pump rpm speed to 60 %, or cutting off the bellows-type valve, attached in between pump bypass (with manometer, MS exhaust, and scroll pump)

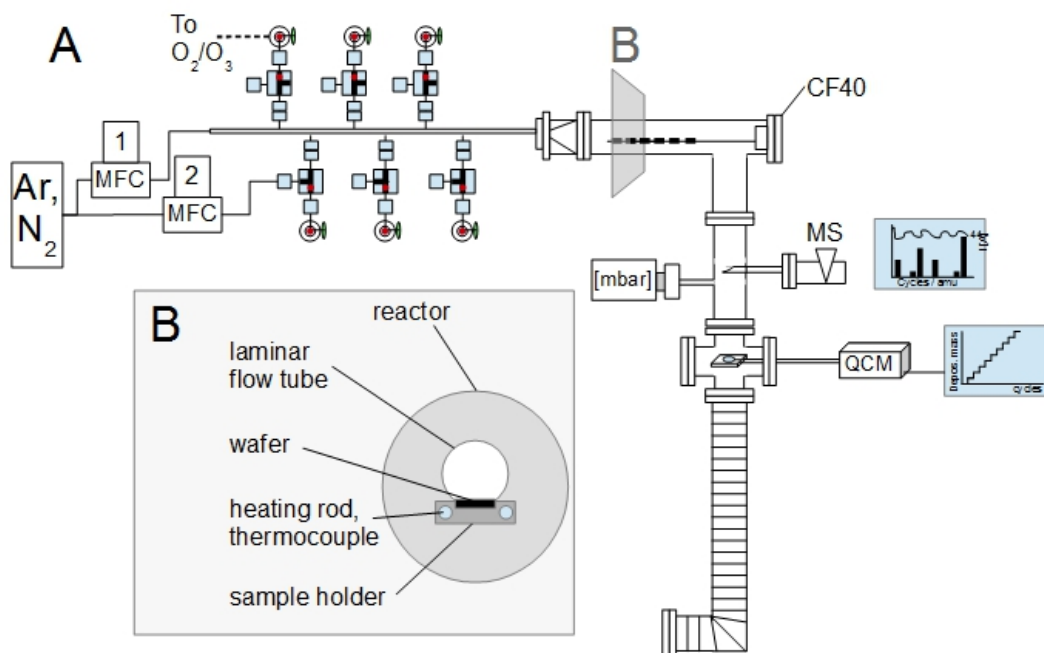


Figure 2.1: **A:** General scheme of the laminar flow reactor. Up to six precursors can be pulsed, while allowing for in situ analysis with MS and QCM. Zoom **B** (transparent intersection in **A**) provides a lateral view into the deposition chamber, imaging the wafer against the laminar flow tube position. A more detailed and true to scale drawing with all part numbers and sealing information can be reviewed in the “reactor manual”.

and chamber, resulting in a lower C_v value (fully opened, it processes $C_v = 0.24$). Flow rates are indexed by the resulting pressure at the substrate and the delay in between a pulse and its arrival in the MS. Due to diffusional delay owed to the MS-cannula, these values act as crude assumptions and may serve as limit numbers.

To ensure a maximum of precursor molecules interacting with the surface without high impact energy, the laminar gas stream is directed side-wise onto the substrate (compare figure 2.2, where the uncoloured area constitutes the sample holder). In contrast to other geometries, this may allow for multiple interaction events leading to binding and higher surface saturation as a consequence thereof. The substrate is mounted into a heated sample-holder (maximum temperature 450 °C) generating a flat surface to avoid pockets and thus long pump/purge times. Advantageously, it

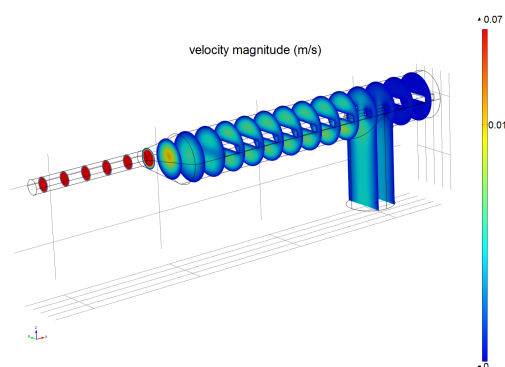


Figure 2.2: Finite element calculation of the laminar flow in the chamber and mixing tube. The split ratio of the flow above and below the sample holder amounts to 45 to 55 %.

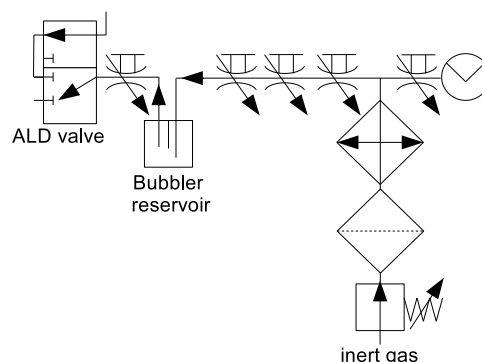


Figure 2.3: Flow diagram of the bubbler (Precision Fabricators Ltd., PF-25CCHBC-G). The connection of the ALD-valve was described previously in figure 2.1.1.

allows for top and underside deposition to give rise to the CVD/ALD ratio. As shown in figure 2.1 the laminar flow tube's bottom end is on same height as the substrate surface, parallel to the stream direction. Because the exhaust gas is pumped downwards, the gas stream's direction is expected to provide perfect interaction with the substrate this way. Calculations predict the laminar flow to split into 0.8 : 1 with the majority can be found under the sample holder. Flow velocities measured using the pulse time of the valve and the detection time in MS are significantly higher than the prediction, the calculated split ratio therefore gives a lower limit of actual split ratios found in practice. Thus, the amount of precursor above the substrate is equal or larger than the prediction due to preservation of flow trajectory.

The machine is equipped with a quadrupole mass detector (QME 220, $m/Z = 1-300$) to allow *in situ* identification of reaction- and exhaust gas components, enabling us to illuminate the surface chemistry mechanism. Comparing literature *in situ* analysis techniques (chapter 1.2), we decided for a MS because of its outstanding possibility to detect very low concentrations of reaction products, without any change of the flow parameters (since other techniques need reactor windows, etc.). In more detail, these fragments are normally drawn 15 cm below the chamber, with a needle from the center of the gas stream. Furthermore, it is possible to attach a cannula

to directly siphon on the wafer's surface. All presented mass studies were done in the normal mode, giving rise to direct response of surface reactions. With *in situ* MS studies we could ensure an oxygen content in the purge gas, e.g. during reaction, of 50-200 ppm. This is comparable to the absolute oxygen concentration in the inert gas box, used for precursor preparation and synthesis of air and moisture sensitive compounds, as implied in chapter 2.4.1. The QUADERA program was complemented by about 25 multi current detection (MCD) routines, mainly investigating decomposition products in chapter 2.4.1.

For poorly vaporizable compounds or precursors, whose decomposition temperatures are very close to the sublimation temperatures, the possibility of a bubbler (Precision Fabricators Ltd., PF-25CCHBC-G) is designated. As shown in figure 2.3, in this set-up a small constant gas stream is directed through and over the precursor in the reservoir. A bubbler does not increase the amount of material which is sublimed (rather reduce it due to increasing pressure), but highly increases the amount transported through the ALD-valve, since the flow is now directed owed to higher pressure in the bubbler and not stochastic as before. The bubbler is filled with the compound, sealed and an inert gas (again purified by a separate O₂ trap). The drawback with bubbler experiments are higher pressure in the reservoir sometimes leading to a drop of substrate from the holder. The pressure therefore has to be adjusted carefully and this is done by three valves with very low C_V values in between the precursor and the heated inert gas stream.

We are furthermore able to track deposition with a QCM (JCM, SQM-160, 120 °C / 285 °C optimized crystals, 6 MHz) as a second *in situ* technique to detect film evolution down to fractions of monolayer growth. This was shown earlier for mechanistic studies of Pt-deposition, proving cyclopentadienyl (Cp), methyl (Me), or C_xH_y to be the surface terminating species.

For cleaning purposes and oxide depositions of noble metals, we attached an ozone generator (BMT, 803N) to the chamber, producing up to 20% O₃ in O₂ to clean surfaces from carbon reminders. While using O₃, the exhaust gas is directed through

a bypass over a O_3 catalyst (BMT, reduces O_3 to 1 parts per billion (ppb)) preventing pump or manometer damage. Since O_3 decomposes within minutes, we build a reservoir which is evacuated continuously via bypass geometry. This warrants for constant concentration and reproducibility.

The purge gas heating is performed in a steel tube coiled around and through a hot brass block, using a 15 m pathway and several seconds dwell time. The block is heated with two heating rods, 230 V/125 W each with a thermocouple in the center determining average temperature. The two gas streams (mix tube and valve purge) are directed mirror inverted through the heating block and the temperature of both is expected to be equal.

The exhaust gas is cleaned, additionally to the ozone bypass, by different components. Most importantly - to avoid valve, catalyst, and pump damage - a particle filter (œrlikon, leybold vakuum, 140116T) is installed in between the heated exhaust gas tube and the bypass valve. The filter blocks particle sizes down to 100 nm. Additionally, due to a large surface and low temperatures, unreacted precursor is expected to condense at the filter block. This reminders are expected to be quenched by the second pulse, avoiding high concentration and condensation in the pump or manometer.

Acids, redox active or toxic fragments which may evolve during the ALD procedure (e.g. HCl from $TaCl_5$, H_2S , ...) are additionally trapped in gas washing bottles using solutions of bases or H_2O_2 .

2.1.2 Reactor Control: Software

To control six valves within milliseconds and up to 25 independent heating zones while avoiding hotspots due to overheating, a program was written with Laboratory Virtual Instrument Engineering Workbench (LabVIEW)^[198,199] using National Instruments hardware and software. This includes a source code called “block diagram” and a graphical user interface (GUI) called the “front panel”. A simplified flow diagram in scheme 2.4 and 2.5 shows its general features. Note that a detailed description of all program parts, sub-programs and hardware compounds and corresponding wiring are available in the “Reactor Manual” as an appendix.

Code

The code is written with Laboratory Virtual Instrument Engineering Workbench (LabVIEW), a system design platform and development environment for a visual programming language from National Instruments. The graphical language from National Instruments, called “G”, well suited for data acquisition, instrument control and industrial automation and is e.g. used in the code of Windows and different Linux distributions.^[198,199]

All parts of the code are labelled with numbers (1, 2, 3a-f, 4a-i, 5) and color coded in the block diagram. Every sub program is explicitly explained in the “Reactor Manual”. The program consists of two parts executed consecutively. In the first part, the user is able to set parameters and prepare the chamber for the following deposition and pulse sequence. After starting the deposition changes in pulse parameters are not possible, while temperature settings can be changed throughout every program stage.

The general features of the main program during deposition are two independent loops, controlling valve opening and heating as shown in figure 2.4. A heating cycle is executed in about 200 ms and consists of a measurement step, using a NI 9213 module to digitalize the voltage of the type-K thermocouples to calculate the temper-

ature, followed by a comparison step of the temperature using a PID sub-program as a control loop feedback mechanism. With individual parameters for P (proportional, K_P), I (integral, K_I) and D (derivative, K_D) experimentally found for each heating zone, this program outputs a percentage $H(t)$ reflecting the need for heating to the set point (T_{SP}). Whenever this value increases to 50 % heating is applied for the next 200 ms. In the following equation, the basic function of the controller is shown, with $T(t)$ being the actual temperature, and $t_1 - t_2$ the approximated heating delay time.

$$H(t) = K_P(T(t) - T_{SP}) + K_I \left(\int_{t_1}^{t_2} T(t) dt \right) + K_D \left(\frac{dT(t)}{dt} \right) \quad (2.2)$$

A unique heating condition is expressed as a sequence of binary digits, where each position in the sequence corresponds to a valve or heating part. This number is generated by a sum of 10^n where n is an increasing natural number, reflecting the corresponding heating zone, depicted in scheme 2.4. The digit at a given position in the sequence denotes heating (1) or no heating (0). After interpretation of this sequence as a binary number and conversion to a hexadecimal base, the number is communicated to the NINI9403, switching current on or off for the next iteration of temperature comparison (in 200 ms). NI9375 is addressing pilot valves to open the ALD valves by applying pressure with switching, in a similar manner.

During deposition, the pressure is measured five times per second and plotted to the graphical user interface as direct data and an average of ten data points. This information is also copied to the deposition report, consisting of all temperatures and pulse parameters followed by the pressure as a function of time given as a x/y data table, which is printed after termination of the deposition process.

A surveillance program monitors inner pressure and shuts down the machine if a pressure limit of 70 millibar (mbar) is exceeded. To avoid heating damage to any part of the machine, every heating zone is assigned a threshold temperature, above which every set-point is instantly set to zero and warning is displayed to the user. This temperature check is performed with a frequency of 5 Hz as a part of the

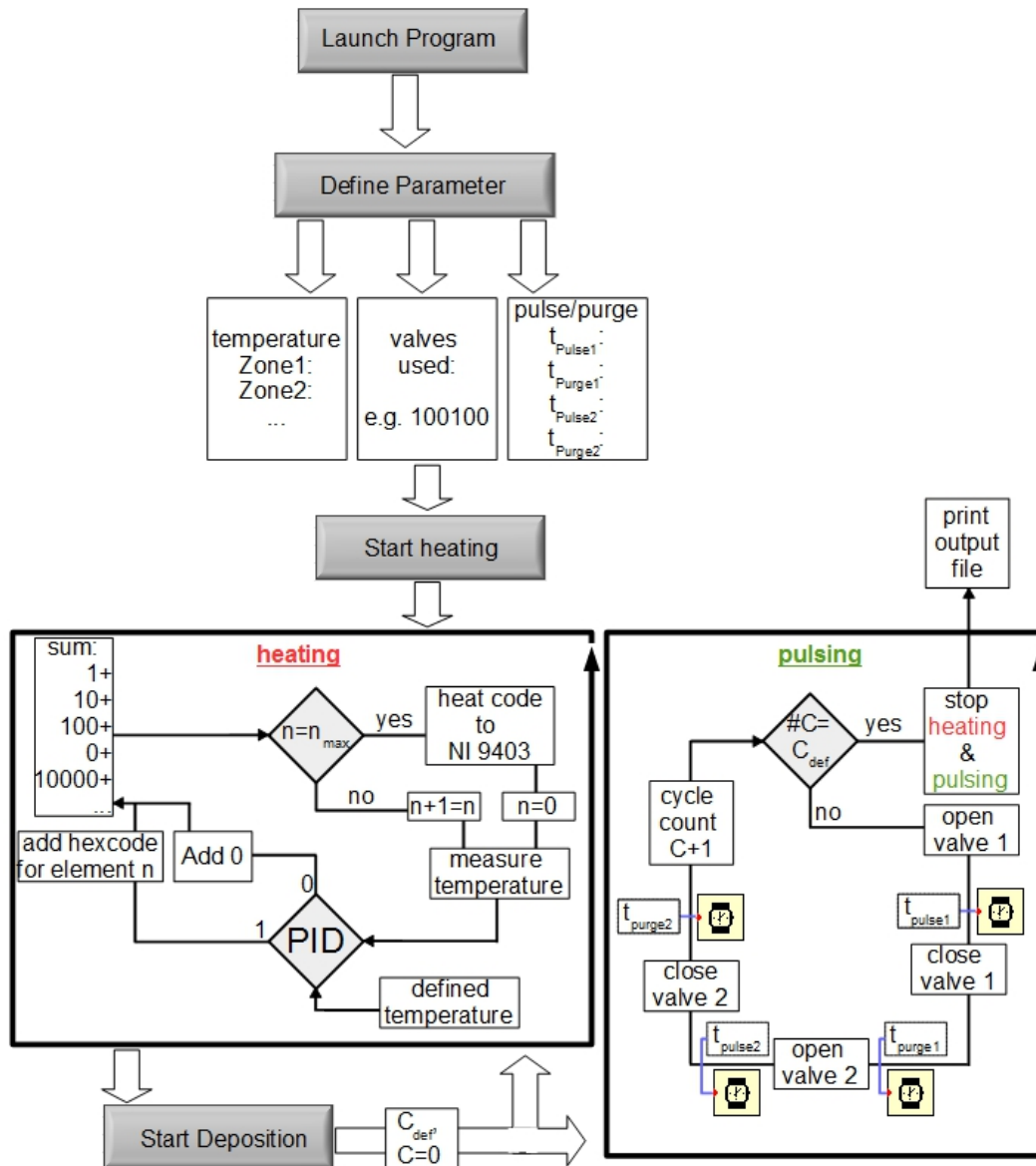
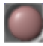



Figure 2.4: Simplified flow diagram of the execution sequence during deposition. Starting in the very top of the image, defining parameters for the projected deposition. The main program starts with the loop on the left side, executed in 200 ms. Here, the temperature is measured and compared with the parameters defined in the very beginning for every heating zone n , using a PID with experimentally optimized constants for I and D. When $n = N_{\max}$ occurs, a number is given to NI 9403. This number can be understood as a binary integer sequence of n_{\max} characters, defining heating on (1) or off (0). In the real program, this is translated to a less demonstrative hexadecimal code which is not displayed here. Reaching the final temperature, pulsing can be switched on with the definition of the amount of cycles C_{def} . This sequence is displayed in the right loop, where yellow boxes stand for waiting times. Note, that at this position, the amount of C , $\#C$ equals C_{def} both loops are stopped and an output file is written.

heating loop.

Graphical User Interface

Figure 2.5 illustrates the entry procedure in a simplified manner. Although a variety of prompts will turn up by clicking the displayed buttons, the general five-step-procedure can easily be learned by everyone without any programming skills. Boolean controls, showing turning green if the input was correct provide a sense of security during the execution. In more detail, the graphical user interface (GUI) displays deposition parameters and progress on three pages of a notebook, selectable by choosing one of the three riders on the left side of the starting page. The first tab appears by launching the program, and is displayed in figure 2.6 as a screen shot. It re-

veals a simplified picture of the reactor design and is made to guide the user through the parameter entry. In the bottom left box, one is able to launch a prompt to type all deposition parameters such as temperatures for all heating zones (“valve, reactor temperature”) and designation string, pulse and purge parameters for the precursor (“define precursor”). Before the deposition process is started, the user is directed to a review page displaying all parameters and values to ensure no mistakes were made (“check all values”). Due to the possibility of ultrafast pulsing, the input has to be made in millisecond units and degrees Celsius because of a temperature variance of 3-5 K, respectively. After defining the precursor in a prompt, these informations are displayed in the top left table and directly at the valve number in the simplified scheme in the screen’s center. Additionally, LED-symbols depict the state of both heating zones (red LED, lit for active heating:  → ) and valves (green

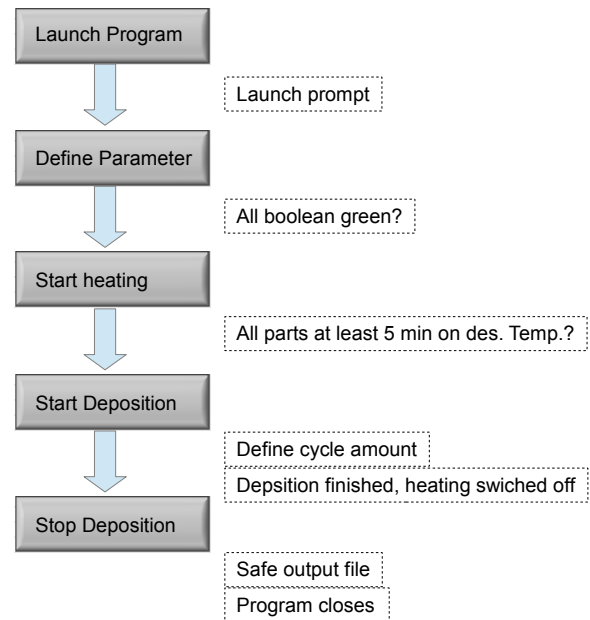




Figure 2.5: Schematic flow diagram of a general control sequence for a deposition showing buttons to press on the left and type or control events on the right side.

LED, lit for opened valve:  \rightarrow ). Finally the user is able to run the pulse-purge sequence, defined previously, selecting the amount of cycles to run as a last parameter (“Start Deposition”) in the top right. This is blocked by a control unit (“Temp _ reach?”) comparing the set and actual temperature to secure no precursor is pulsed in a cold or too hot chamber. Deposition progress is indicated by displaying the cycle number and an estimated time of completion.

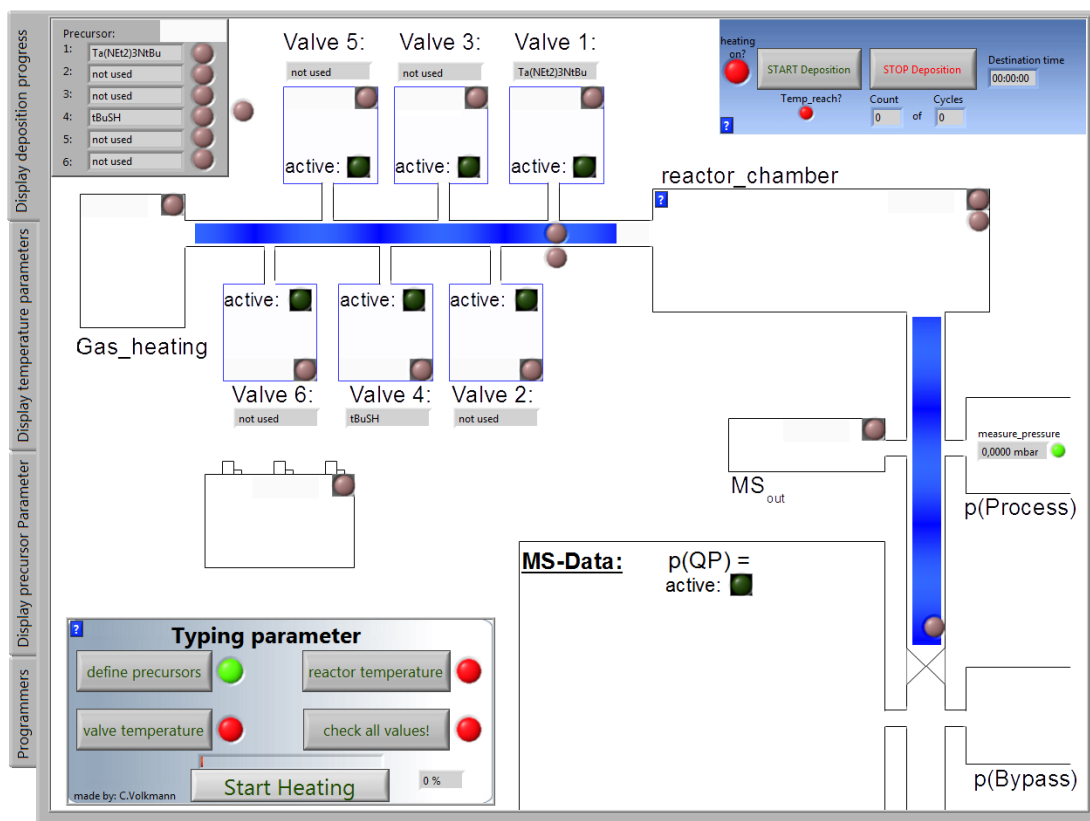


Figure 2.6: Screenshot of the first GUI page (“Display Deposition Process”). In the lower left the user is able to set pulse parameters and temperatures. In the upper left corner the currently used precursors can be read. The center of the screen shows a reactor scheme with red control lamp showing the heating zone is currently addressed and green control lamps showing the valve to be open or closed.

To control heating zones and pressure, the second index tab (“Display Temperature Parameter”) is used. There, after starting the heating on the first tab, the given temperatures are displayed in the upper part and can be compared with the

displayed, measured temperatures within milliseconds. Temperatures of all heating zones are plotted with unique colours in the lower left corner graph. Figure 2.7 shows the initial heating of reactor parts as a linear increase in temperature. The subsequent control phase is visible as a plateau of nearly constant temperature. An appropriate choice of parameters yields a smooth transition between linear heating and control without ringing.

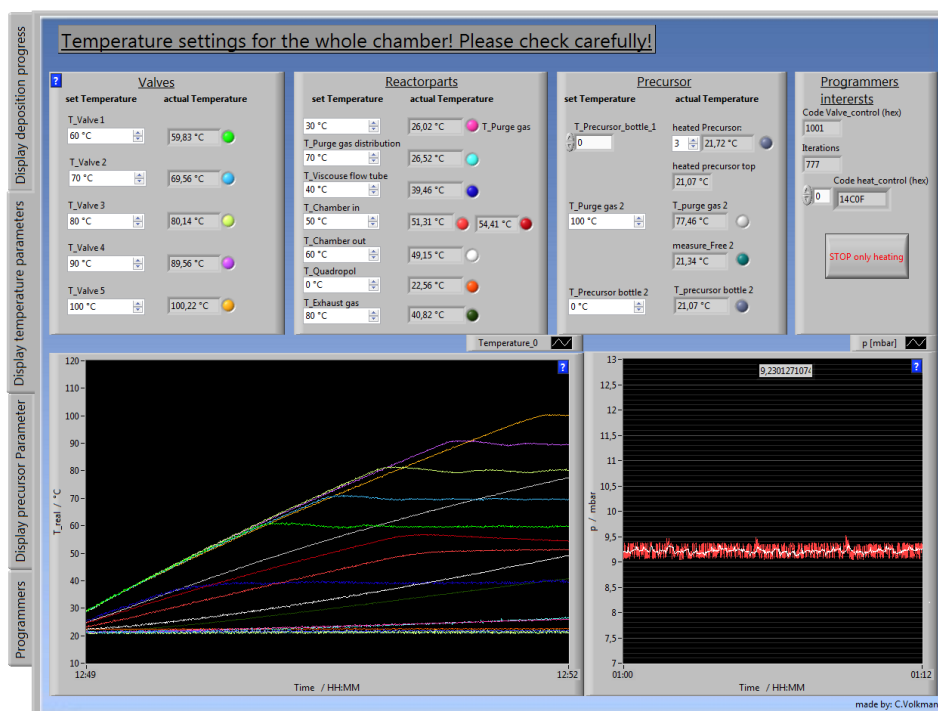


Figure 2.7: Screenshot of the second page (“Display temperature parameter”) comparing set and actual temperature parameter in the top and showing their development in the bottom left graph. On the right side the pressure in the chamber is displayed (Imported from a TaS deposition, using $Ta(NEt_2)_3NtBu$ and TMS_2S).

Due to different mass, heat capacities and surface of heated elements the slope for their heating differs. While the valves reach their temperature within minutes, the block for gas heating requires up to an hour because of purge gas cooling. A third box in the upper part displays precursor bottle heating (“Precursor”). Two precursor-containers can be heated in a single experiment. These temperatures can be changed during a deposition, e.g. to measure concentration using an unknown

precursor or if a precursor-bottle runs empty. As an example for ideal concentration the pressure for a TaS_x-deposition using Ta(NEt₂)₃N^tBu and TMS₂S in high flow rate is inserted in the bottom right. If the pulse increases the pressure by a minimal, still being visible amount confirms the bottle still being filled while using appropriate amount of material (note, that pulsing would be forbidden at this stage due to the still pending heating procedure). The code for valve switching (here 100010, so addressing first and fifth port) and heating (here 14C0F = 000010100110000001111, so heating zone 1-4, 10-11, 14 and 16 are live) is displayed in the upper right corner (for details, see scheme 2.4).

The third page (figure in the appendix ??) shows the values for the final printout of the deposition. Finally several help buttons can be found in the GUI (?). These give general and detailed help explaining common mistakes and provide hints.

2.2 Chamber Testing and Improvement of Depositions

2.2.1 Aluminum Oxide

To test our system, a simple material / element was chosen for which the deposition is well established and described in literature. The oxide composite should be feasible to use, not only as a testing material for the chamber but also as an interlayer in phonon blocking structures and super thin isolator materials for scattering purposes. We focused on Al_2O_3 , due to its convenient properties: low roughness, amorphism, comparable to single crystal stoichiometry, density, vapour pressure of the precursors and their commercial availability. Although the precursor handling turned out to be challenging, the reactivity of trimethylaluminium precursor with oxygen and water in the chamber was best to evaluate the leakage influence on deposition observations. Furthermore, recent literature shows the possibility of Al_2O_3 deposition on noble metals such as Ir^[200] or Pt^[201,202] with good adhesion.

Following literature procedures TMA and water were chosen as unheated precursors to react on a warm (75-100 °C) SiO_2 substrate (for details see 5.3.1). As a first experiment we investigated the suitability of the reactor for ALD (2.1.1) with respect to the CVD to ALD ratio, which can be extracted from the data presented in figure 2.9. Film thickness as a function of pulse length, approximately proportional to the precursor amount of each cycle, is displayed. In this experiment we varied the pulse duration of TMA in several increasing steps from 5 ms, which is the min-

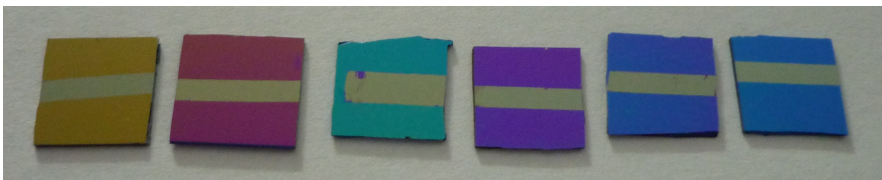


Figure 2.8: Correlation of wafer color after successful deposition indicative for film thickness. Film dimensions ranging from 20 to 140 nm corresponding to 50-600 cycles.

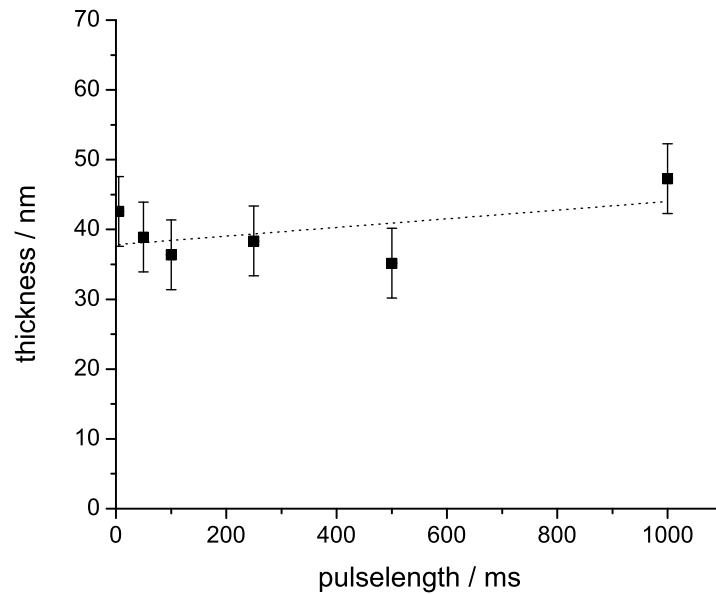


Figure 2.9: Correlation of pulse length TMA and film thickness of Al_2O_3 measured with profilometry giving rise to ALD/CVD ratio in the novel set-up proportional to the slope of linear regression. Error bars correspond to the standard deviation of numerous measured data points and time error to manufacturer's data of the ALD valves.

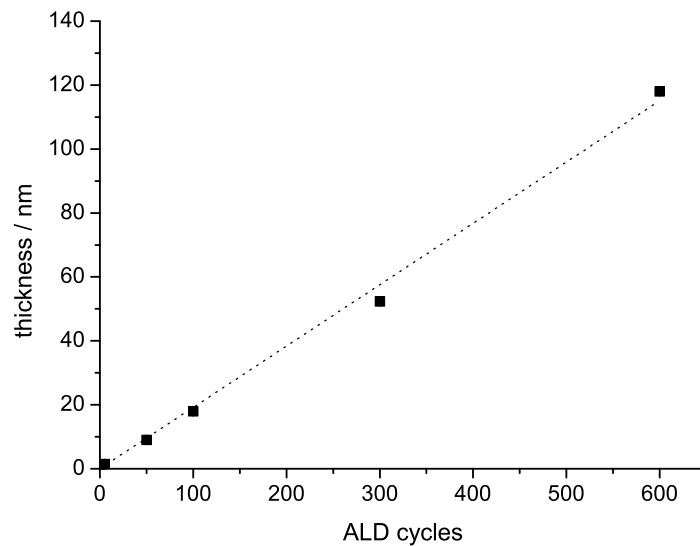


Figure 2.10: Correlation of film thickness as a function of ALD cycles with linear regression. Data points measured with TEM, error bars correspond to measuring and interpretation (the error is similar to the size of data points).

imum opening time for the ALD-valve, to 1000 ms. This corresponded to a barely measurable pressure increase in the chamber to a 6 mbar peak maximum above the constant 2.5 mbar inert gas stream, using 1000 ms instead. The entity of cycles (sequentially water and TMA) was kept constant to 200. Substrates were previously prepared with Capton tape perpendicular to the gas flow direction as shown in figure 2.8.

Film thickness was measured with DEKTAK profilometry in both directions in line with the gas stream direction, perpendicular to the taped area displayed in figure 2.8 three times each. The average values of these 4-6 data points were plotted with error bars, which corresponds to the standard deviation. Within error bars, there was no significant correlation of film thickness and TMA concentration, even with a raise of the quantity of material by orders of magnitude. In addition to that, no significant difference in both stream directions could be observed since the deviation from mean value was not associated with the measuring position. Both these findings guarantee for a minimal CVD stake in the novelistically designed chamber.

Additionally, the average value of the data in figure 2.9, perfectly fulfilled the estimated thickness given by the linear regression in figure 2.10. This plot shows the correlation of film thickness to the amount of deposition cycles, applied in the experiment, proving reproducibility and initial phase behaviour. As they are the most accurate, HR-transmission electron microscopy (TEM) images were evaluated and fitted here, but also profilometry, ellipsometry data (shown in figure 2.12 as an average of three region of interest (ROI), investigating film thicknesses in different areas marked as green oblongs and fitted with model data of the corresponding software) and SEM values were in perfect agreement with the applied linear regression.

Figure 2.10 proved reproducibility and the possibility of very thin film deposition: the bottom left shows a correlation of 1.5 nm film thickness to five deposition cycles. From this plot a gpc-rate of $1.94 [\pm 0.06] \text{ \AA} \cdot \text{cycle}^{-1}$ could be calculated which was found to be slightly higher than most of the reported Al_2O_3 thermal deposition procedures^[36], although deposition rates in the literature differ between $0.8 \text{ \AA} \cdot \text{cycle}^{-1}$ ^[203]

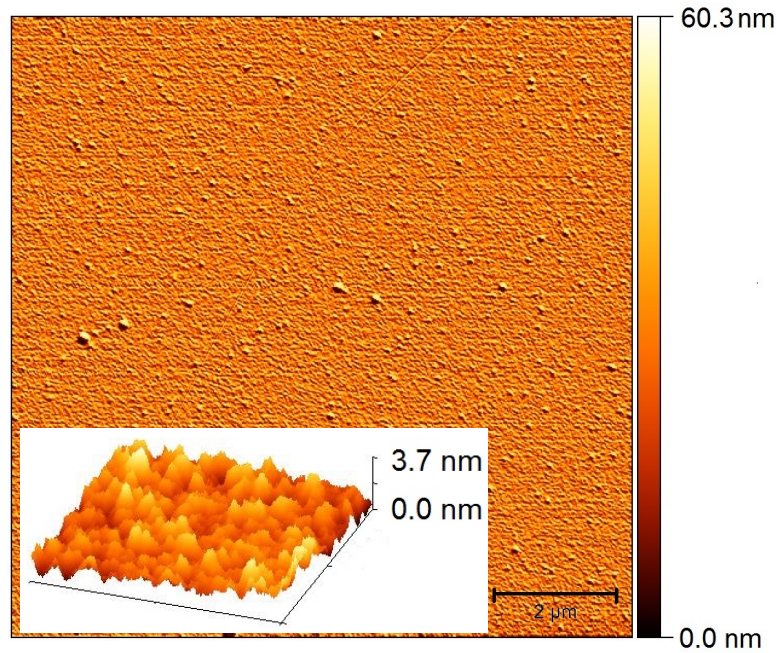


Figure 2.11: Atomic force microscopy analysis of a 50 nm Al_2O_3 film showing a height profile and large and small scale maximum roughness. The retral image show a top view on a $10 \cdot 10 \mu\text{m}^2$ sector showing a few dust particles in the size of 50 nm. The overlaid image shows the roughnes of the uncontaminated deposited material in a 3-D view of a $0.5 \cdot 0.5 \mu\text{m}^2$ area.

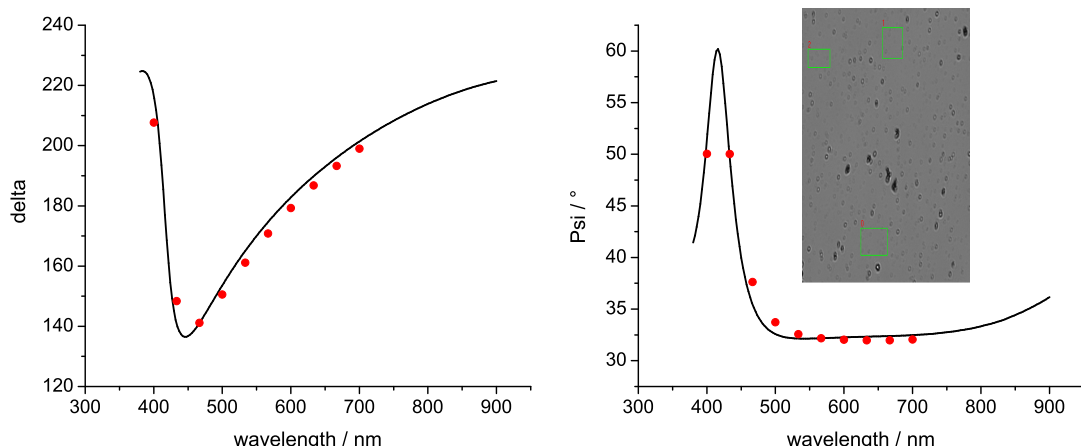


Figure 2.12: Ellipsometry Δ and Ψ plots, comparing measured data (red dots) and fit (black line) for $30.5 \pm 0.3 \text{ nm}$ of Al_2O_3 (150 Cycles) on 200 nm SiO_2 (calculated thickness refer to all ROIs, shown in microscope image). Not shown: reference data for the empty wafer show $d(\text{SiO}_2) = 204 \pm 2 \text{ nm}$.

and $2.4 \text{ \AA} \cdot \text{cycle}^{-1}$ ^[204] showing a strong correlation on the reactor design. Additionally, the separation of hexagonally close-packed planes of oxygen in sapphire is 2.17 \AA ,^[36] setting a limit for the maximum deposition rate (no CVD contribution) surmounting found gpc.

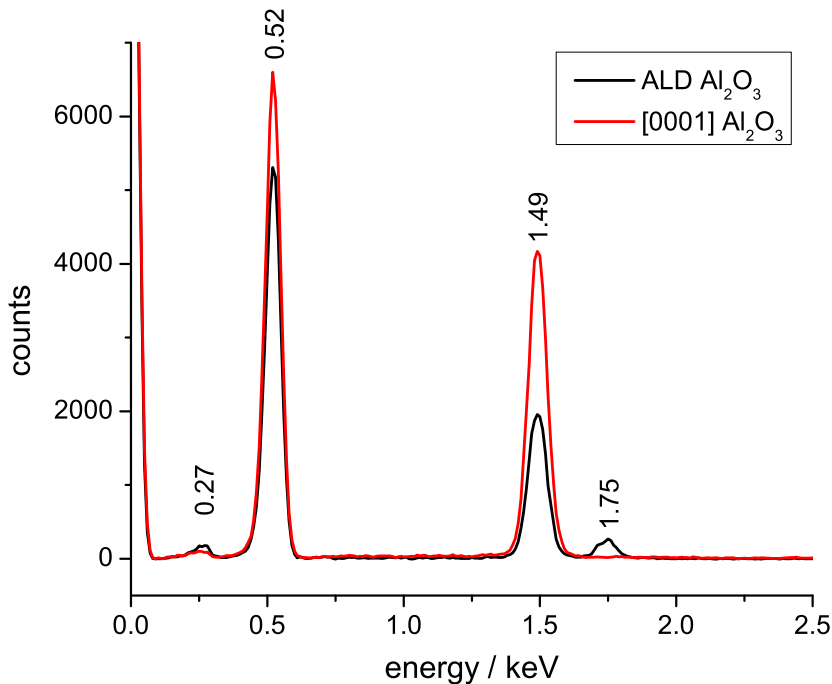


Figure 2.13: EDX spectrum of a single crystalline (red) and a 50 nm ALD assay. Displayed energies correspond to (left to right) $K_{\alpha}(\text{C})[0.27]$, $K_{\alpha}(\text{O})[0.52]$, $K_{\alpha}(\text{Al})[1.49]$, $K_{\alpha}(\text{Si})[1.75]$. Note, that the underlying SiO_2 substrate is also effecting the O-signal in the black graph.^[205]

Furthermore, films were found to exhibit suitable properties, such as very low carbon content and minimal roughness, perfect for forming multilayer materials. Impurities were measured using EDX, electron energy loss spectroscopy (EELS) and AUGER spectroscopy, the latter before and after oxygen cleaning procedure in ultra high vacuum (UHV) with high temperatures applied. From figure 2.13 and also later in this text in figures 2.33 and ??, the impurities calculate to values shown in table 2.3 ($\text{C} < 1 \%$) which is slightly higher than the best literature values showing

0.2 % carbon impurities.^[15] In figure 2.13 a carbon free single crystal of sapphire (red) is compared with a 50 nm ALD sample (black). Since no carbon is embodied in single crystal Al_2O_3 , the observed signal purely represents transport contamination. This explicates the origin of carbon impurities, giving rise to the fraction of internal contamination and surface impurities due to transport. Integration of the signals at 0.27 keV lead to a ratio of 1:2 proving at least half of the measured contamination being transport based.

The density of Al_2O_3 could be obtained using EDX (e.g. figure 2.13) together with the formula 4.2. The density was calculated to $3.05 \pm 0.3 \text{ g} \cdot \text{cm}^{-3}$ which is in good agreement to the best literature value of $3.5 \text{ g} \cdot \text{cm}^{-3}$.^[35]

Alumina films featured a minimum roughness, independent on the film thickness on SiO_2 -substrates. In the small scale, free of dust impurities, the roughness was often measured to range in between 0.3 and 0.5 nm. In figure 2.11 the maximum roughness is displayed, which corresponds to the difference of lowest and highest data point in a certain area. It was shown, that in areas below the micrometer length-scale rarely irregularities were detectable although larger dimensions showed existence of dust particles pegged into the film. Due to the large area of about $10 \cdot 10 \mu\text{m}^2$ scanned in figure 2.11, the amount of dust particles on the whole wafer can be estimated to several million irregularities covering a surface of $50 \cdot 50 \text{ nm}^2 \cdot 5 \cdot 10^8 = 1.25 \cdot 10^{12} \text{ nm}^2$, which is in other words a fraction of $1.25 \cdot 10^{-4} \%$ of the overall wafer surface. Although this is only a rough estimation Al_2O_3 can be utilized in scattering experiments since the influence of grains of dust is negligible.

The stoichiometry was determined by EDX using a single sapphire crystal as a reference which is depicted in figure 2.13. By integration of the corresponding Al (1.49) and O (0.52) signals, we observed a minor increase of the oxygen content, leading to a sum formula of $\text{Al}_2\text{O}_{3.5}$ (figure 2.13, black) instead of Al_2O_3 (figure 2.13, red). According to the ellipsometry fitting aluminium oxide is suggested to be in normal stoichiometry form, precisely because of the well applicable fit function (figure 2.12). The alumina layer on top of a metal showed high resistivity and no crystallinity which

was verified by X-ray diffraction (XRD): showing no signal in all applied measurements including PLD laser irradiation recordings, where an annealing effect was expected. In addition, TEM experiments, e.g. high resolution transmission electron microscopy (HR-TEM) images in this work showed that no order was observable and furthermore TEM electron diffraction leading to no diffraction pattern which proves the disordered structure. All these promising results led to the use of alumina as a part of the composite material described in chapter 2.3.

Catalyst Improvement with Aluminum Oxide

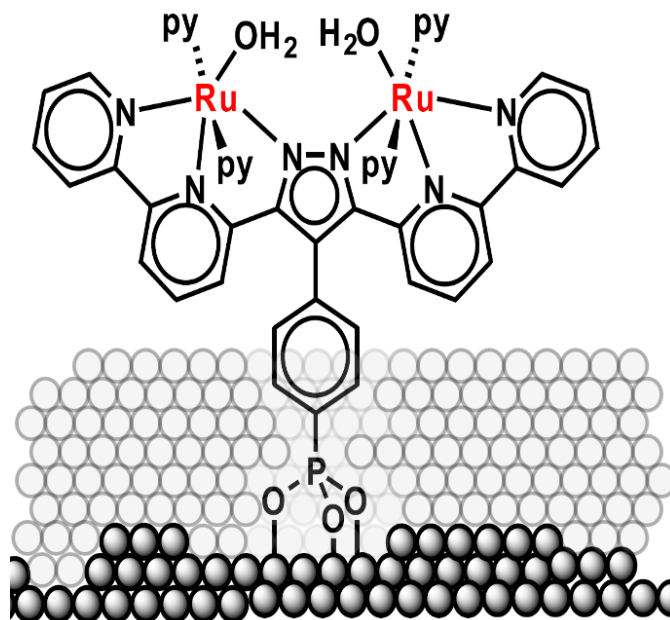


Figure 2.14: Bimetallic ruthenium based water oxidation catalyst anchored by ALD- Al_2O_3 (gray atoms) on a SiO_2 wafer (black atoms).

Within the scope of a cooperation, Al_2O_3 was used to increase the anchoring strength of a catalyst molecule on a surface employed in a water oxidation reaction. Previous to this experiment, J. ODROBINA anchored a dinuclear ruthenium water oxidizing catalyst (shown in figure 2.14) with a phosphate group on glass but found that catalyst activity dropped due to hoist of the molecule to solution. Following literature procedures, low temperature depositable oxides are usually used to fasten molecules to the surface such as TiO_2 ^[206] or Al_2O_3 ^[207] also allowing for larger pH spans in queued up experiments. In the ALD experiment, a rotating disc electrode with catalyst load was glued to the sample holder and covered with about 1 - 1.5 nm Al_2O_3 using five deposition cycles at 60 °C, minding catalyst decomposition. An inconspicuous color change of the electrode (compare to chapter 2.3) indicated deposition success. Further catalysis experiments did not exhibit longer lifetime or higher turnover numbers and frequencies.

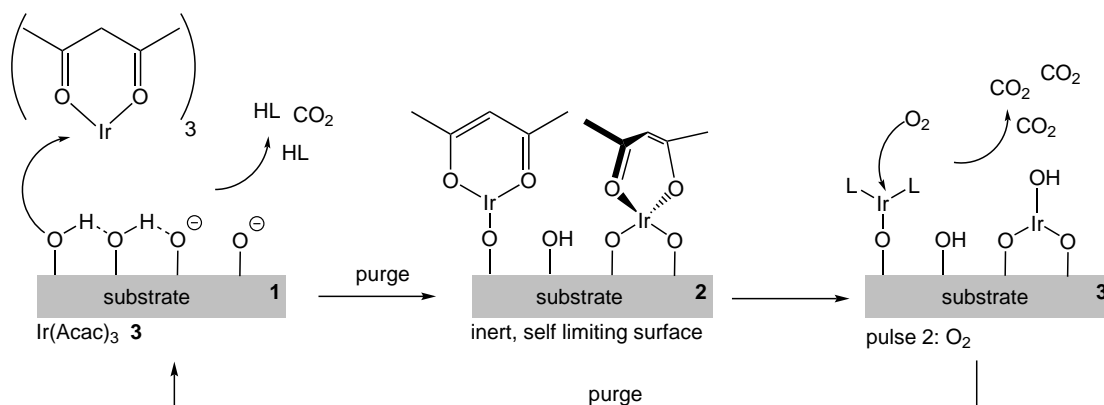


Figure 2.15: The mechanism of Iridium deposition with oxygen at high substrate temperatures. **1:** Reaction with the surface holding different oxygen sites (protonated or basic), releasing ligand or CO_2 , depending on reaction pathway, substituting a ligand **2:** self-limiting ligand protected surface after purge phase. **3:** Ligand oxidation and reactivation of the metallic surface.

2.2.2 Iridium

One of the most prominent example of high temperature deposition - for both evaporation of the precursor and the substrate - was a first generation 2,4-pentanedionato based Iridium precursor.^[208] We chose this to evaluate the limits of the chamber, ALD valves, and heating of the precursor bottles. $\text{Ir}(\text{Acac})_3$ (**3**) is highly symmetric and features a fairly high molecular mass. Therefore, it is difficult to evaporate. Although it was stable in ambient conditions for minutes, it can react in the gas phase^[209,210] (CVD) or on a hot substrate^[208] with oxygen to form thin iridium metal films in an ALD fashion. Iridium thin films may also serve as metallic interlayers for phonon blocking, because of moderate inert behaviour to oxygen and water, the very high melting point of $2443\text{ }^\circ\text{C}$ ^[209], high density, and crystallinity on oxide materials.^[208] Furthermore, it defined the borders of physical parameters possible in the novel set-up.

The deposition was tracked via MS to evaluate and reproduce the literature procedures. Taken after some initiation cycles (the first cycles often showed higher precursor concentration, due to long initial heating and are thus not representative.), the MS shows very nicely the exhaust of CO_2 during the pulse of oxygen indicates

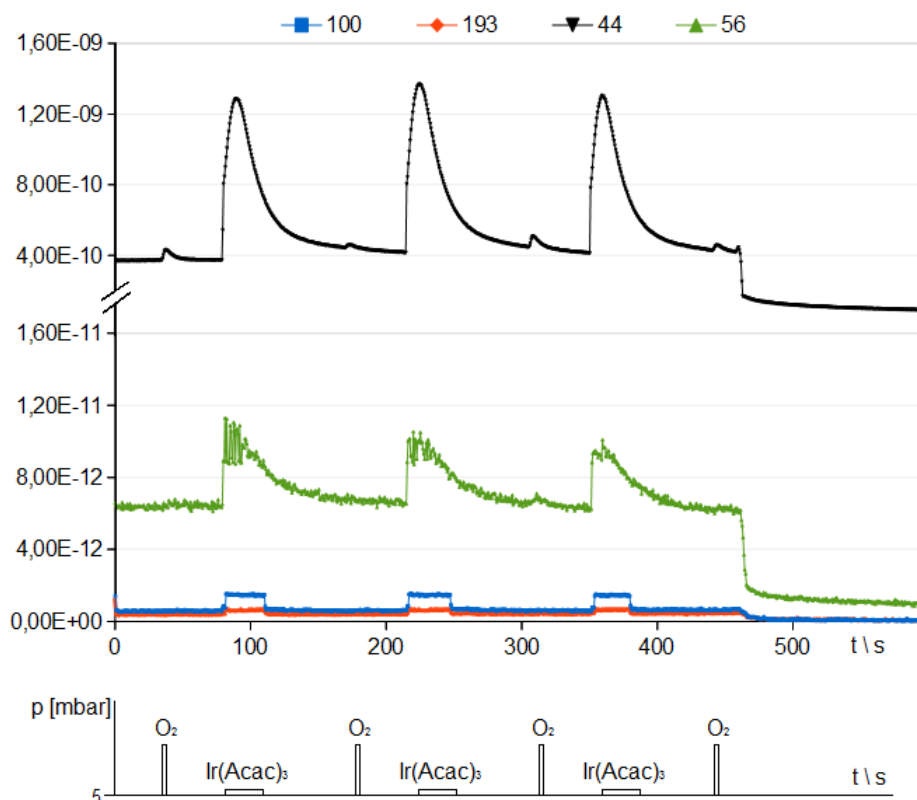


Figure 2.16: MS investigations on Iridium depositions using **3** and O_2 tracking CO_2 (black) generation ($m/Z = 44$). Additionally ligand fragment desorption was tracked: Acac ($m/Z = 100$, blue) and its main EI-MS fragment C_3H_5O ($m/Z = 56$, green). Below plotted the schematic ALD cycles with respect to pressure increase. $p = 5$ mbar indicating continuous purge flow of N_2 . After 450 s the MS was closed.

surface coverage with carbon species like ligand(s), which allow for the ALD mechanism. This is furthermore supported by the release of ligand fragments (figure 2.16, green) in the third oxygen pulse. However, this signal turned out to be quite small and not detectable in every cycle. Furthermore, it was proven that no complete ligand was cleaved with the track of acetylacetylen (Acac) (blue) showing no increase during the oxygen pulse.

The resulting layers were metallic in appearance and conductive which was checked with a multimeter. Further investigation show a minor small scale maximum roughness of < 7 nm which was an improvement to literature values reported previously > 7 nm.^[47] However, the average roughness was comparably low (table 2.1). It was

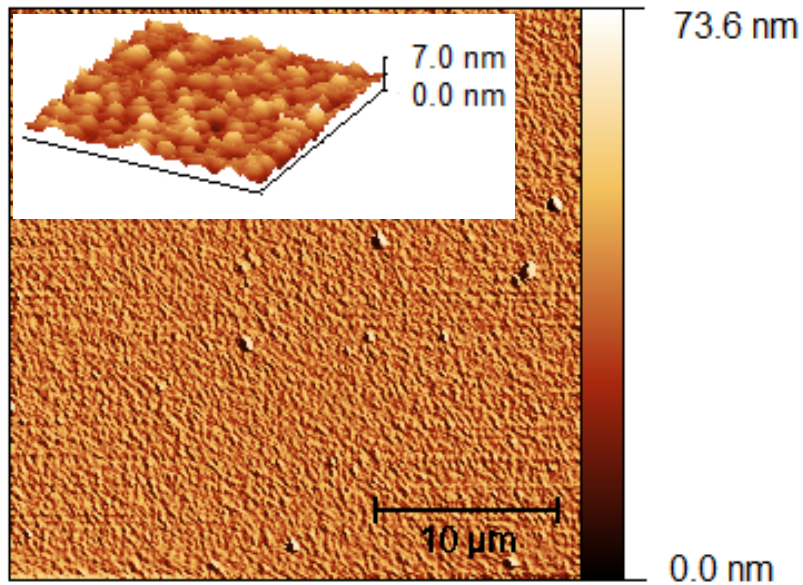


Figure 2.17: AFM analysis of a 30 nm iridium film showing large ($30 \cdot 30 \mu\text{m}^2$) and small scale ($1 \cdot 1 \mu\text{m}^2$) maximum roughness in a height image.

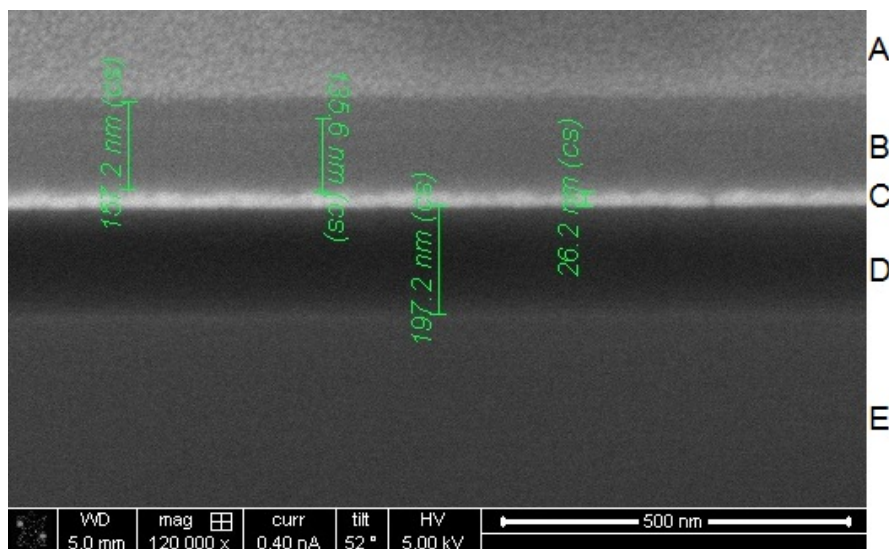


Figure 2.18: SEM image of 30 nm metallic iridium (layer C) on substrate SiO_2 on Si (D and E) covered with electron-beam deposited platinum (A and B).

calculated to 1.3 nm, including the dust particles. Large scan areas revealed a low dust particle concentration displayed in figure 2.17. This roughness was furthermore confirmed by cross section SEM, proving iridium to be metallic and dense by comparison of the brightness of layer C and B in figure 2.18, showing a strong contrast of electron beam deposited Pt and ALD-Ir. Although the layer is conductive, holes are visible in this picture. Figure 2.19 shows the film content for a 10 nm iridium film as determined by X-Ray photoelectron spectroscopy (XPS). Signals for carbon and oxygen could be observed, whereas the oxygen contamination impurified the sample much more. Although some of the oxygen signal (at 550 eV) may arise from SiO_2 , since underlying substrate is visible in the range of 150-225 eV, oxygen in the iridium film was present.

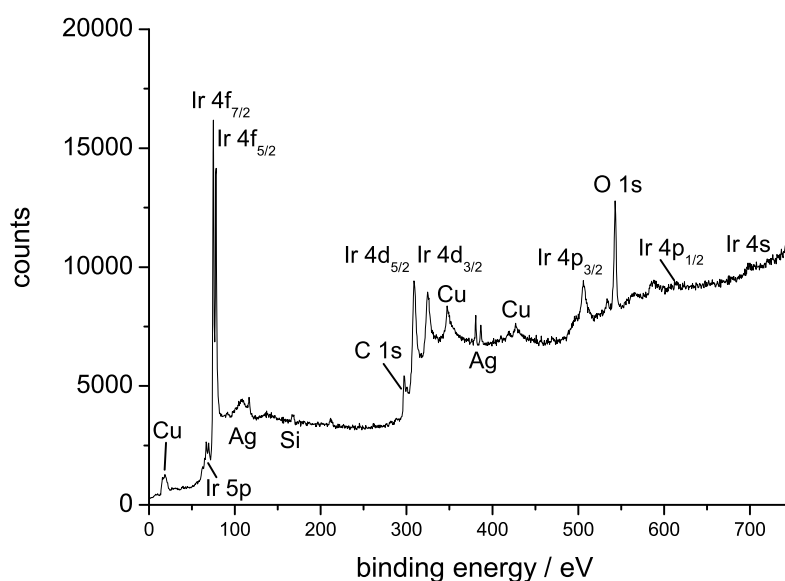


Figure 2.19: XPS spectrum of a metallic iridium layer of about 15 nm. Signals visible in addition to the ALD-film are substrate signal (Si and O), the glue from wafer fixation (Ag) on the sample holder (Cu).

Beneficially, only a very minor carbon impurity fraction could be observed. Comparing these results with the best literature values, which can be found in a three-step synthesis of iridium films utilizing additional hydrogen gas after the oxygen

pulse for cleaning purposes, oxygen impurities are more pronounced than carbon impurities in comparable dimensions of amounts and ratios, respectively.^[48]

Both findings concerning impurities proved the presented films to be more flawless in comparison to literature, especially considering the lack of the cleaning properties of H₂, utilized by LESKELÄ *et al.*.^[48]

Therefore, this experiments proved a theoretical ALD window coverage of the chamber of 25 - 350 °C which is expected to be sufficient for the investigation of novel deposition strategies.

With the measured disadvantage of holes, high evaporation temperatures and no significant decrease of the surface roughness, iridium was discounted for the generation of multilayer structures.

Table 2.1: Comparison of prepared and literature iridium material pivotal properties. Data of prepared films originates from AFM, XPS and SEM. In literature, the growth rate was highly dependent on the substrate temperature which is shown by the displayed numbers. However, the number in parentheses refers to the same parameters as the prepared sample.

Feature	Thesis samples	Literature	Citation
Roughness [nm]	1.3	0.5 - 1.6	[208]
Impurities (C)	0.75 %	≤ 1 %	[48]
Impurities (O)	4.2 %	4-7 %	[48]
Growth rate [gpc]	0.5 ± 0.1	0.2-0.6 (0.45)	[208]

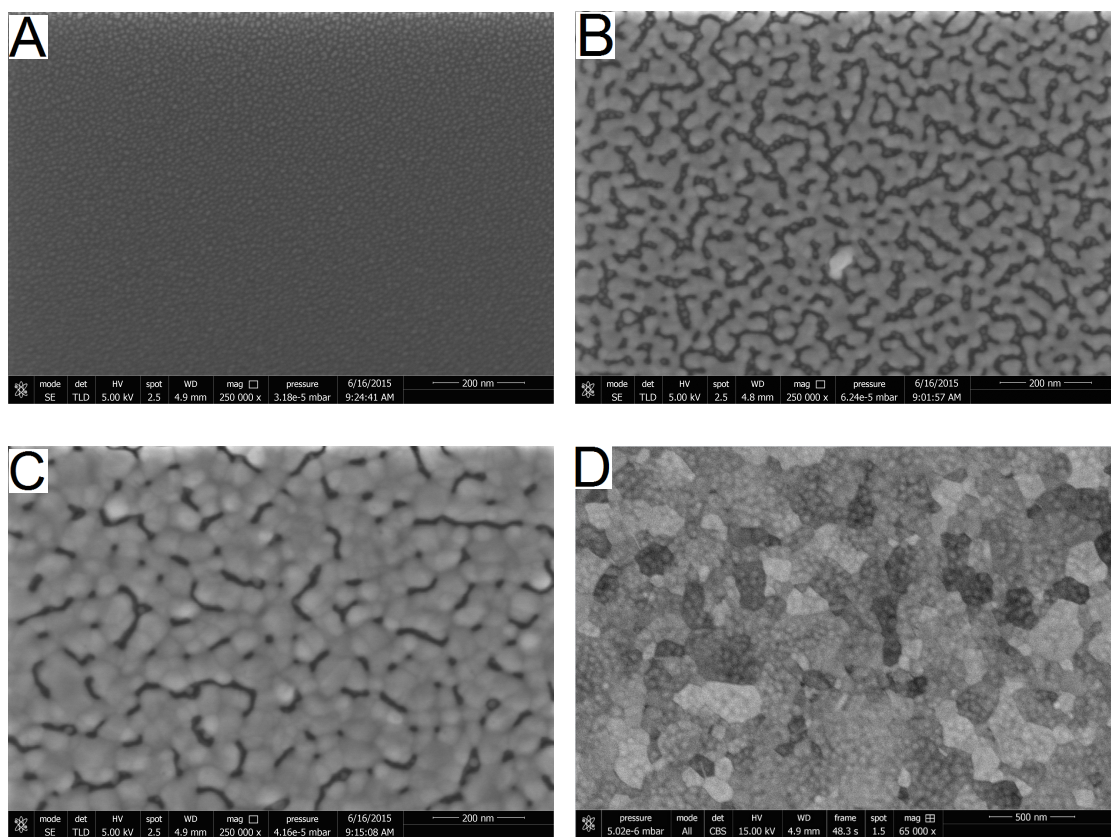


Figure 2.20: SEM images of a SiO₂ wafer exposed to 25 [A], 50 [B] and 100 [C] cycles of Pt deposition using MeCpPtMe₃ and Oxygen. [D] depicts a SEM image with a CBS detector being applied to a 50 nm Pt specimen made by 300 Cycles showing single crystal domains orientation.

2.2.3 Platinum

Platinum metallic layers could be successfully prepared using thermal platinum-ALD literature procedures^[49] applying alternating MeCpPtMe₃ (**2**) and oxygen to a SiO₂ surface. As described in literature,^[119] platinum was found to form typical island growth on insulator substrates. A substrate change from SiO₂ to MgO resulted in islands of larger diameter, as determined via AFM. This initial phase during the growth is depicted in figure 2.20 [A-C]. The experiment showed correlation of applied deposition cycles and surface coverage in the initiation phase of Pt deposition, detected by SEM. [A] shows the first step of platinum deposition, forming a regular surface coverage with small islands ranging from 3-10 nm in diameter and a surface

coverage of about 50 %. With an increase of the number of deposition cycles, we could show their development in image [B]. It was proven that small hot droplets of platinum accumulate to larger islands if above a critical size or below a critical distance to each other. In Figure [B] domains are visible already within the in-plane length scale of 20 to 50 nm with additional small particles forming droplets in between new bigger islands proving prior migration. With additional cycles the film closes with domains of 20-100 nm size depicted by [C] and [D]. Thickness dimensions can be achieved from perpendicular view using TEM in section 2.3 showing flattened droplets with 8-10 nm in maximum height.

Figure 2.21 and 2.22 demonstrate the maximum roughness of platinum on a SiO_2 substrate with unblemished homogeneity over a large scan area. Both AFM, especially the zoomed 3D-Image, and scanning tunnelling microscopy (STM) showed the verified island growth heritage: although the layer was closed, conductive and of metallic appearance, the roughness

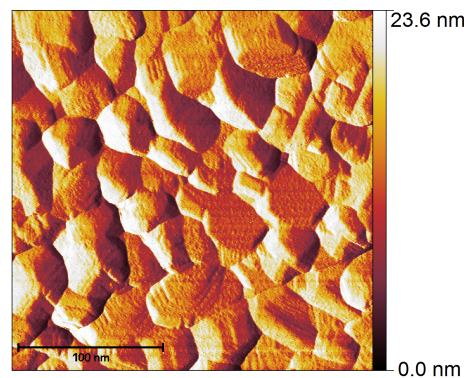


Figure 2.21: Scanning tunnelling microscope image of a conductive platinum film on SiO_2 made with 200 ALD cycles showing a height profile.

remained higher than found for isolators in chapter 2.2.1. Despite the increased roughness, one advantage was given by the absence of dust particles, since the surfaces remained clear of larger irregularities.

As shown in figure 2.23, platinum was perfectly ordered, showing typical $[111]$ ^[119] orientation in the 2θ -XRD-scan. In disparity of this observation, the orientation of described islands parallel to the substrate surface was highly disordered as shown in figure 2.20 [D] using a CBS detector to visualize the domain structure of Pt. The observation of high crystallinity was later reproduced by TEM diffraction in multilayer

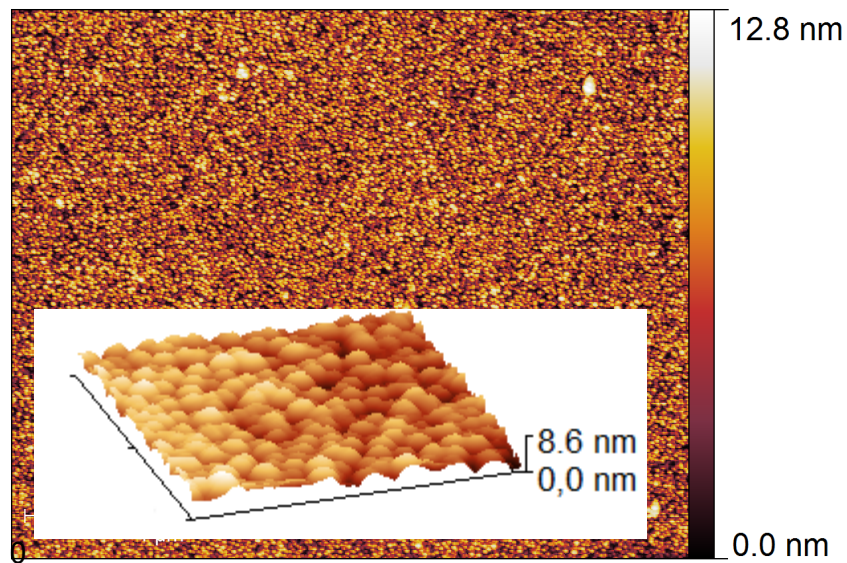


Figure 2.22: Atomic force microscopy analysis of a 50 nm platinum film showing large (plan view, $8 \cdot 10 \mu\text{m}^2$) and small (3D view, $1 \cdot 1 \mu\text{m}^2$) scale maximum roughness shown in a height profile.

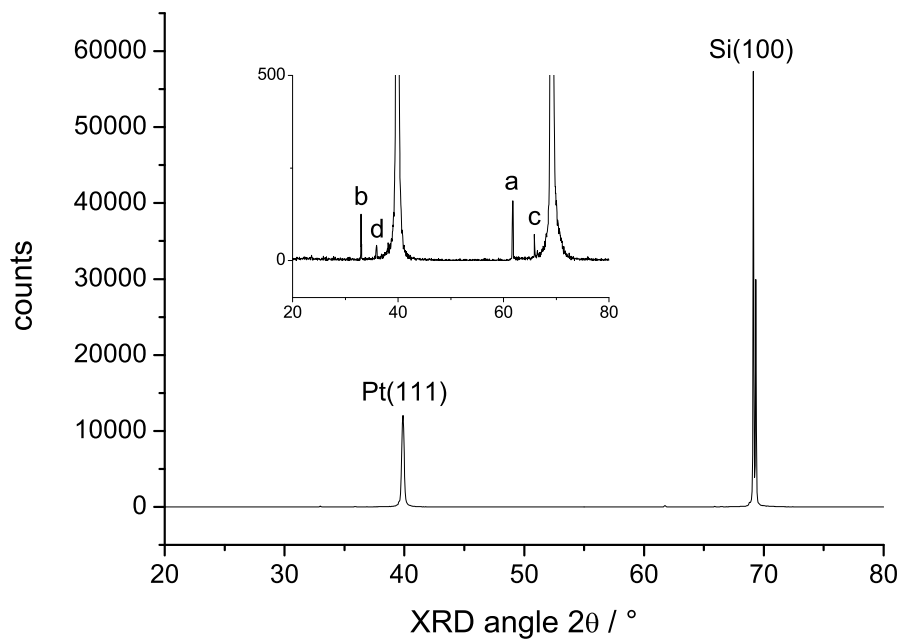


Figure 2.23: 2θ -scan of an about 15 nm thick platinum film on 200 nm SiO_2 on Si substrate. Smaller impurities (a-d) are shown in inlet and correspond to the sample holder.

structures. *In-situ* LEED measurements were performed, but the domain disorder of the structure and also the roughness inhibited measurement success.

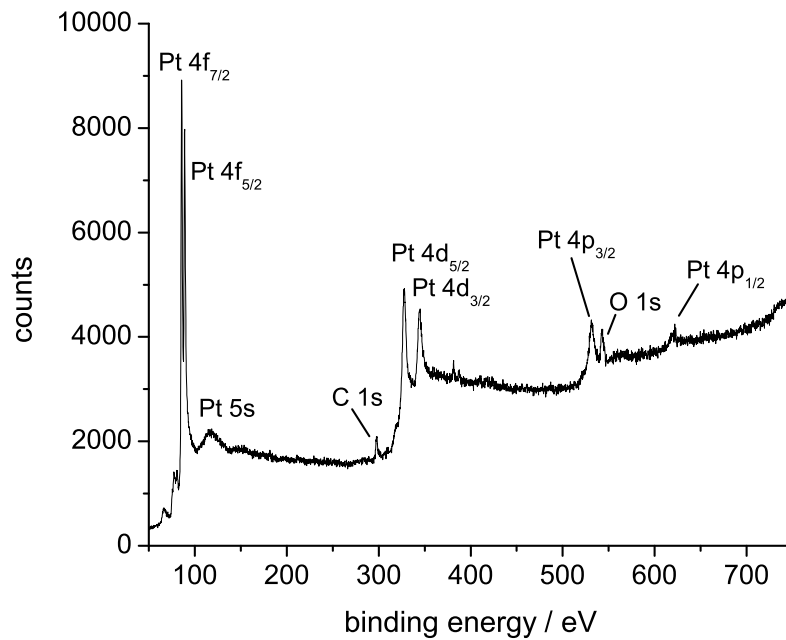


Figure 2.24: XPS of a 15 nm platinum film. Indexed orbitals contribute to the calculation of impurity content. Very small signals at 385 eV are silver glue.

As a crucial limitation for many experiments using ALD samples, the amount of impurities in and/or on the deposited material has to be evaluated inevitably. These could be estimated by integration of XPS signals although carbon and oxygen impurities were expected larger than real values due to contamination during transport. The calculated data are listed and compared in table 2.2 showing small deviation of both values: slightly higher values result from non-use of sputtering procedures after transport. Condensing the presented findings, it was shown that impurities calculated to lower values, compared to literature.^[49,75,77,78,119,211] This was shown previously in chapter 2.2.2 and this recurrence proved again the outstanding possibilities of the presented set-up.

Moreover, table 2.2 shows a very interesting aspect of highly increased growth rate

of the presented platinum deposition. It cannot be finally excluded, that this finding originates from the oxygen background, but experiments with higher concentrations (figure 2.27 for example) shows different depositional behaviour, like roughness increase by orders of magnitude in this particular case. Here, this was not the case, so one can address the outstanding gpc rate to the set-up geometry, the fact of mild collision and the feature of multiple interactions with the substrate surface, especially with respect to the stable precursor.

In conclusion, platinum thin films displayed in this chapter showed not only improved film properties due to well chosen parameters and the novel reactor design compared to recent literature, but furthermore represent a perfect source for metallic interlayers in special structures shown in the next chapter. Especially the very low impurity contribution and the highly ordered and conductive structure lead to the decision for application.

Table 2.2: Comparison of prepared and literature Pt material pivotal properties. Literature values refer to depositions with the same or very similar deposition parameters.

Feature	Thesis samples	Literature	Citation
Roughness [nm]	0.98 (10)	4.0; 0.7 ± 0.3	[49,211]
Impurities (C)	2.39 (20) %	< 5.0 %	[211]
Impurities (O)	2.41 (20) %	< 5.0 %	[211]
Domain size diameter [nm]	25-50	ca. 20	[77,119]
Growth rate [gpc]	0.75 ± 0.1	0.45 ± 0.05	[49,75,78]

2.3 Materials for Phonon Spectrum Tuning

2.3.1 Application for ALD Thin Films: Nanolaminates

As a cooperation project in the CRC 1073 subgroup A, a novel tailored material was synthesized. To address the general idea of understanding energy transport (as described previously in chapter 1.3.1), a deposition strategy was evaluated of following deposition procedures to build high interface density materials. Two materials were chosen from the reactor testing phase, namely Al_2O_3 and platinum. The fact that both materials can be deposited onto each other^[201,202], strong difference in structural parameters, heat capacity, and Young's modulus, additionally to their availability renders them perfect candidates for sandwich structures (see 1.3.1). As depicted in figure 2.25, platinum growth rates did not change with underlying oxide material. Here, 300 ALD cycles were conducted for both metal and oxide source forming three layers on SiO_2 , showing on the one hand good reproducibility of platinum thickness (the layer's thickness on SiO_2 is 19-26 nm and 18-23 nm on Al_2O_3 , respectively) and - on the other hand - slightly higher growth rates on SiO_2 -substrates than on Al_2O_3 . This can be explained by higher ordering and increased lattice mismatch on silica, as it was shown for MgO previously. Furthermore, we aimed for the thinnest interlayer possible of both platinum and Al_2O_3 . Figure 2.26 shows a structure of increasing platinum thickness forming interlayers between consummately constant Al_2O_3 . The number of ALD cycles was increased by 50 for each Pt-layer, increasing

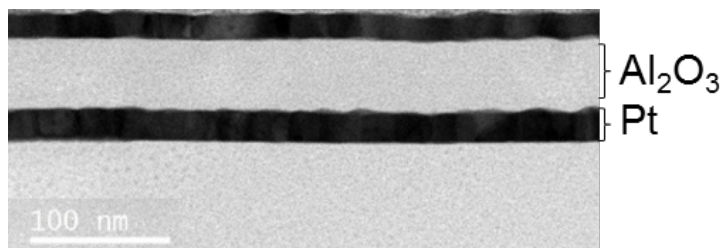


Figure 2.25: TEM image of a sandwich structure showing reproducibility of Pt on SiO_2 (bottom Oxide) and Al_2O_3 (interlayer Oxide). All Layers were deposited using 300 cycles showing the difference in growth rates.

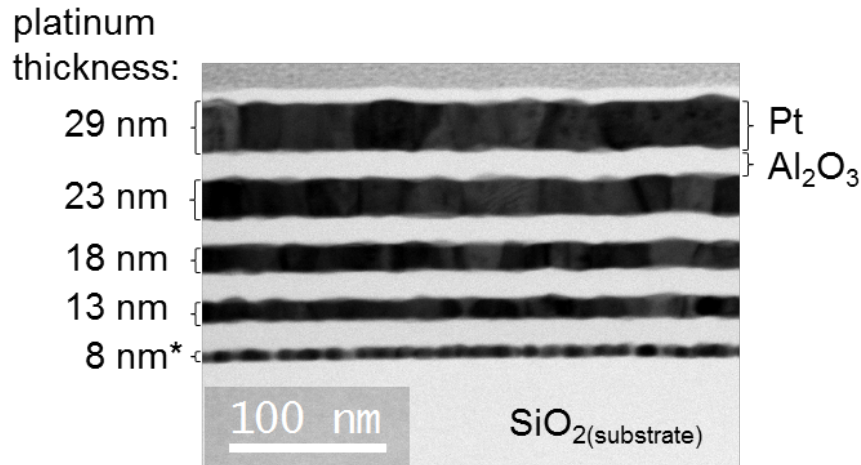


Figure 2.26: TEM image of a sandwich structure on SiO₂ substrate with increasing Pt thickness and constant Al₂O₃ showing eleven interfaces. (Prepared with 100 cycles Al₂O₃ and 50, 100, 150, 200, 250 iterations for Pt.)

the thickness linearly by about 5 nm each, as anticipated. 100 cycles of TMA and water were used repetitively generating Al₂O₃, forming 17 ± 0.3 nm oxide layer advantageously exhibited minimum variation.

Nevertheless, both of these pictures showed first examples of these multilayer compositions and were therefore of great interest to study energy transport perpendicular to the boundaries. Through the collaboration within the CRC 1073, tailored structures were generated by the author and structural properties in respect of energy intake were investigated in two experiments. In addition to the depicted structures, two more nanolaminates were synthesized, increasing the interface density much further: 600 nm of Al₂O₃ was deposited, symmetrically intermittent by 10 nm of platinum, forming ten (assay ALD 3) and twenty (assay ALD 4) interfaces in this 600 nm by five and ten platinum interlayer. Furthermore, copper was deposited on top as a light absorber using PLD but TTR-investigation was still pending by the time this thesis was written.

Since the reproducibility of the interlayer deposition strategy was proven previously, a further characterization by TEM was omitted, as this would have been invasive.

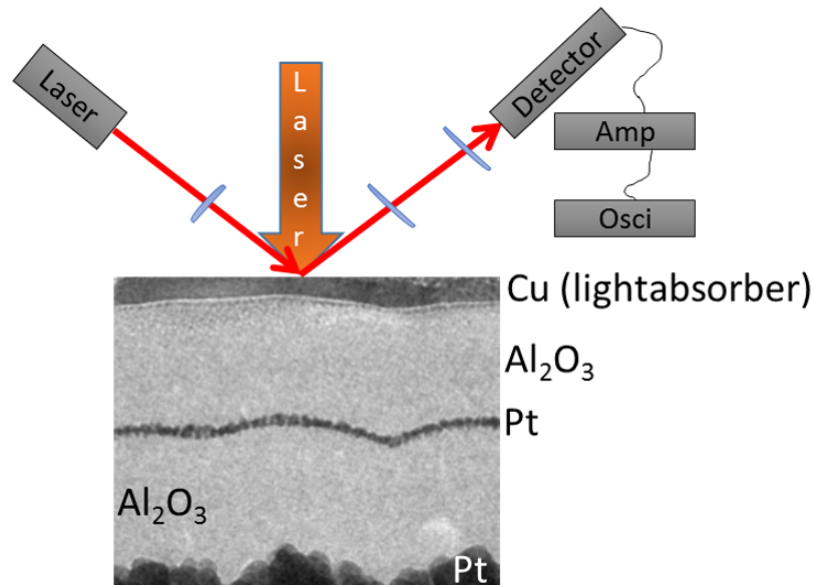


Figure 2.27: Schematic view on the TTR experiment^[165] with TEM image of the investigated structure, assay ALD 2, green in figure 2.28.

Thermal Conductivity of Atomic Layer Deposited Thin Films of Platinum and Aluminium Oxide

TTR was used by F. DÖRING to investigate the heat transport into a material and the theory was described in chapter 1.3.1. As displayed in figure 2.27, 50 nm of copper was deposited with PLD^[213,214] on two ALD samples and single crystalline [0001]-Al₂O₃ (4.3) acting as a light absorber strongly increasing the surface roughness. Two lasers are used in this experiment: while the first one is continuously reflected from the surface (red in figure 2.27) with permanent detection of the amount of photons, a second laser (orange in figure 2.27) excites at $t = 0$, resulting in a very fast temperature increase which dissipates into the material within microsecond fractions. The measured change in reflected light intensity can be expressed in terms of a temperature change. The normalized surface temperature is depicted in figure 2.28 showing the laser incidence at $t = 0$ and deexcitation/dissipation afterwards for three samples. Pure Al₂O₃ with light absorber are shown in black (“Al₂O₃”, single crystal) and red (for the amorphous ALD sample with no platinum). Nanolaminare sample ALD 2

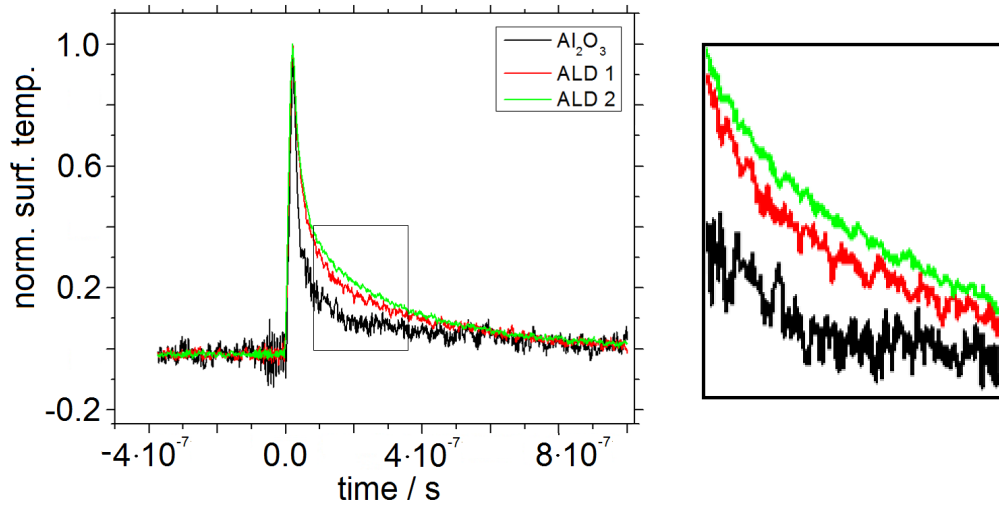


Figure 2.28: Transient temperature-dependent reflectivity measurement of three different samples ([0001]-single crystal Al_2O_3 (black), about 400 nm ALD-deposited Al_2O_3 (red) and Al_2O_3 with interlaying Pt (green, 2.27)) showing the effect of interlayers on energy dissipation by normalized surface temperature change. The highlighted section on the right-hand side displays the separation of the graphs.^[212]

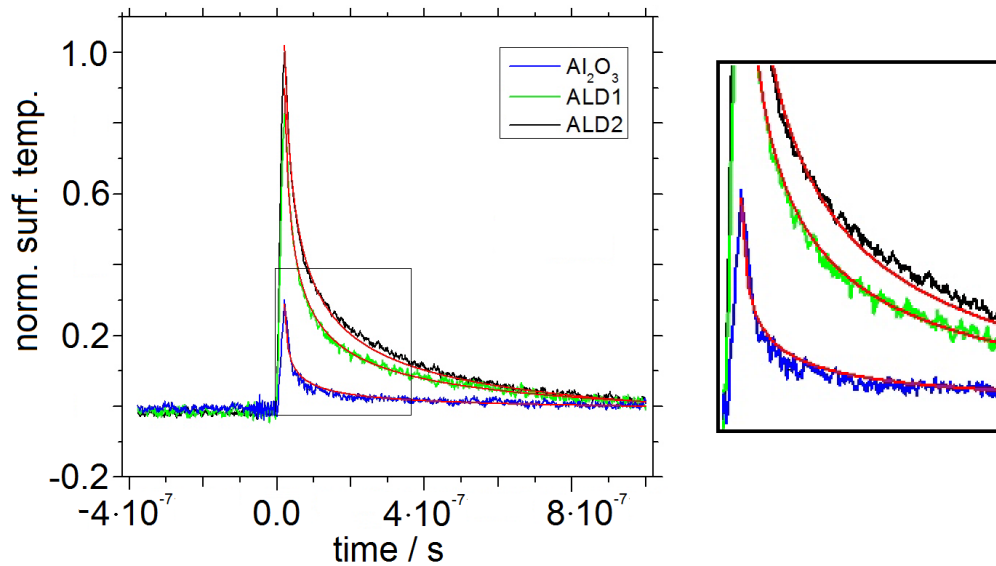


Figure 2.29: Transient temperature-dependent reflectivity measurement of three different samples ([0001]-single crystal Al_2O_3 (blue), about 400 nm ALD-deposited Al_2O_3 (green) and Al_2O_3 with interlaying Pt (black, 2.27)) showing the effect of interlayers on energy dissipation by normalized surface temperature change without rescaling to the highest heat signal. Red lines fit the experimental data are used to determine the final heat capacity. The highlighted section on the right-hand side displays the separation of the graphs and the strong difference in maximum temperature reached in single crystal compared to amorphous ALD assays.^[212]

(green curve) reflects the averaged data of HR-TEM image sample in figure 2.27 where 200 nm Al_2O_3 is divided by platinum interlayers of about 8 nm thickness. The bottom platinum interlayer of 90 ± 17 nm was very rough due to high oxygen concentration in the background / purge gas of the chamber during the deposition. Indicating the strong disorder in amorphous ALD-samples, temperature decrease in $[0001]\text{-Al}_2\text{O}_3$ turns out to be much faster compared to the ALD assays. Furthermore, the initial temperature increase of the crystalline sample was lower at $t=0$ which is depicted and highlighted in figure 2.29. Since the spread of energy is driven by phonon excitation, this is expected: lattice vibrations are hindered by defects or lattice mismatches. A highly ordered structure therefore leads to a much faster energy equilibrium and conducts thermal energy efficiently. Conductivities measured by TTR amount to about 46 W/mK for the $[0001]\text{-Al}_2\text{O}_3$ reference material, which almost equals the literature value of 42.5 W/mK^[215] within error bars.^[165]

The thermal conductivity of the ALD 1- sample was found to be much lower. Derived from the TTR result, one can approximate the thermal conductivity of the amorphous Al_2O_3 to a value around 6 W/mK. Although the underlying SiO_2 -layer's distance to the surface is about 450 nm, an influence of its very low thermal conductivity of about 1.3 W/mK cannot be excluded.

As a second outcome, the ALD 2 sample shows an even slower energy dissipation which can now be attributed to the influence of the interlayers. F. DÖRING calculated a thermal conductivity of 1.6 W/mK. Although platinum has been added, which has a significantly higher thermal conductivity of 72 W/mK^[216] and one could expect a faster transport, this is a further reduction by the factor of four. Even more interesting, the contribution of silica to the overall conductivity is smaller, since the layer system is thicker than expected.

The effect of interlayers on heat transport by thermal boundary resistances was discussed in chapter 1.3.1, and can be described in the presented structure by the dominating factor of different density of phonon states at the two sides of the boundary, to adduce the diffuse mismatch model due to moderate roughness. The

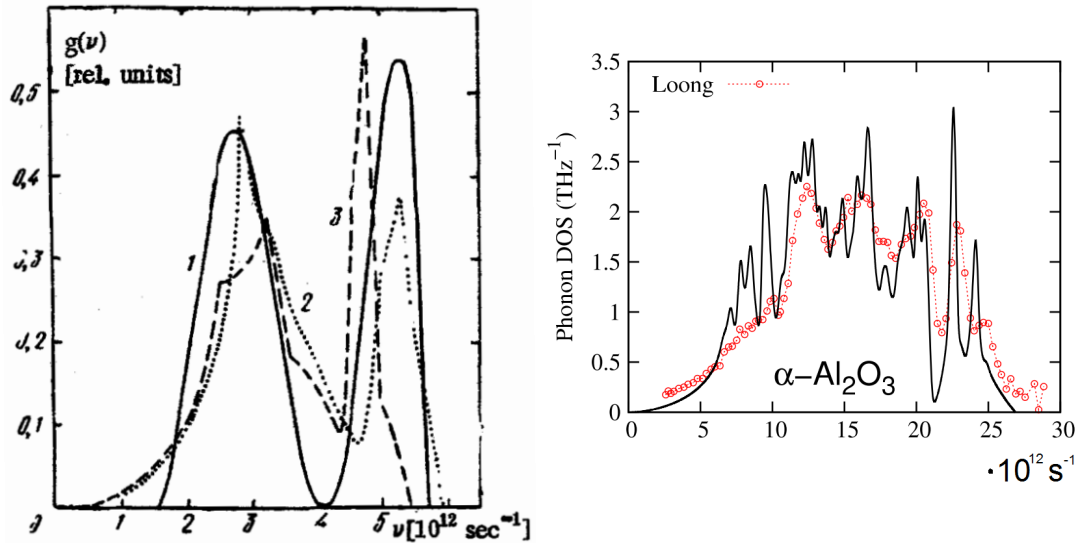


Figure 2.30: Phononic density of states (calculated) in utilized materials of the presented nanolaminates. Taken with small changes from KORSHUNOV *et. al.* (1980) (left, platinum) and WANG *et. al.* (2010) (right, Al_2O_3)

calculated DOS for phonon excitation is shown in figure 2.30 for comparison. Here, platinum shows two maxima at 2.7 and 5.5 THz and no phonons above 6 THz.^[217] The highest density for Al_2O_3 can be found at 23.0 THz with population just up to 27 THz.^[218] One can therefore state that the very small overlap thwarts the propagation of phonons efficiently both from Al_2O_3 to platinum and vice versa. Furthermore, it is possible that island growth and the existence of platinum domains with defined boundaries parallel to the heat flow may lower the thermal conductivity of the platinum in addition to its very thin layer size compared to the bulk property. With a boundary resistance of about $10^{-6} \text{ m}^2\text{K/W}$ our system shows good agreement with comparable literature values.^[219] Furthermore, the effect of a single interlayer is not visible in most cases and shows the potential of the investigated ALD assays. It has to be proven with further experiments, that e.g. for thicker/thinner layers, values for interlayer-free ALD-samples can be reproduced proving the influence of SiO_2 to be negligible. Furthermore, already prepared multi-interlayer samples, holding ten and twenty interfaces, need to be investigated, proving the boundary conductance to be the dominating effect reducing heat transport. In addition, this materials can

also show the effect of high roughness in ALD 1, since interfaces are expected to be much smoother in these assays.

Rydberg Atom Tagging with Thin Aluminum Oxide on Platinum

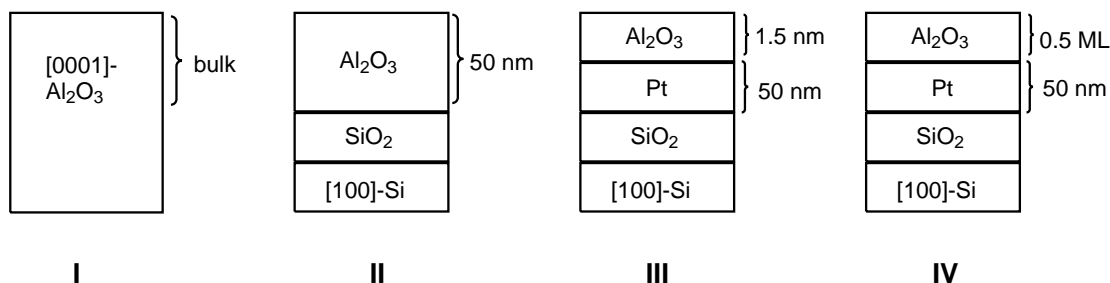


Figure 2.31: Schematic drawing of samples utilized in RAT-experiments.

In another experiment in cooperation with the BÜNERMANN group (A04, CRC 1073) we investigated Al₂O₃/platinum samples, displayed in figure 2.31. Using thinner oxide layers on metals than have been shown in literature before, we tried to answer the question, how thin a layer needs to be, to hide underlying materials properties. For this purpose several structures were synthesized with Al₂O₃ on Platinum in different thicknesses. The TEM image in figure 2.35 (a) shows shows one of these materials: A 50 nm thick platinum layer acting as bulk support was capped with a very thin layer of Al₂O₃ and later compared with 50 nm of ALD deposited Al₂O₃. For the metallic underlying layer we decided to choose platinum because scattering properties were available from bulk experiments with hydrogen atoms from previous testing procedures. Finally, these were compared with single crystalline [0001]-Al₂O₃ and [111]-platinum. The layers were grown with ALD using 1, 5 and 300 cycles TMA **1** and water, platinum layers were grown using 500 cycles of MeCpPtMe₃ **2** and oxygen. The thickness of Al₂O₃ in sample **III** and **IV** was difficult to measure to the small number of cycles run. As shown in figure 2.35 (b and c), utilizing EELS-mapping in HR-TEM measurements gave rise to an approximate value which was in perfect agreement with the previous gpc findings in section 2.2.1. With five ALD cycles we were able to fully cover the surface with an oxide layer of about 1.0 to 1.5 nm thickness, corresponding to 4-5 monolayers. Although measurement was not possible over the whole range of the lamella, due to platinum roughness over-

lay in picture's depth, aluminium content was detectable uniformly throughout the surface, proving complete homogeneous coverage. This is furthermore backed by Auger spectroscopy measurements of both samples displayed in figure 2.33. Here, platinum signals arise at 42 and 63 eV, which are overlaid by the aluminium signal at 50 and 66 eV, which can be nicely seen by the green plot showing both platinum and aluminium generating a shoulder in the second signal, vanishing for the pure Pt, shown in cyan. Isolated weaker signals of platinum arise at 148, 156, 165 and 233, 248, 262 eV. Very minor signals at 353 and 386 are almost not visible.^[220]

Further elements can be identified: intense oxygen signals at 470, 488, 510 are isolated while 78 and 91 cannot be detected in every spectrum. Signal for carbon had been anticipated at 273 and 242 eV. The absence can be explained by the previous finding of very low carbon content in the film and furthermore by a successful cleaning procedure removing transport contamination. Integration of signals gave the surface coverage for the ML- Al_2O_3 -sample, since one can easily see the intensity of oxygen in **IV** (cyan) is larger than pure platinum, exposed to oxygen (blue) calculating to Al_2O_3 -oxygen. Different measurements lead to a value of 40-70 % which is far higher compared to literature

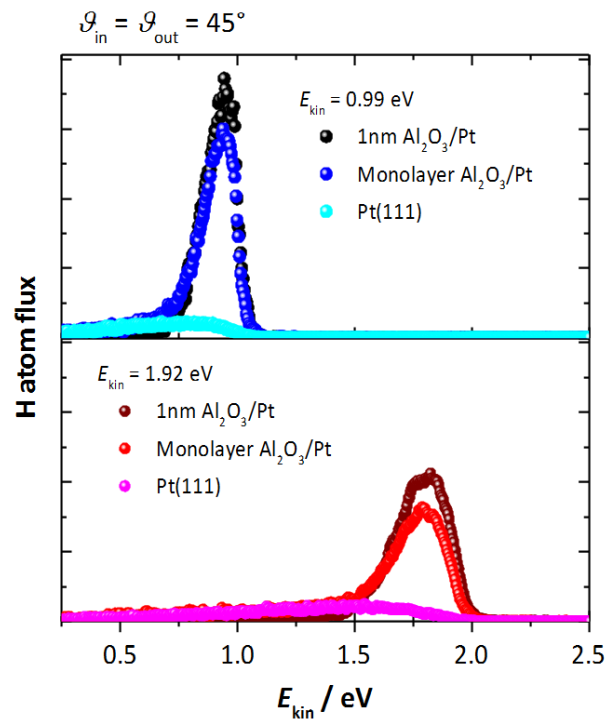


Figure 2.32: Hydrogen flux scattered from different interfaces with two different acceleration energies (one eV in the upper spectrum and two eV in the lower graph), comparing ALD one and five cycle experiments with bulk [111]-Pt sample.^[221]

sample, since one can easily see the intensity of oxygen in **IV** (cyan) is larger than pure platinum, exposed to oxygen (blue) calculating to Al_2O_3 -oxygen. Different measurements lead to a value of 40-70 % which is far higher compared to literature

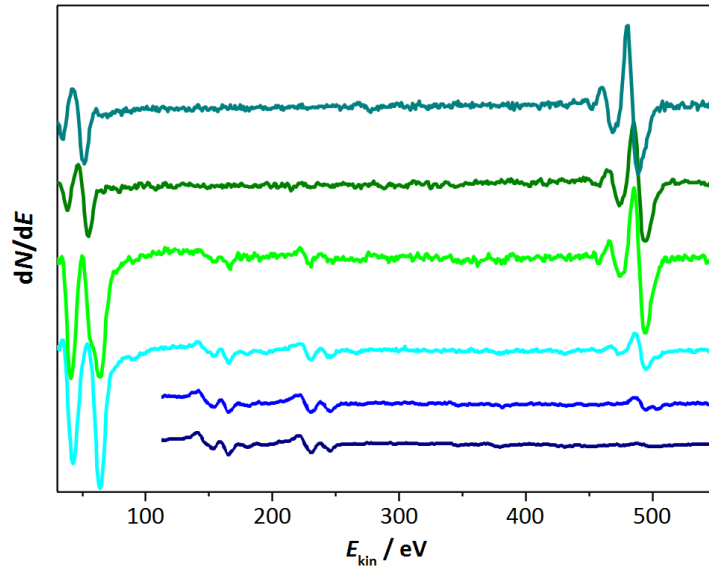


Figure 2.33: Auger spectrum of different samples in RAT experiment: from top to bottom these are [0001]- Al_2O_3 (pacific), 50 nm Al_2O_3 (moss), 1 nm Al_2O_3 (green), 1 ML Al_2O_3 (cyan), maximum chemisorbed oxygen (blue) on clean Pt [111] single crystal (dark blue), corresponding to 25 % coverage, derived from LEED data.^[221]

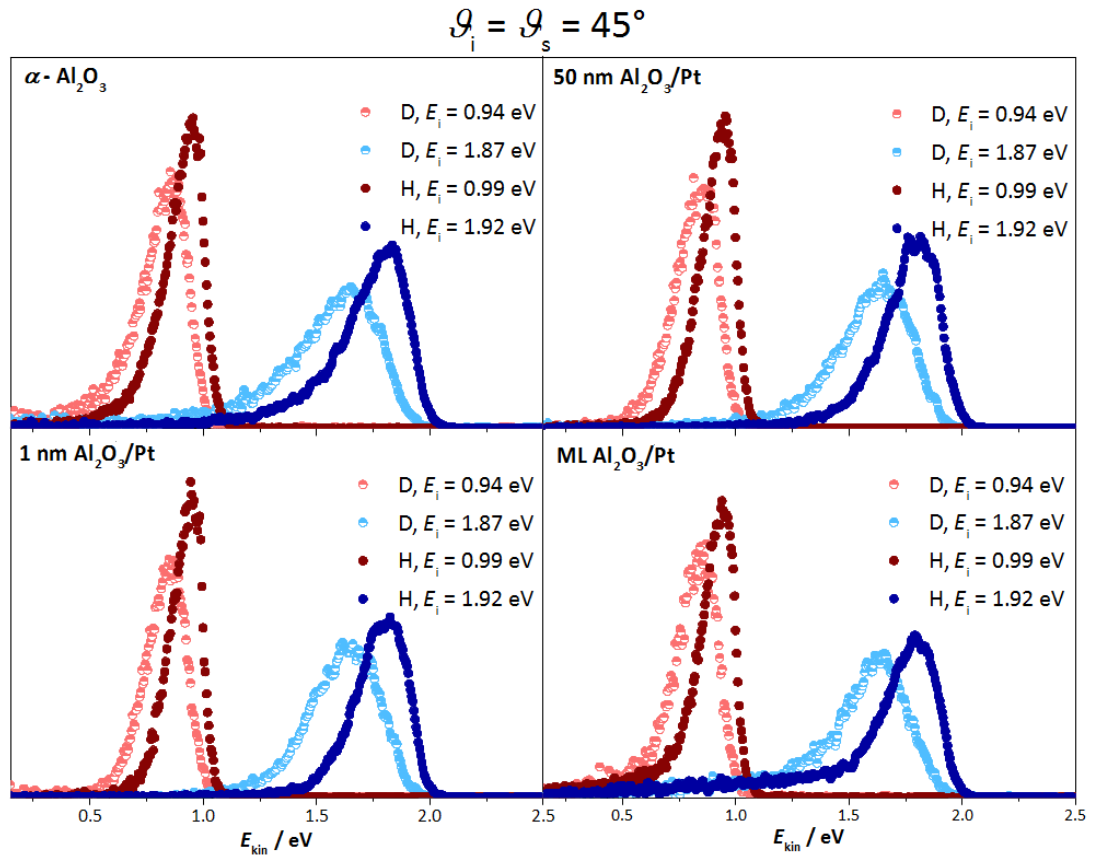


Figure 2.34: Energy loss spectrum of hydrogen (filled dots) and deuterium (half filled dots) atoms with about one (red) and two eV (blue) energy and incidence angle of 45° , scattering from I, II, III and IV.^[221]

values of 30 % discussed by PUURUNEN *et. al.*, 2005 and citations therein^[15] thus is in good agreement with found growth rates being higher, too. The absence of the platinum signal for the 5-cycle ALD sample III (green) showed complete surface coverage. This homogeneity was supplementary proven by both cross section high resolution (HR)TEM shown in figure 2.35 and SEM in figure 2.20 showing no agglomeration of Al_2O_3 .

Experiments of hydrogen scattering and *in situ* Auger analysis were performed by Y. DORENKAMP. In figure 2.34 the energy loss of deuterium and hydrogen atoms, scattering with incidence energies of 1 and 2 eV for the four samples is displayed. Comparing the data with the generally expected isolator-metal discrepancy (compare figure 1.17), it can be stated that all graphs show the main contribution of typical oxide scattering. Thereby it was proven, that the structure of the underlying material do not play a major role, comparing highly crystalline and amorphous Al_2O_3 in different thickness. The only difference was found in the ML- Al_2O_3 image. Here, the 2 eV graph showed platinum contribution. For better comparison this is overlaid in figure 2.38 with previous data of bulk [111]-platinum. It could be concluded, that the measured data for the ML- Al_2O_3 sum up of both platinum and oxygen scattering due to the 50 % surface coverage: we addressed this mixture effect to the heterogeneous surface on which small hydrogen atoms can either hit metal or oxide areas/atoms. However, it seems therefore, that a single monolayer of oxide material would sufficiently overlay the metallic scattering character.

As an other finding the angular distribution of scattered atoms differed, as shown in figure 2.37 and 2.36. Here, the broadening was found to be inverse to the roughness, taken as a first explanational approach. Therefore, another structural parameter may governs peak widths. Since the scattering energy loss is always effected by electron or phonon excitation in the material, we searched for mismatches, namely in stoichiometry and impurities and density. Experimental findings are listed in table 2.3. Measurements using EDX show slightly increased oxygen (0.52 eV), even after correcting the integrals by the amount of substrate- SiO_2 , visible at 1.75 eV.

This was verified using EELS at various position of the 1 nm sample, resulting in a similar value for the Al to O ratio (compare figure ??). This may finally lead to an explanation, why the scattering of insulator was found to be dominant: With an increase of oxygen, the scattering from this atoms may be more likely than from the metallic surface.

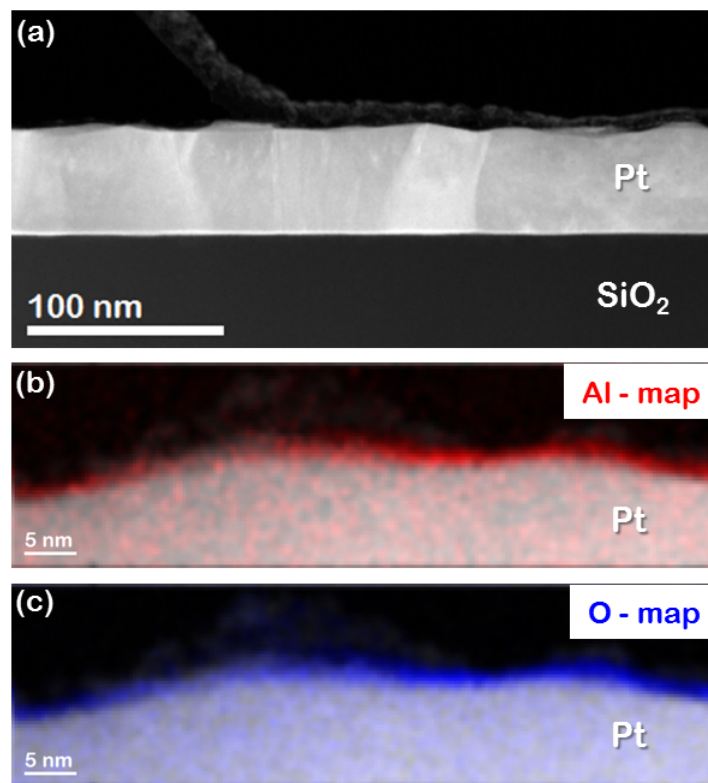


Figure 2.35: TEM image of a 55 nm Pt sample on SiO₂ (a) and EELS mapping of its surface region showing the thickness of five cycles deposited Al₂O₃ (b + c).

Carbon impurities were found to be slightly increased for the ALD-samples, but it cannot be excluded that this is merely the effect of dual transport contamination, once before the deposition experiment and later on deposited material. This would lead to increased EDX-signals by a factor of two and explain the missing C-signal in Auger measurements.

With the presented investigation of super-thin insulator layers on metallic substrate it could be proven, that scattering is evidently independent of roughness, stoichiom-

entry and thickness unless a few monolayers (3-5) are reached. It could be proven, that elastic or inelastic scattering is only based on the specific atom hit on the surface. A mixture of surface atoms, as presented in the unsaturated monolayer assay therefore lead to never before observed mixing of two different hydrogen collision behaviours, undergoing an energy loss or maintaining its speed.

Table 2.3: Assays and properties. Roughness measured with AFM (4.2.4), stoichiometry with EELS (4.2.2) and EDX (4.2.5). Carbon impurity with EDX, XPS (4.2.1) and Auger.

assay	Al to O ratio	Roughness	Carbon impurity
substrate SiO ₂	-	0.20 nm	1.38 %
1 ML Al ₂ O ₃ IV	n.d.	4.47 nm	n.d.
1 nm Al ₂ O ₃ III	Al ₂ O _{3.5±0.2}	1.82 nm	≈ 0 %
50 nm Al ₂ O ₃ II	Al ₂ O _{3.7±0.1}	0.661 nm	2.61 %
[0001] Al ₂ O ₃ I	Al ₂ O ₃	0.164 nm	1.19 %

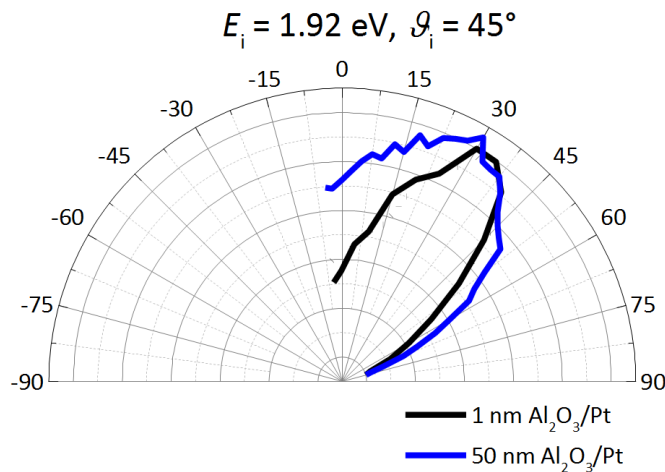


Figure 2.36: RAT experiment angular distribution of scattering hydrogen from bulk (blue) and thin Al₂O₃ (black) with about 2 eV energy and incidence angle of 45°. Both samples were deposited with ALD.^[221]

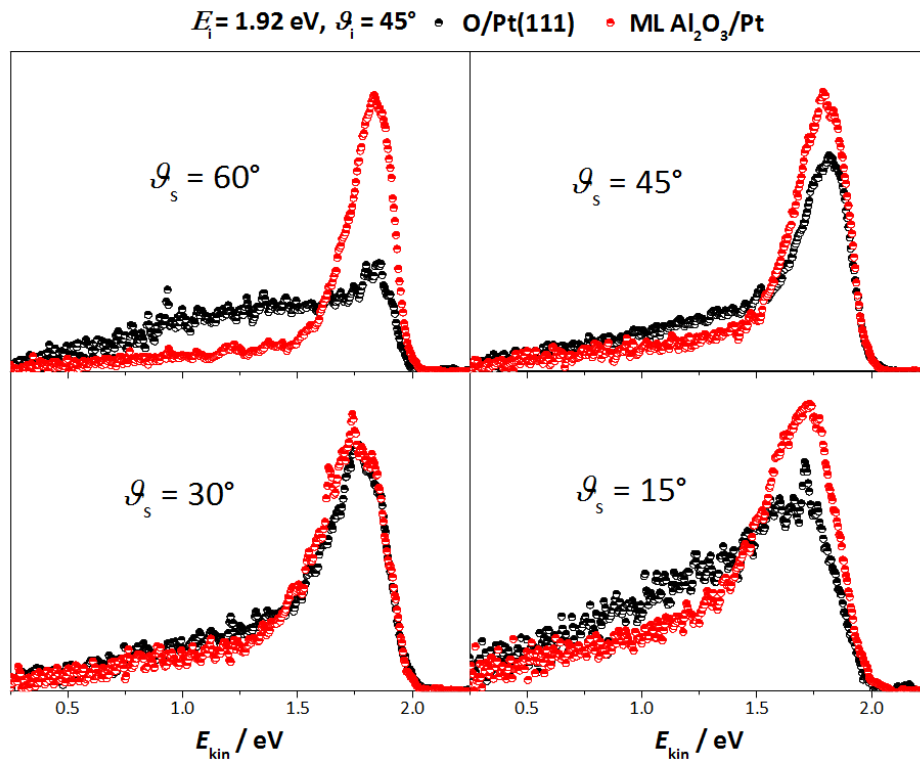


Figure 2.37: Hydrogen scattering with 2 eV from ML-fraction on Pt with different detector adjustment ϑ_s compared with bulk Pt.^[221]

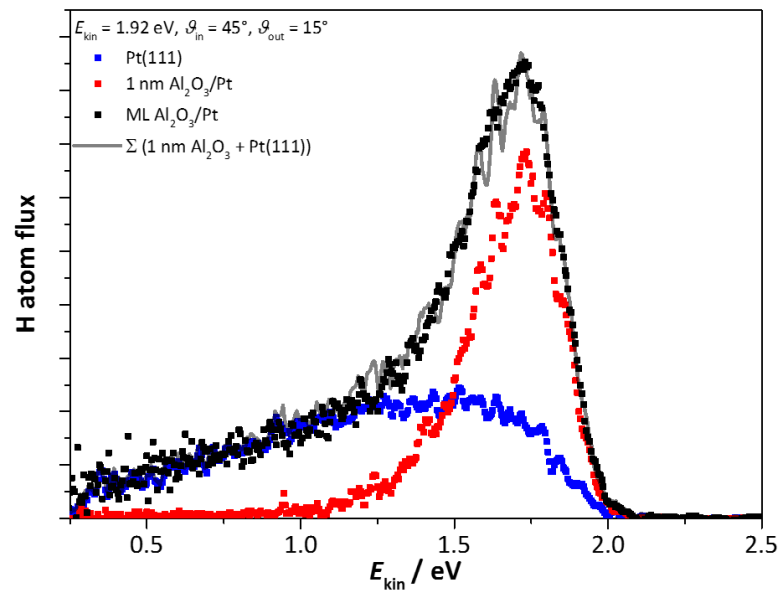


Figure 2.38: Energy loss spectrum of H-atoms of different energies impacting the surfaces of III, IV and Pt for comparison.^[221]

2.3.2 Silicon Oxide Deposition

Within the framework of cooperation of CRC 1073 and CRC 803 amorphous SiO_2 layers were deposited for the purpose of vesicle spreading. For this intent we used the literature known precursor **13** in figure 2.39 with water, tracking gas phase composition with MS shown in figure 2.40. The track of ethanol fragment displays the possibility of mechanical investigations during deposition: the smaller signal arises during the water pulse and originates from surface reaction



only, illustrating the possibilities of *in situ* MS nicely. This experiment show the remarkable possibilities of the chosen method. The evidence of faster vesicle spreading can be reviewed in J. SCHUMACHER's dissertation which is to be published.

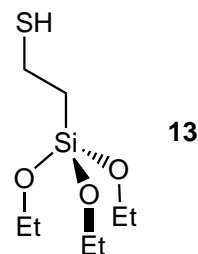


Figure 2.39: Structure of the applied silicon containing precursor $\text{Si}(\text{C}_2\text{H}_4\text{SH})(\text{OEt})_3$, (**13**) for SiO_2 deposition.

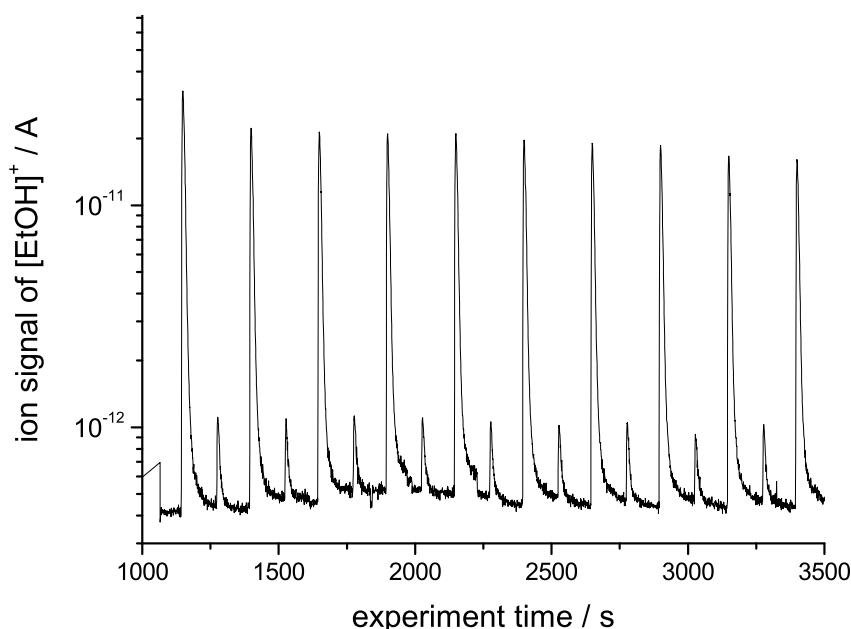


Figure 2.40: MS track of evolving $[\text{EtOH}]^+$ in the deposition experiment. Small signals arise reacting water with the covered surface, bigger peaks show the inlet pulse of **13**.

2.4 Precursor Development and Testing

2.4.1 Cobalt

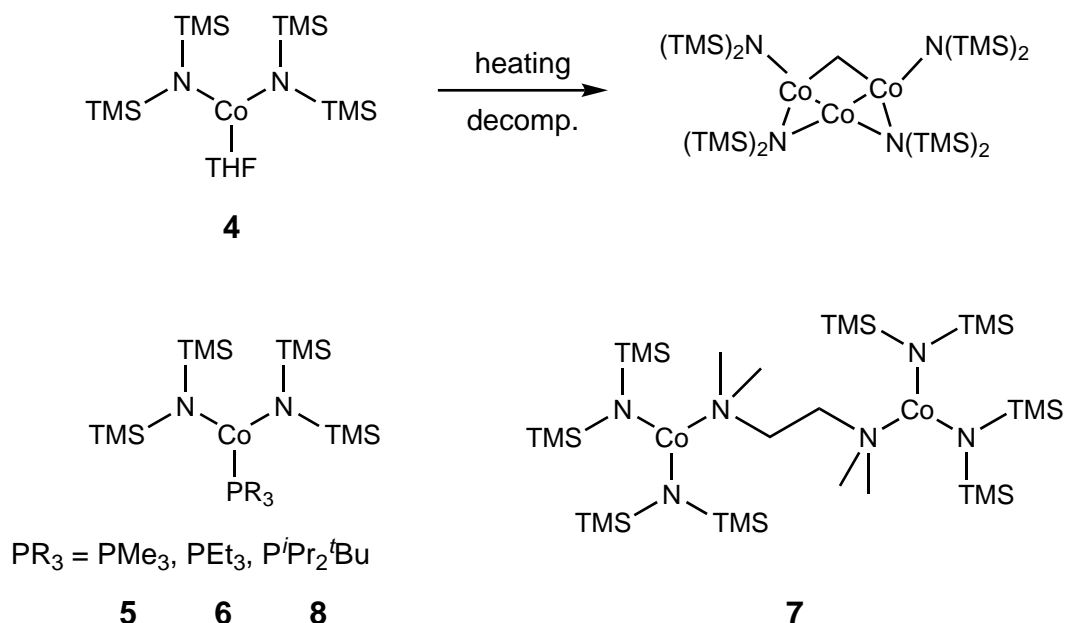


Figure 2.41: Employed Cobalt containing precursors for metallic Cobalt and CoO_x deposition.

As a joint project of precursor synthesis and deposition experiment within an industry cooperation founded by BASF, J. GERKENS synthesized several cobalt precursors displayed in figure 2.41. As described previously (1.1.4), all precursors feature the absence of α - or β -hydrogen atoms to enable the discussed reaction cycle in scheme 1.4.1. As part of a bachelor thesis^[222] volatility, stability, and ALD properties of these novel structures were investigated. Determination of stability parameters were performed in undermined screws, heated to different temperatures over night as shown in figure 2.42. We could show stability of this compound class up to 150 °C, although the pressure in the screw cavity raised to two bar over the corresponding ALD chamber



Figure 2.42: About 1 cm³ hollow screw setup for stability tests of Co containing precursor.

experiment, which hinders a precise comparison. Therefore, we applied line vacuum and 70 °C to a Schlenk tube over 24 h to a pestled **6** in a second experiment and found crystalline material at different positions in the tube afterwards, proving successful (re-)sublimation.

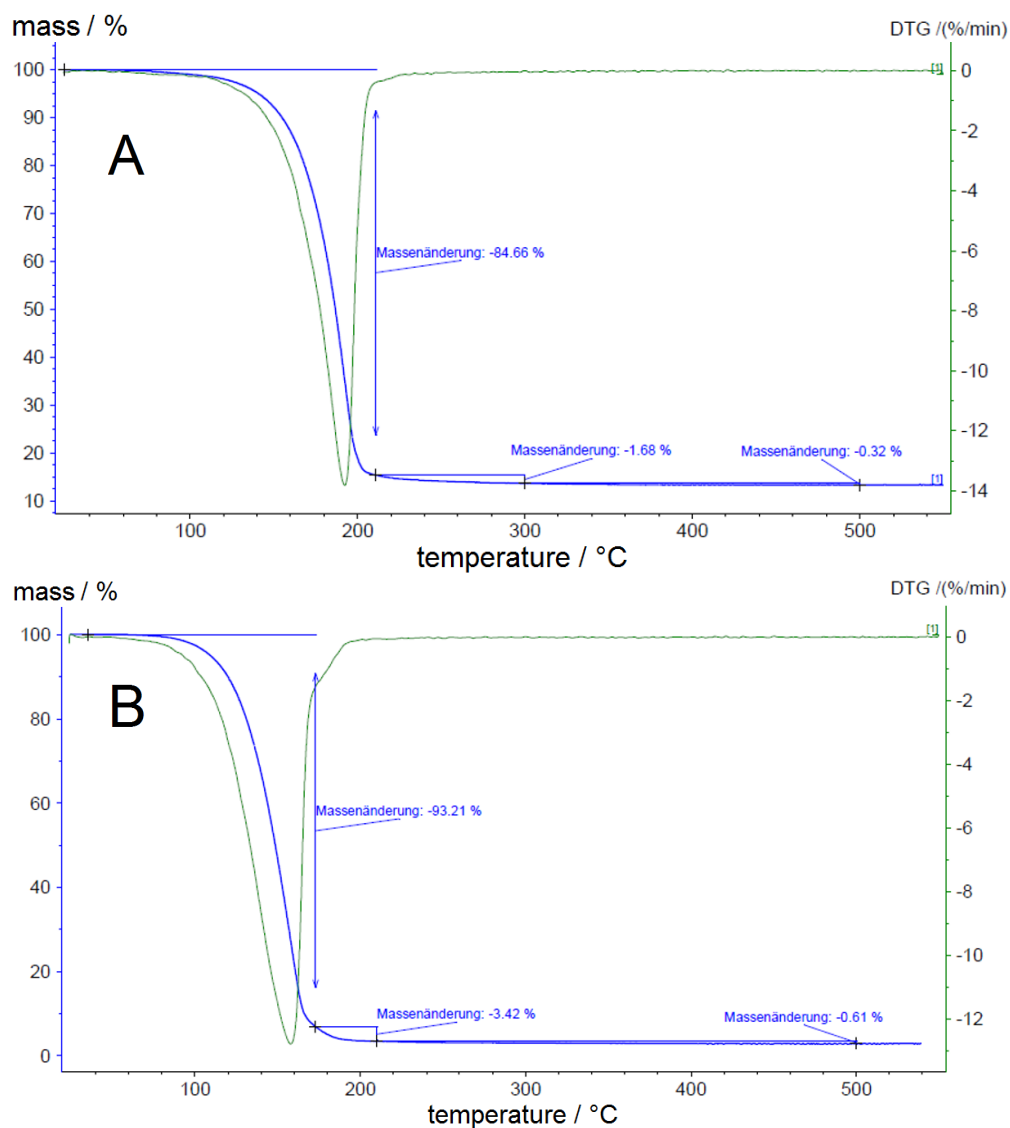


Figure 2.43: TGA of **6** (A) (observed similary for **6** and **8** (B) showing influence of symmetry break on the remaining mass (a drop from 14 % to about 2 % reminder) and the evaporation temperature, starting sublimation was observed ($\Delta T \approx 25$ K).

In contrast to this, ambient pressure TGA experiments at BASF mainly result in a remaining residue, whose mass was perfectly in agreement with the mass fraction

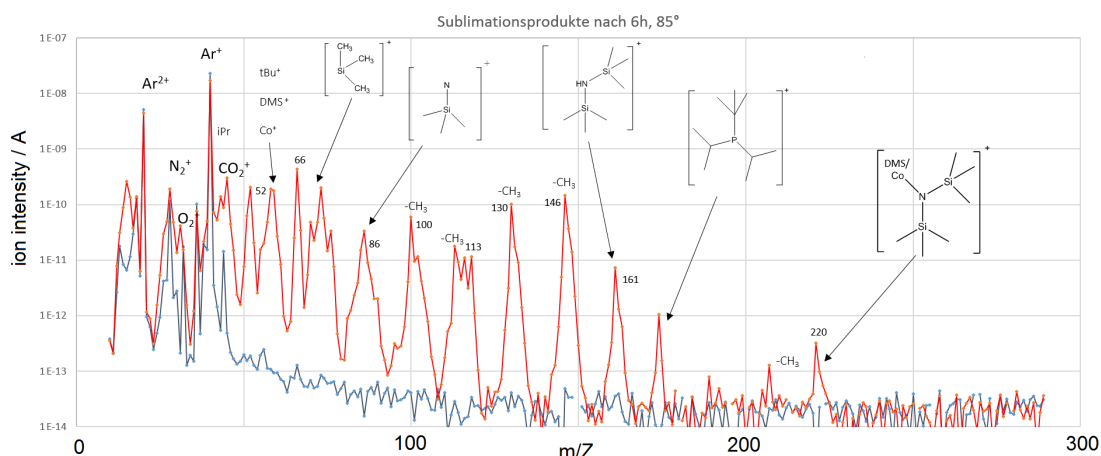


Figure 2.44: MS spectrum of $\text{Co}(\text{NTMS})_2(\text{P}^t\text{Bu}^i\text{Pr}_2)$ (**8**) sublimed at $85\text{ }^\circ\text{C}$ after 6 h of deposition.

of cobalt in the compound (**5**, **6** and **7**) indicating decomposition and ligand release.

Several compounds were tested in the chamber to elucidate sublimation behaviour in the ALD experimental set-up using MS. During manifold tests combining TGA and reactor results it turned out that the break of symmetry had a major influence on sublimation properties. Comparing signal intensities of e.g. $[\text{TMS}]^+$ in a MS experiment with alike chamber parameters (pulse time, flow rate, temperature, MS pressure, ...) enabled relation of sublimation temperature. Condensing a variety of experiments, **8** turned out to be stable in TGA experiments (figure 2.43) and had the lowest sublimation temperature in the precursor flask: while symmetrical compounds (**4,5,6**) fulfil acceptable concentrations in the range of 100 to $120\text{ }^\circ\text{C}$, the MS-signal of **8** is comparable in the range of 65 to $85\text{ }^\circ\text{C}$. This is displayed in figure 2.44, referring to the EI-fragmentation of the gas phase composition in the chamber during the pulse of **8** heated to $85\text{ }^\circ\text{C}$. High intensity of the $\text{N}(\text{TMS})_2$ -Ligand together with other fragments could be observed. Sadly the m/z overlay of $[\text{Co}]^+$ and $[\text{DMS}]^+$ made final interpretation in respect of Co concentration difficult. Nevertheless, two features were measured uniquely using **8**: The drop of signal observed by MS, corresponding to gas phase concentration, turned out to be negligible, as shown in figure 2.46. Even during deposition experiments, where the concentration of **5**, **6** and **7** dropped

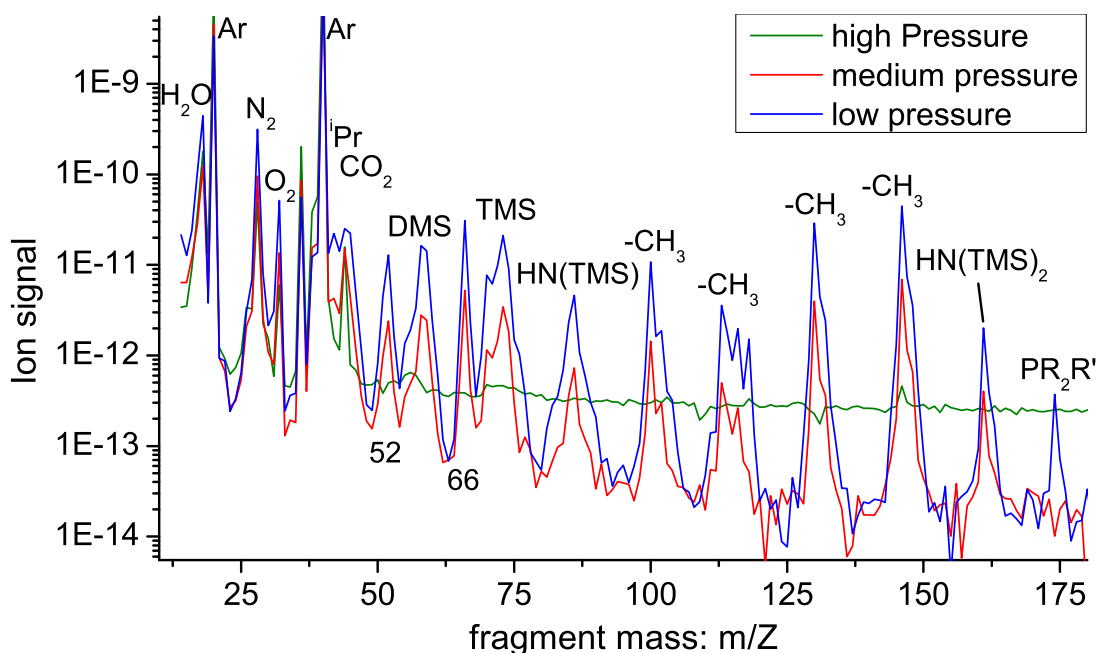


Figure 2.45: EI-MS spectra, taken at various pressures: 8 (green), 2 (red) and 0.5 mbar (blue), indicating a strong dependence of the sublimation or decomposition of $\text{Co}(\text{NTMS}_2)_2(\text{P}^t\text{Bu}^i\text{Pr}_2)$ (**8**) on the pressure. Sum formulas drawn in the spectrum are all ways meant as $[\text{X}]^{n+}$, where X is the fragment and $n = 1$ or 2 . $\text{PR}_2\text{R}' = \text{P}^t\text{Bu}^i\text{Pr}_2$.

by 90 % in the second pulse compared to the very first one, **8** mass fragments were detectable in time-invariant constant intensity. Secondly, phosphine signal was observed for the first time, and was furthermore strongly dependent on the chamber pressure, as depicted in figure 2.45. In figure 2.46 fragments of **8** are visible in the water pulse, originating from surface reactions. With time = 190 s, fragments with the mass $m/Z = 92$ ($[\text{SiO}_4]^+$ or $[\text{O}=\text{P}^t\text{Bu}^i\text{Pr}_2]^{2+}$) and 134 ($[\text{H}_2\text{SiNMe}_2\text{NMe}_3]^+$ or $[\text{H}_2\text{SiOH}(\text{NMe}_2)_2]^+$ or $[\text{O}=\text{P}^i\text{Pr}_2]^+$) showed high concentrations, to prove a reaction between **8** and the oxidizing precursor has taken place on the substrate, since otherwise the signal would be constant and not exclusively rising during valve opening. However, they are also observed during the pulse of **8**, so this may also point to the evidence of precursor decomposition before sublimation and reaction with the oxygen background, since this presumably the best explanatory approach explaining two ligand showing different evaporation properties and oxidized fragments are observed, respectively.

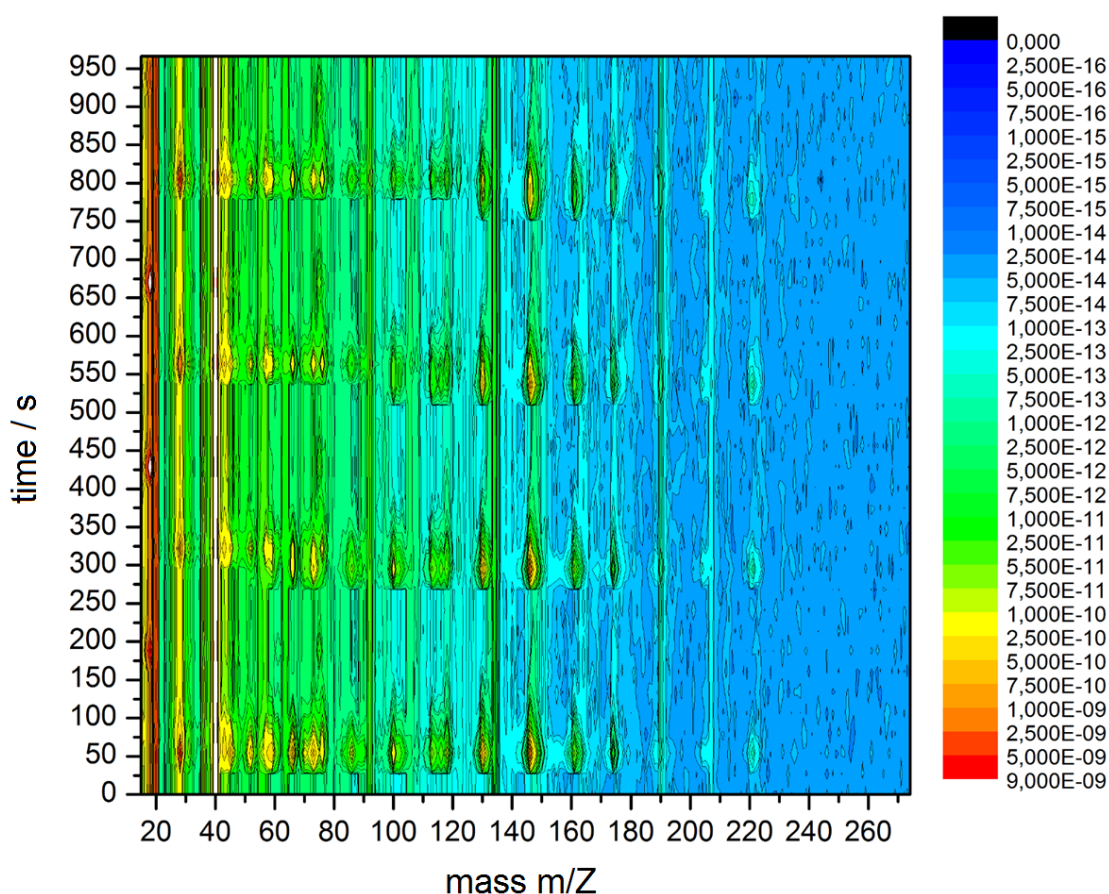


Figure 2.46: 3D mass spectrum tracking the deposition of **8** with H₂O (m/Z = 18) using a bubbler. Corresponding fragments to the signals are drawn in figure 2.45.

With the prove of ligand oxidation during the H₂O pulse, first deposition were performed, using H₂, H₂O, O₂ and Air, aiming for metallic cobalt first with H₂ and, after unsatisfying results, the focus was relocated to the easier cobalt-oxide model system (with coprecursor H₂O and O₂). Anyway, CoO-deposition remained dissatisfying in amount/thickness and growth speed as shown in figure 2.47: although the pulse-microstructure is visible with QCM, no significant thickness increase was measured. Even after these thousand ALD cycles CoO amount was hardly detectable on the substrate by colour change and barely measurable on the SiO₂/Si-substrate using XPS (figure 2.47 B). Also minor ligand residues were detected indicating no pure deposition. Following Nuclear magnetic resonance (NMR) spectroscopic investigations of the residues in precursor steel containers proved partial decomposition

taking place, as presented in figure 2.49 and 2.50, where several paramagnetic species were forming which could not be interpreted with respect to their structure. However, the decomposition of compound **8** is much slower, as presented in the NMR spectrum in figure 2.51. Here, only smaller side product signals raised over the ALD experiment proving **8** to be the most stable compound tested. Further structural investigations, using single crystal XRD only revealed the structure shown in figure 2.41.

To investigate and avoid decomposition of the material prior to reaching the substrate various attempts were made, such as pestling substances (resulting in the chance of lower sublimation temperature), pre-evaporation and resublimation to the ALD valve vestibule to shorten the travelling distance to the sample holder. Furthermore, increasing purge flow speed, changing the chamber pressure, or using a bubbler precursor reservoir were tested as approaches. None could increase gpc-rates significantly. To illuminate the pathway of decomposition, MS-investigations were performed, comparing possible decomposition products with the pattern in figure 2.44 (for an overlay, see figure 2.48). As already mentioned, $[\text{DMS}]^+$ and $[\text{Co}]^+$ -fragment are similar in mass. The isotope purity of ^{59}Co further impedes differentiation. Chances therefore are that TMS_3 as a side reaction product plays a major role in the decomposition pathway since overlaid MS-data showing identical masses and very similar signal shape (broadening, intensity, ...). Nevertheless, no oxygen containing fragment could be detected in MS-studies refuting O_2 -background of about 300 ppm influences deposition experiments. Applied elemental analysis (EA) (table 2.4) indicates an increase of the Co-fraction in the precursor compared to the pure compound (variation of pure compound and expected values is a result of EA-preparation in air), thus indicating decomposition supportingly. The low vapour pressure of forming oxide species, especially in the case of the phosphine signal, may explain their absence. Furthermore, the ionisation yield in the MS experiment may be limiting for the phosphine signal.

Table 2.4: Elemental analysis before (B) and after (A) the ALD-experiment with **8** (4500 applied cycles of 15 s of **8** at 85 °C).

assay	% P	% Co
Probe A (ALD)	2,60 (1)	13,45 (1)
Probe B (pure)	5,22	11,41
expected	5,61	10,68

The origin of the experiment's failure could not be proven conclusively. It could be shown that decomposition already takes place in heated steel precursor containers but not in a glass-based sublimation apparatus. Breaking of symmetry and sterical demand of ligand in **8** could improve stability to deposit monolayer fractions of Co with very small gpc-rates ($0.01 \pm 0.001 \text{ \AA} \cdot \text{cycle}^{-1}$) and poor impurity content. A possible decomposition pathway was identified by MS being TMS-group transfer based.

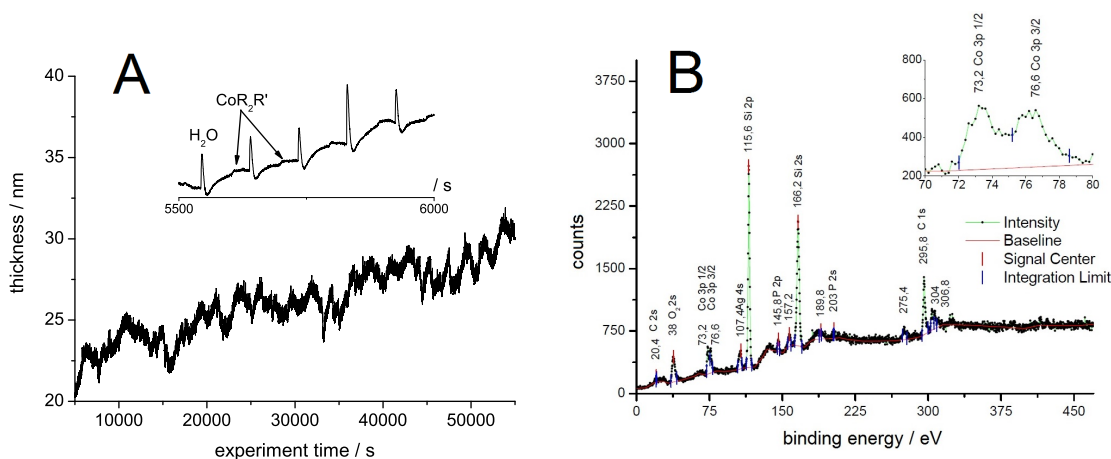


Figure 2.47: **A:** QCM track of a Co deposition experiment with $\text{Co}(\text{NTMS}_2)_2\text{PET}_3$ ($\text{PR}_2\text{R}'$) and Water with 1000 cycles indicating very low deposition progress. The superimposed image show five cycles. Strong signals arise of the interaction with water, reducing the amount on the surface and small signals correspond to precursor **8** increasing the thickness sustainably. **B:** XPS spectrum of the experiment showing Co ($3,7 \pm 0,7 \%$) on the surface as well as P ($0,8 \pm 0,3 \%$) and C ($9,8 \pm 1,1 \%$).

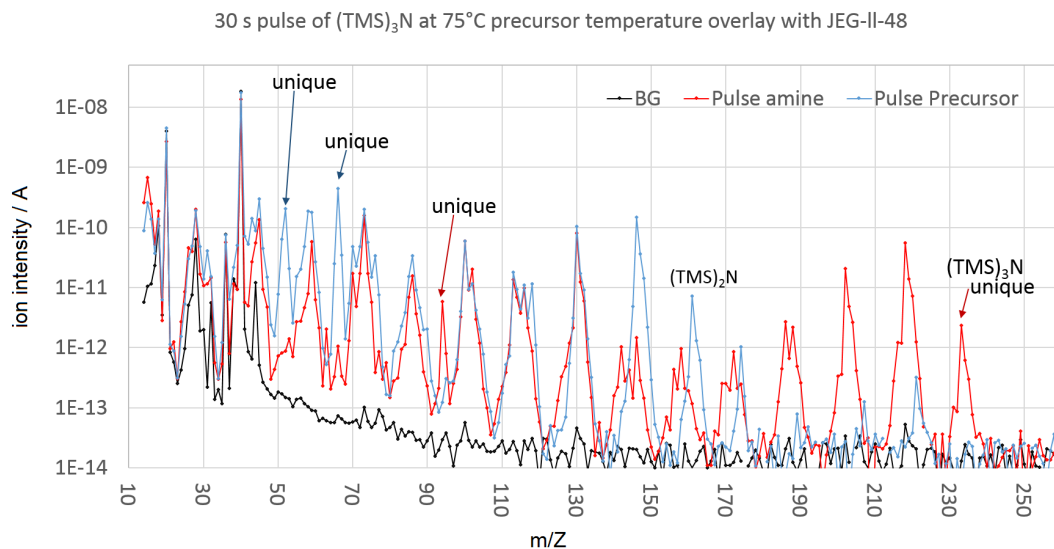


Figure 2.48: MS spectrum of $\text{Co}(\text{NTMS}_2)_2(\text{P}^t\text{Bu}^i\text{Pr})$ with 85 °C after 6h of deposition overlaid by a spectrum of similar pulsed NTMS_3 .

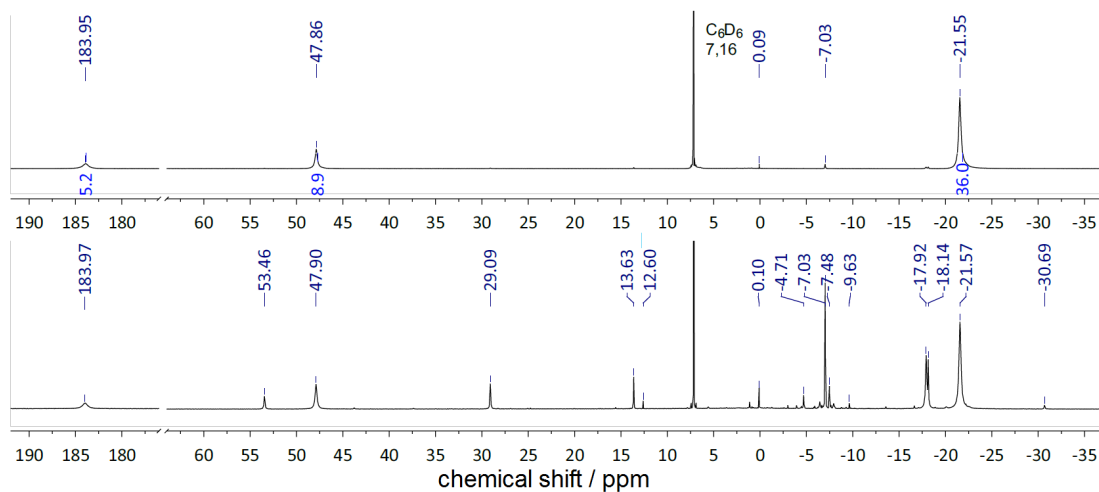


Figure 2.49: NMR spectrum of $\text{Co}(\text{NTMS}_2)_2\text{PET}_3$ residue after several hundred deposition cycles with an evaporation temperature of 95 °C showing new compounds forming due to decomposition.

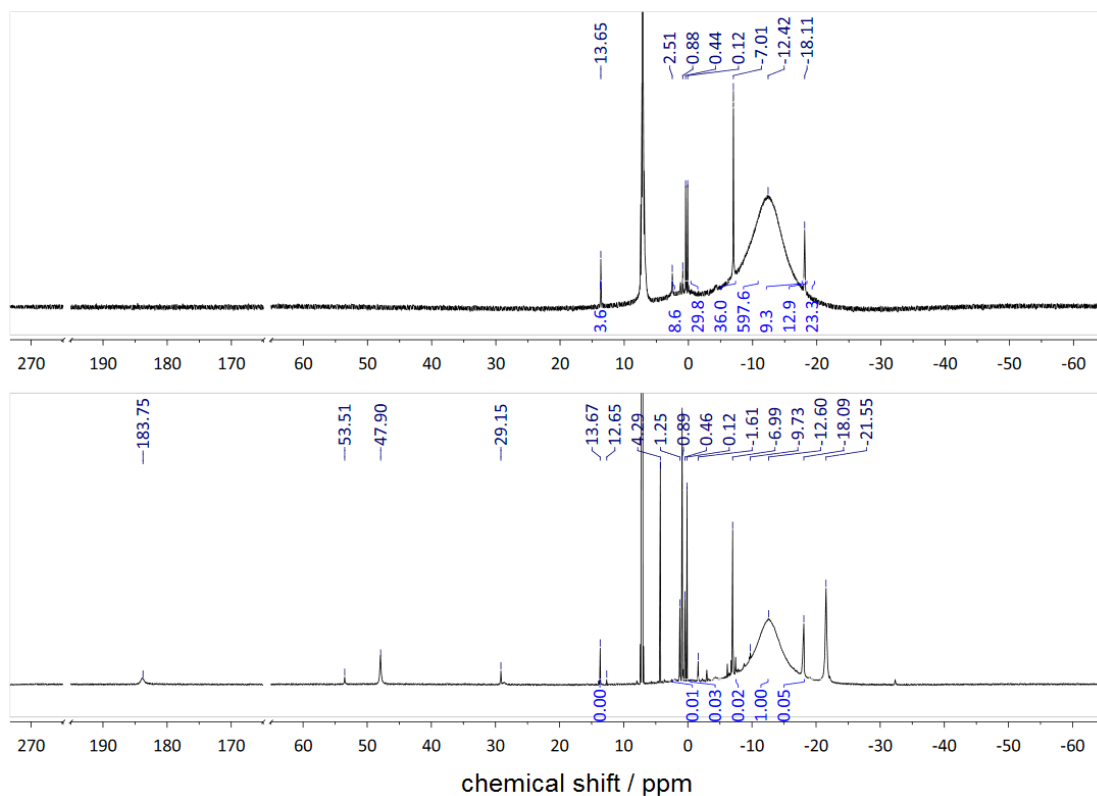


Figure 2.50: NMR spectra of Co(NTMS₂)₂(TMEDA) as synthesized compound and after a few hundred deposition cycles with the reservoir kept at 70 °C.

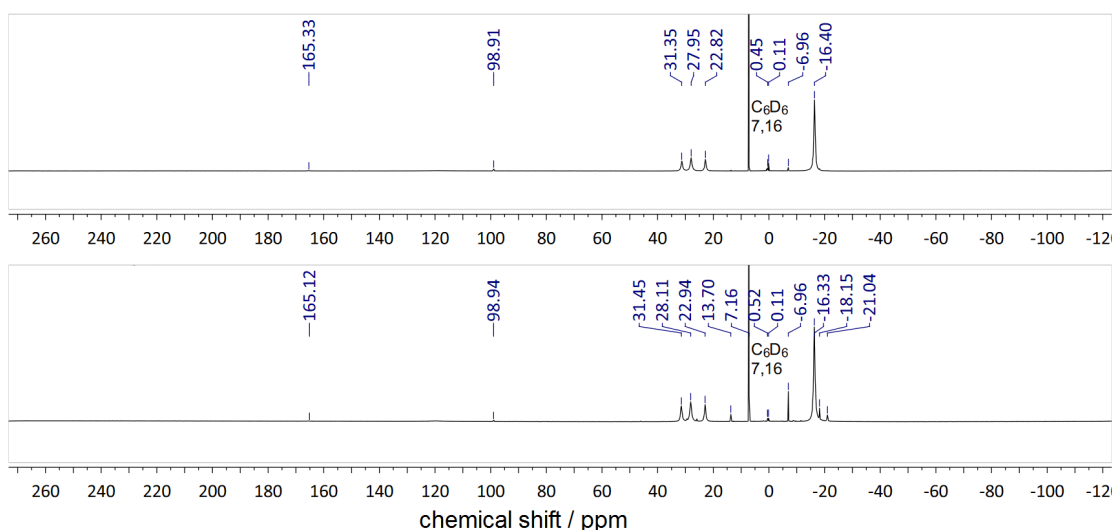


Figure 2.51: NMR spectra of Co(NTMS₂)₂((P^tBuⁱPr)) as synthesized compound and after a few hundred deposition cycles with the reservoir kept at 70 °C.

2.4.2 Tantalum Sulphide

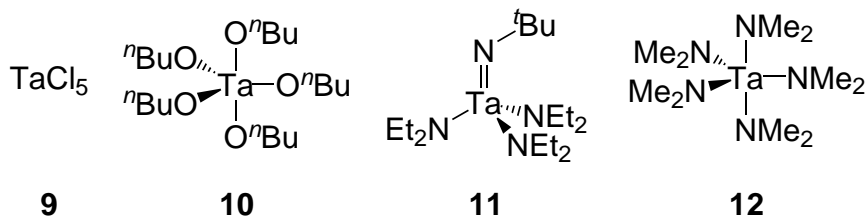


Figure 2.52: Employed Tantalum containing precursors for TaS_x deposition.

Three different precursors were applied in this project, Pentachlorotantalum (**9**), (*tert*-butylimino)tris(diethylamino)tantalum (**11**), pentakis(dimethylamino)tantalum (**12**) and penta-*n*-butoxytantalum (**10**), depicted in figure 2.52. In addition to the depicted data, a more detailed summary of this project can be reviewed in the Bachelor theses of T. MÜNCH.^[223]

Setting up first deposition experiments, **11** and **12** and **10** were reacted with H₂S in tetrahydrofuran (THF) while **11** and **12** were found to immediately form a brown precipitate at room temperature. In contrast to this, **10** did not react, proving Ta to be merely oxophilic and **10** was discarded. Attaching the precursors to the chamber, first experiments aimed for the investigation of the evaporation properties of compound **9**, **11** and **12** and were performed using the normal reactor geometry. For this purpose, the MS was attached and the corresponding mass was tracked using small inlet pulses of the compound during a constant temperature increase of the reservoir. In our setup, **9** turned out to be vaporizable above 110 °C, **12** at about 85 °C and **11** exceeding 65 °C. The discrepancy between **12** and **11** can be explained by the reduced mass and, more importantly, by the break of symmetry. For first depositions using ^tBuSH the evaporation temperature was kept 15 °C over the investigated minimal evaporation temperature. Experiments with **11** were performed holding the lowest evaporation temperature and therefore allowed for the most broadened ALD window, did not result in film formation, although experiments at various substrate temperature, ranging from 66 to 300 °C were performed. We assigned this finding

to the higher stability and poor chemisorption on the substrate and relocated our focus towards **12**, since **9** was discarded because of its high evaporation temperature and the drawback of possible HCl evolution during deposition, damaging chamber, pump and MS. With **12** we were able to generate TaO_x films, using water as a co-precursor, following TOLBERTS procedure.^[196] Films formed both at the special position (compare in the experimental section, figure 5.1) and on the wafer, although film thickness on the special position was found to be slightly larger. Nevertheless, optimization of the procedure allowed us to broaden the published ALD window to significant lower temperatures. Deposition described by TOLBERT and coworkers necessitate temperatures above 250-300 °C.^[196] A substrate temperature of 130 °C and a special position temperature of 110 °C resulted in a TaO_x films, lower temperatures were not examined extensively. The roughness of these low temperature deposited materials was outstandingly small with R_a = 0.35 for very thin films, proving “Franck-van-der-Merwe-growth”^[31,32,33] to be the dominating mechanism.

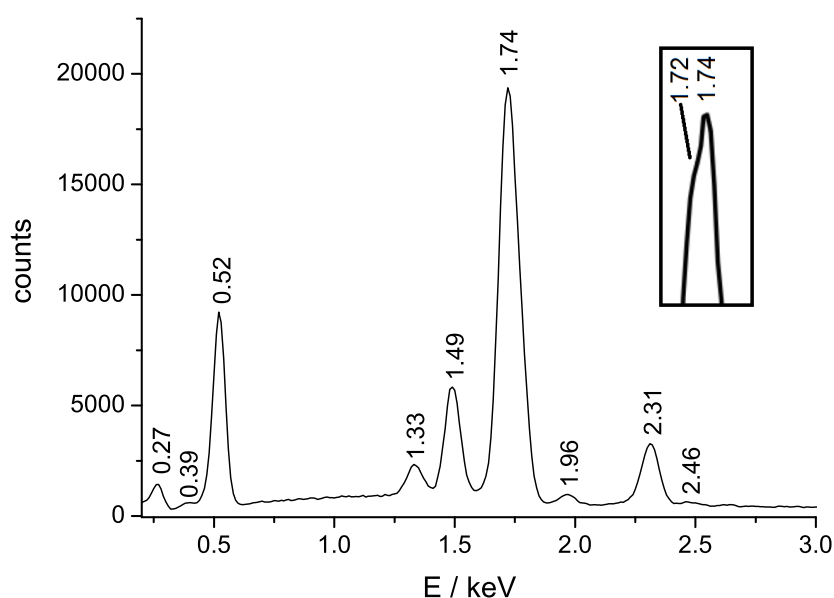


Figure 2.53: EDX spectrum of a TaS_x film on Al₂O₃/SiO₂/Si substrate. The indicated signal energies correspond to C (0.27 keV), N (0.39 keV), O (0.52 keV), Ta (1.33 keV), Al (1.49 keV), Ta and Si (1.72 keV and 1.74 keV), S (1.96 keV), S (2.31 keV), S (2.46 keV). The overlay of the Ta and Si signal is highlighted.

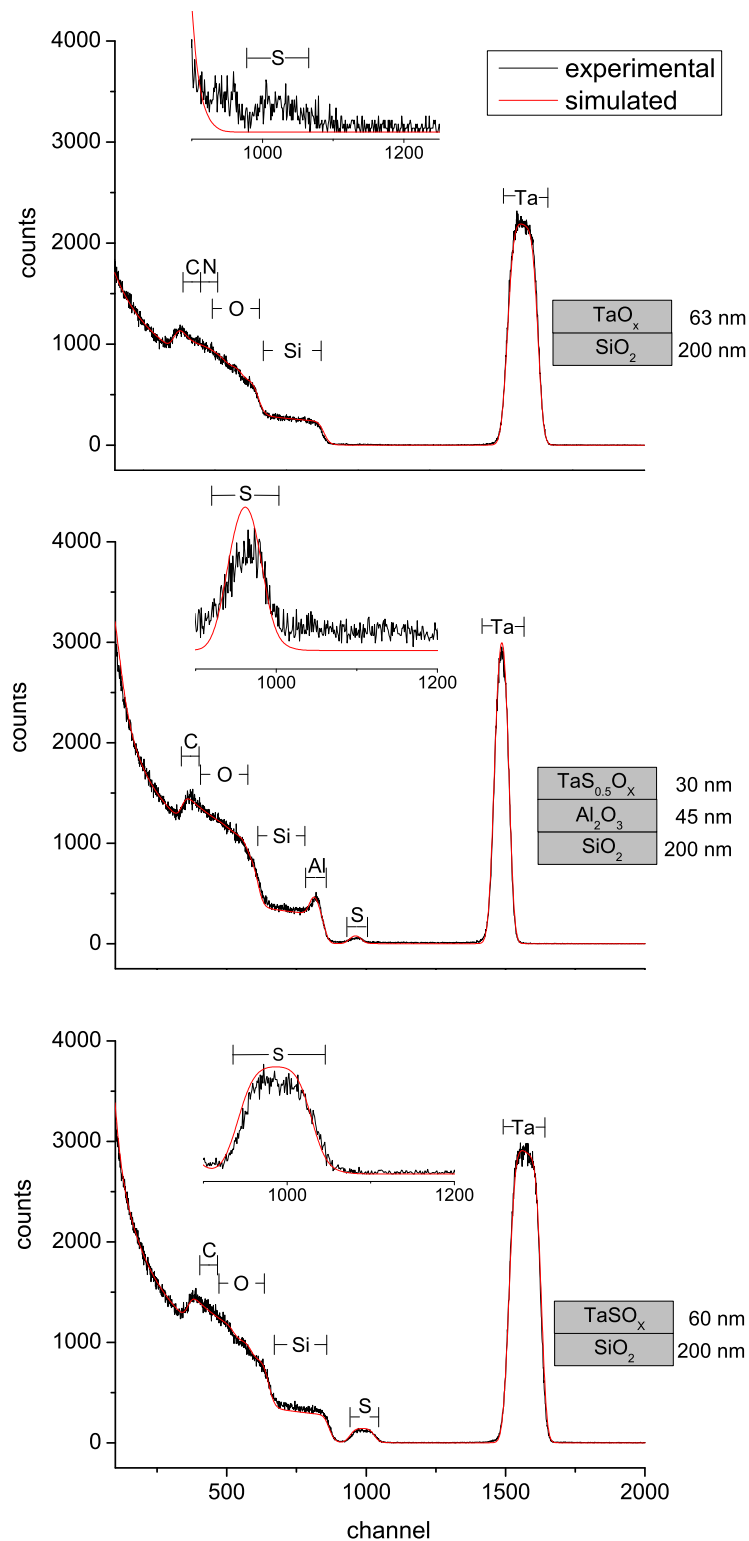


Figure 2.54: HRRBS spectra of three layers, generated with different deposition parameters (black) with the corresponding fit (red), leading to layer composition (right hand side). **A:** special position wafer with 110 °C substance temperature. **B:** connected bubbler with 90 °C and Al₂O₃ seed layer. **C:** sublimation out of the bubbler with 110 °C. Substrate temperature was 130 °C in all cases. A detailed explanation of the method is given in chapter 4.

The growth rate was approximated, corresponding to profilometry data to about $0.6 \pm 0.2 \text{ \AA} \cdot \text{cycle}^{-1}$. Generating films with **12** and H_2S also resulted in deposition at the special position, although these films were much thinner and also mainly composed of tantalum and oxygen, instead of sulphur as intended. This was verified by Rutherford backscattering spectroscopy (RBS). In figure 2.54 (top spectrum) the fit was not able to include sulphur share in the film, though there is a signal significantly different from noise depicted in the highlighted area, to prove a sulphur source was applied, albeit not contributing appreciable to the film.

Furthermore, this deposition was not reproducible in constant film thickness, and therefore a bubbler was attached to increase the amount of **12** and the author was able to generate films on the special position and the normal sample holder, respectively. Film thicknesses on both positions, albeit separated by $> 15 \text{ cm}$, were measured to be of similar size, according to profilometry data. Furthermore, the special position substrate and wafer on the sample holder were deposited with the same amount of material from both top and underside, proving ALD to be the dominating mechanism.

Sulphur (2.31 keV) content was assured, according to the EDX spectrum in figure 2.53 showing no nitrogen (0.39 keV) and only small carbon (0.27 keV) impurity. However, the oxygen contamination was still very high, which was extracted from applied HRRBS experiments to verify the stoichiometry parameters. In figure 2.54 the middle and bottom graphs reflect tantalum containing layers generated using a bubbler. In both experiments the investigated layers result of 600 deposition cycles, only the amount of **12** was changed by an increase of the reservoir temperature by 15 K. In the two films the oxygen content was fitted with 60 and 40 %, respectively. In a control experiment, where only **12** was pulsed onto the substrate while preserving all other deposition parameters, no films could be observed. The origin of the oxygen in the film was therefore assigned to be contaminated H_2S , and later experiments verified a O_2 concentration of 1-5 % according to MS data. It was furthermore observed, that the ratio of tantalum to sulphur drastically changed with the

amount of **12**: already with 15 K higher temperature increase of the reservoir, the author was able to achieve an equal tantalum to sulphur content, which is more than a doubling of S, even though oxygen was still dominating. The critical shortage of compound **12** at lower temperatures here leads to an unsaturated surface, which afterwards reacts in a concurrent way with either O_2 or H_2S . Since the reaction with oxygen is expected to be thermodynamically favoured, films were anticipated to form oxides first. This is additionally proven by the investigation of layer thickness, which was found to be doubled in the case of higher bubbler temperatures indicating a fragmentary surface saturation (Which is best described by a ALD mechanism).

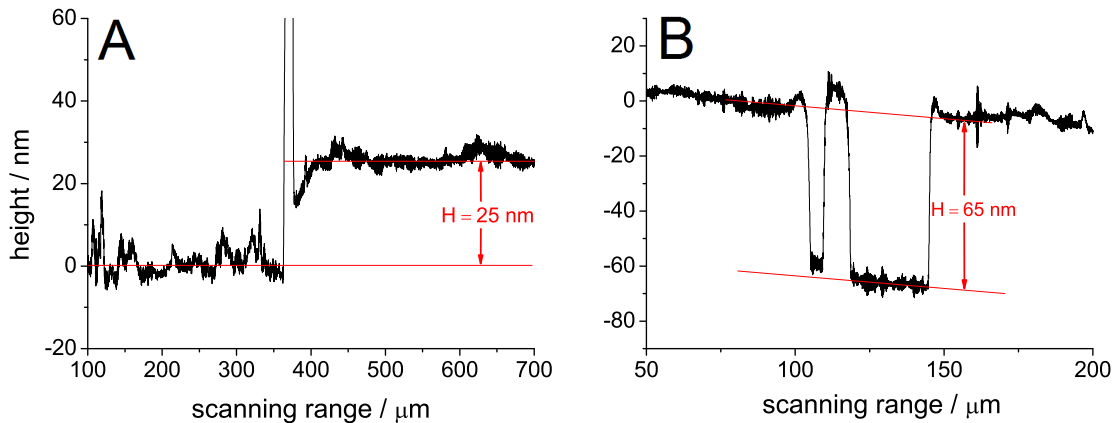


Figure 2.55: Profilometry spectra of 900 ALD cycles of TaS on 130 °C SiO_2 substrate **A** shows the height difference directly behind the capton tape proven by the signal at 375 μm being capton glue. **B**: shows the height profile of two holes, resulting from detaching film areas.

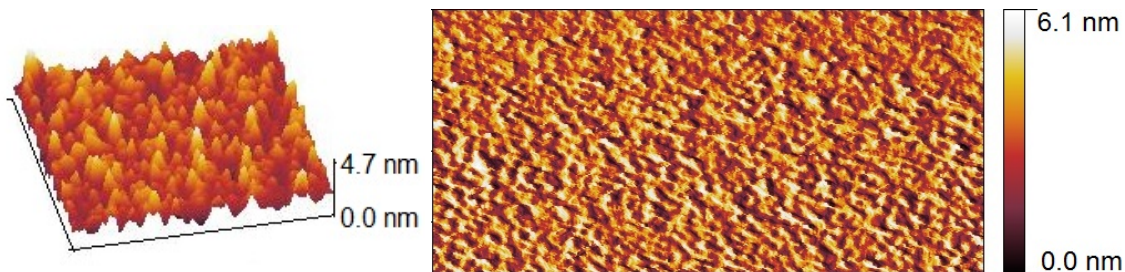


Figure 2.56: Atomic force microscopy analysis of a 30 nm TaS_xO_x film showing a height profile and large and small scale maximum roughness. The retral image show a top view on a $2 \cdot 2 \mu m^2$ sector showing no few dust particles contamination. The left image shows the roughness of the deposited material in a 3-D view of a smaller, $0.2 \cdot 0.2 \mu m^2$ area.

Moreover, the deposition was hardly homogeneous over large wafer areas if utilizing a copton tape as a flow barrier, indicated by profilometry measurements, depicted in figure 2.55 (low reservoir temperature of 90 °C). Film thickness was found to be far lower near the tape, but raised to a constant level within several hundreds of μm .

Although indicating saturation being inchoate, again CVD contribution becomes more unlikely, since the opposite would be expected in this case. Nevertheless, films were found to be homogeneous both in Ta and S stoichiometry, with respect to the depth profile, as depicted in highlighted areas of figure 2.54.

Film roughness was again outstandingly low according to AFM investigations and calculated to $R_a=0.45$ nm on SiO_2 with an additionally minor maximum roughness of about 5 nm, as depicted in figure 2.56 on the left side. Using a seed layer of Al_2O_3 , the average roughness was found to be equal, evidently independent on the roughness of the substrate. Here it calculated to $R_a=0.42$ nm. This is comparable to the well established Al_2O_3 procedure. Superior to the previous findings, also no larger hills could be detect in various measurements, as depicted in figure 2.56 on the right hand side. This can be asserted only by “Frank-van-der-Merwe”-growth conditions^[31,32,33] which is again a lead for ALD. However, the final prove can only be given by the independency of growth rate on the amount of the tantalum source

12.

Precursor stability was verified by EA investigations shown in table 2.5. Here the values almost fit the calculated and expected atom contribution. Two measurements were performed,

whereby it was conspicuous that values of the second measurement decreased by another percent for each element. The low values was assigned to originate from the

Table 2.5: Elemental analysis of the precursor bottle (bubbler) reminders.

assay	% C	% H	% C
deposition	27.2 ± 1.2	6.8 ± 0.4	15.6 ± 0.8
calculated	29.9	7.5	17.5

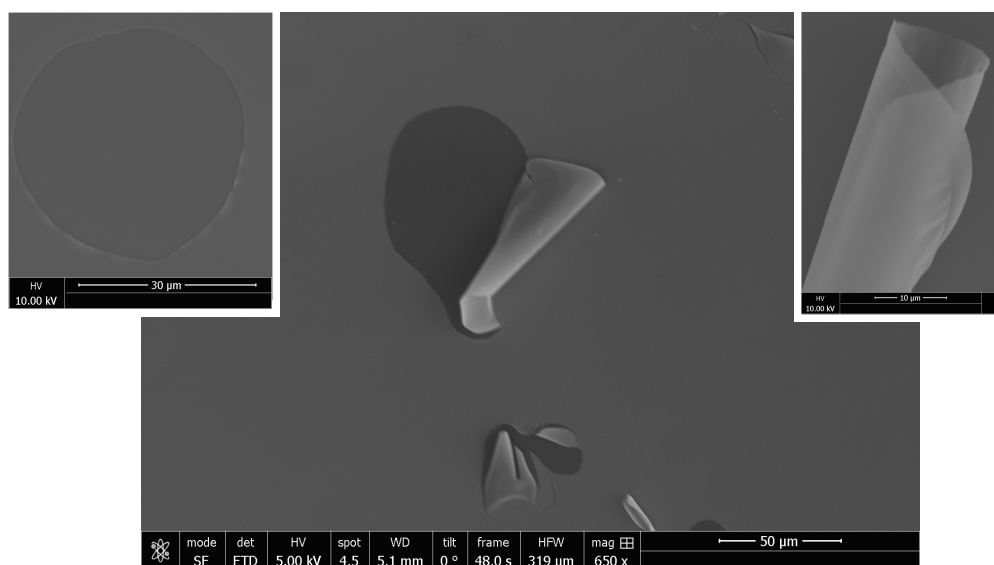


Figure 2.57: SEM image of 900 cycles of **12** and H₂S sequentially pulsed to a 130 °C SiO₂ surface. The centred image shows films prepared in the third and the small overlays in the first position of the sample holder. The small images show a completely detached and furred layer. The hole on the left and the layer on the right side were separated by several hundreds of μm.

EA experimental setup. The hypothesis was proven by NMR investigations, showing > 90 % of the precursor was compound **12** after several hundreds of deposition cycles.

However, the films already showed characteristic and expected properties. In figure 2.57, typical exfoliation (as described for TMDs earlier in this text) could be observed with an increase of the films thickness to 60 nm or above. In the left superposition image in figure 2.57 the hole is displayed, resulting from the completely detached layer, which was found furred on the surface close to the hole and depicted in the image on the right hand side. The centred image shows beginning exfoliation of different sizes of the layer. Still, areas observed ranged in sizes of several μm and can therefore be addressed to be quite homogeneous in diameter. It was proven, that film detaching affects the whole deposited material, using EDX and profilometry. The depth of holes can be reviewed in figure 2.55, where in the right spectrum two holes were screened. In these measurements, the films thickness and hole depth were measured to be the same. Furthermore, EDX investigations on the hole

areas could not identify any tantalum or sulphur content. Changing the substrate to a prior to this experiment deposited seed layer of 30 nm Al_2O_3 did not increase the binding strength to the substrate or reduce exfoliation.

With pentakis(dimethylamino)tantalum (**12**) films could be generated with outstanding roughness, typical TMDs behaviour, and an equal tantalum to sulphur content. The precursor could be proven to be stable in deposition experiments and its concentration could be sufficiently improved by a bubbler precursor reservoir. The origin of film contaminating oxygen could be identified and should be easily reducible, using a pure sulphur source.

3 Summary

With the presented novel laminar flow reactor design the deposition of three different materials could be reproduced. With Al_2O_3 we could prove that there is no CVD contribution to the found ALD mechanism, since the film thickness was perfectly independent of the amount of TMA and linearly dependent of the number of cycles. With the successful deposition of iridium it was possible to show that even the highest evaporation temperatures connote no obstacles. Furthermore, MS investigations illuminated reactions and gave mechanistic insights on the surface by gas phase analytics. Thin films of platinum were investigated in terms of noble metal initial phase behavior and turned out to be a perfect candidate for interlayered tailored materials. With thoroughly sampled parameters it was possible to improve the described film's literature properties ever so slightly in respect of growth rates, found to be increased in the platinum and the Al_2O_3 case and roughness, which was lower in almost every material tested. Most importantly, carbon impurities could be reduced as well as the oxygen content in metallic iridium and platinum layers. This is attributed to the low oxygen background in the chamber and the flight path of a precursor in relation to the substrate.

Two of these compound were combined to form nanolaminate materials. With this it was possible to synthesize the first ALD based combination of Al_2O_3 and platinum as super-lattices and materials with different or increasing interlayer thicknesses. Furthermore, it is one of the first ALD nanolaminate composites of alternating isolator and metal contribution. These materials were investigated with respect to their energy dissipation by photon energy intake using TTR as a common technique and

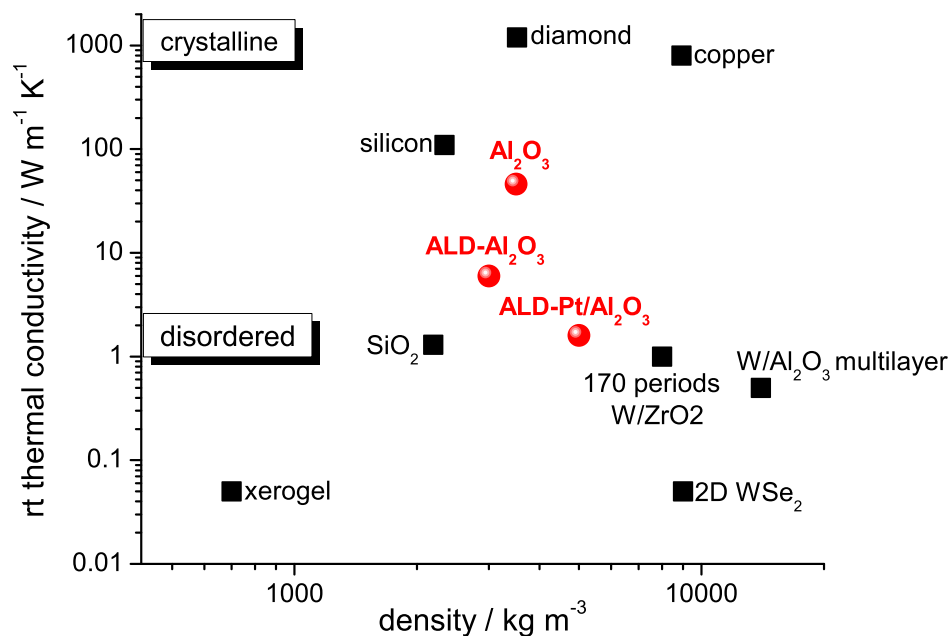


Figure 3.1: Room temperature heat capacities of samples synthesized in this thesis (red), compared with representative literature values (black).^[224]

very strong differences between single crystalline and ALD deposited oxides were found. The influence of interlayers, although being metallic and highly conductive was outstandingly large. With two interlayers we were able to reduce the heat capacity by a factor of 4, whereas single interlayers in other materials did not show a appreciable change in this property. The calculated data is compared with representative literature values of compounds and multilayers in figure 3.1. The conductivity of sample ALD 2 almost equals the conductivity of 170 periods of W/ZrO₂.^[165]

Two samples of atomically thin layers of Al₂O₃, produced with one and five cycles, were deposited on a bulky ALD-made platinum surface. We directed accelerated hydrogen and deuterium atom beams onto the surface and measured energy dissipation to the material due to the collisions. By this RAT technique we could prove that in the first cycle a surface coverage of about 60 % aluminium is reached, ho-

3. Summary

mogeneously spread over the substrate. It was furthermore shown, that this incomplete monolayer shows an overlay of insulator and metal scattering, meaning no and a large energy loss to the surface. A layer of 1 nm thickness, corresponding to 4-5 monolayers only showed insulator scattering. The observed angular distribution was independent on stoichiometry, roughness and density.

Within the cooperation with BASF precursors for cobalt deposition were tested. Although a satisfying film growth remained elusive (best gpc = $0.01 \text{ \AA} \cdot \text{cycle}^{-1}$), the compound class $\text{Co}(\text{NTMS}_2)_2(\text{PR}_3)$ was intensively characterized in respect to stability and evaporation parameters as a function of structural differences. It was possible to achieve highest thermal stability and volatility with compound $\text{Co}(\text{NTMS}_2)_2(\text{P}^i\text{Pr}_2^t\text{Bu})$. Furthermore a mechanism is suggested to interpret these results.

Tantalum chalcogenide containing films were successfully synthesized using the CVD precursor $\text{Ta}(\text{NMe}_2)_5$ (**12**) with H_2O at very mild deposition temperatures, broadening the ALD-window, to form thin films of tantalum oxide with an outstanding roughnesses smaller than described for Al_2O_3 .

On the other hand a strategy for TaS_x film generation is presented, using H_2S as a coprecursor and a bubbler reservoir for **12**. Albeit the low roughness, ALD based deposition mechanisms and suitable growth rates were very promising, the films were contaminated with oxygen, which was proven to originate from H_2S impurities. However, the presented structures prove a novel ALD procedure for Tantalum sulphide containing layers.

4 Experimental Methods

4.1 *In Situ* Analysis: EI-MS and QCM

For the purpose of mechanistical insights to novel ALD procedures, *in situ* electron ionisation mass spectrometry (EI-MS) was used. The attached PfeifferVakuum PrismaPlus™ engine (QME 220 F3 Prisma Plus) extracts a fraction of the exhaust gas continuously and is able to analyse mass fragments from 1 up to 300 m/Z using a quadrupole field generated by four 16 cm tungsten magnet rods for ion separation (figure 4.1, 4). The analysed gas is generally extracted from the middle of the gas stream in the exhaust gas tube with a total distance to the substrate of 15 cm. As a second possibility, it may be extracted directly at the wafer surface position, with the disadvantage of long cannula pathway resulting in staggered detection (shown in figure 4.1 in red superposition). The MS can detect fragments in concentrations lower than $4 \cdot 10^{-12}$ hPa in the residual gas. Ionisation is performed by a cage like electron impact cavity (4.1, 3) with two filaments in open geometry. The ion detection can either be done with a Faraday or upstream electron multiplier (SEM) detector with 1013 V. With the program QUADERA it is possible to program highly accurate measuring strategies ranging from ionisation yield corrected oxygen quantification to multi ion detection (SEM-MID) to track predefined gas fragments (4.1, 6). The MS is evacuated by a turbomolecular pump (TM) with 90.000 rpm using the process scroll pump as the backing pump shown in figure 4.1 (S).

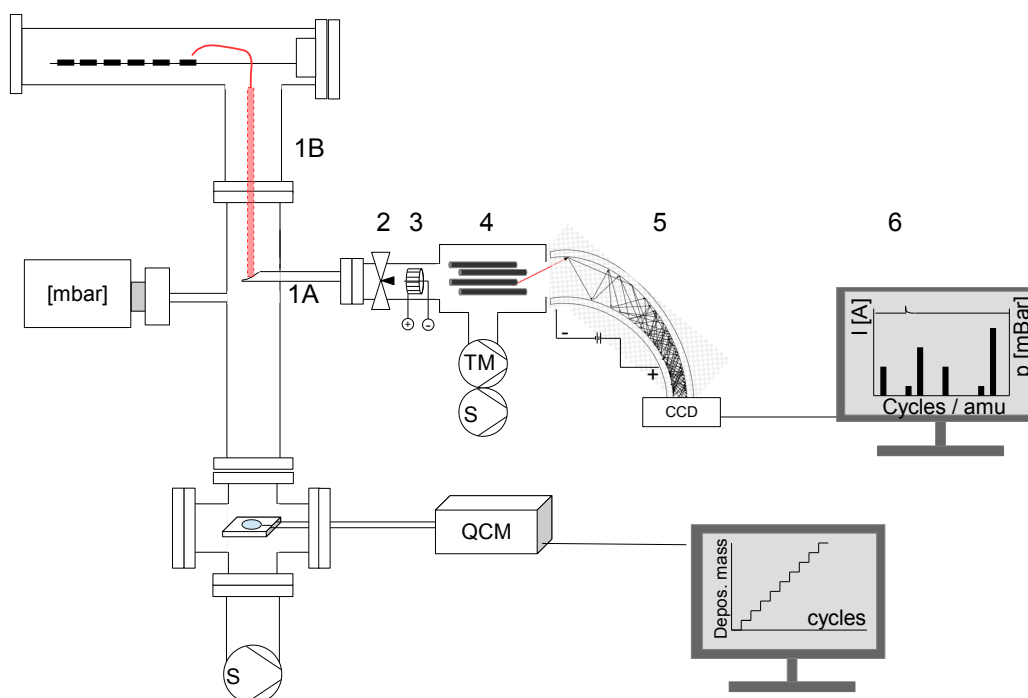


Figure 4.1: displays the arrangement of the MS and QCM and pressure detection as a side view of the chamber I. Displayed numbers at the MS referring to the different detection methods (normal: 1A, wafer position 1B, red, dashed), the needle inlet valve (2), electron impact ionisation cage (3) under high voltage, quadrupole tungsten rods and magnetic field and ion distraction (4) and single-channel electron multiplier with 1013 V (5) showing the cascade of secondary electrons resulting from the initial, primary radiation event. Signal analysis is done by QUADERA program (6). Under the MS we attached the QCM. The crystal is centered in the exhaust gas stream. Note, that the position of the process pump S is not exact, since bypass and exhaust purification are omitted for clarity.

For the annex of the QCM (JCM, SQM-160, 120 °C / 285 °C optimized crystals, 6 MHz), a dagger-like steel welding was constructed. With a window on the left and an opening for the oscillating crystal holder on the other side, it was attached in between the exhaust tube and the MS connection, as depicted in figure 4.1. The welding was planned to centre the crystal in the middle of the gas stream, exactly under the MS inlet. It furthermore allowed for a continuous inert gas purge, using the special throughput on the right side. Additionally, we aimed for the possibility of active heating, which is not possible in normal mode (the instrument was previously used with inductive heating). In the presented set-up, a heating coil can be

connected via a lead through at the position of the window (left side). The increase in mass of the crystal, the corresponding reduction in frequency, and the calculation of film thickness were performed by a Inficon display (SQM-100 “rate and thickness monitor”) on the one hand and by the corresponding computer program (SQM-160-COMM) on the other. For the generation of oscillation we used the oscillator remote sensor (OSC-100).

4.2 External Methods

In this thesis, a variety of methods were used to characterize film properties with respect of roughness, crystallinity, composition or impurities, and other parameters. The following paragraph will briefly describe the utilized instruments, applied parameters and present the possibilities of each method shortly. The general theory of the technique will not be discussed, but can be found in several reviews, which are cited in the paragraphs. Furthermore, this script will not comment on the procedure operation. This can be located in the "Reactor Manual" which gives a two-page step by step guidance (English) to run every instrument.

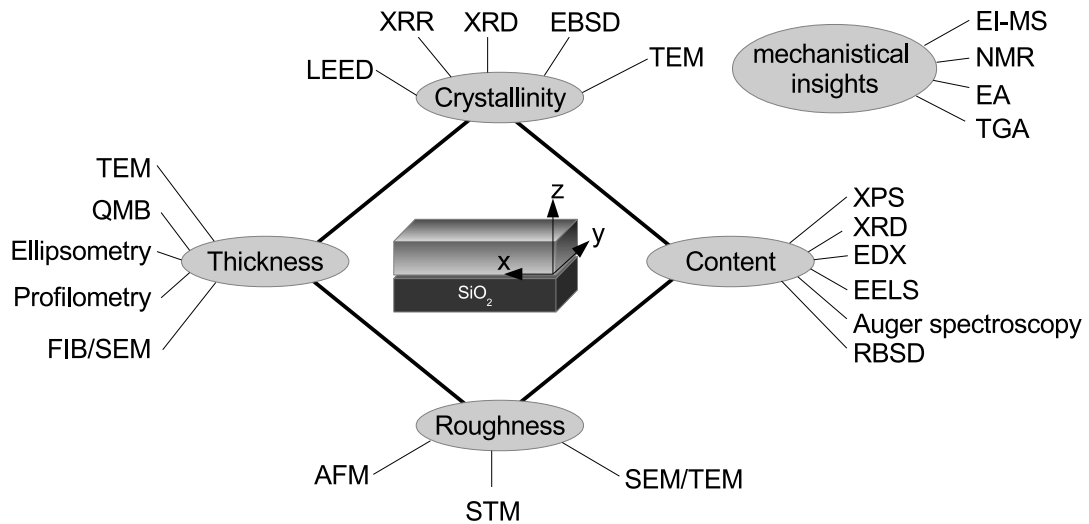


Figure 4.2: Characterisation methods utilized in this thesis, listed with respect to the investigated film characteristics.

4.2.1 X-Ray photo-electron spectroscopy (XPS)

XPS spectra were obtained using the Ceasar spectrometer with a DAR 400 source (Mg α -radiation) and a EA 125 hemispherical Energy Analyser (Omicron Nano Technology) with an emission current of 10.4 kilo Volt (kV). The displayed spectra are summarized data from three sweeps. Generally, the resolution was chosen to be 0.2 or 0.1 eV.

The content of films were evaluated using database average matrix relative sensitivity factors (AMRSFs)^[225,226] S for Mg-radiation using Gaussian signal model with integration areas A determined using Origin. The fraction X of each element n in the investigated film can be calculated by:

$$X_n = \frac{\frac{A_n}{S_n}}{\sum_i \left(\frac{A_i}{S_i} \right)} \quad (4.1)$$

Since the correction values originate from calculations, X_n should furthermore be corrected by the instruments factor which was set to one here.

4.2.2 Transition Electron Microscopy (TEM)

Images made with a transition electron microscope TEM were record by the author instructed by Dr. F. DÖRING and Dr. V. RHODDatis (CRC-Project B08). The TEM lamellas were cut at the Nova Nano SEM 650 using a Ga-ion beam with an approximate diameter of < 100nm. The lamellas were glued on a TEM-grid and transferred into the instrument. In this thesis several instruments were utilized, namely a CM12 (Phillips) and a Titan 80 300 (FEI) using a monochromator and CS correction for the purpose of ultra high resolution images.

Using TEM enables for detailed information, especially investigating multilayer structures, of interlayer thickness, crystallinity, density, roughness (2D), and mixing. As a disadvantage, this method is invasive and the preparation and measurement is as well expensive as time consuming.

4.2.3 Elemental Analysis (EA)

Elemental analysis was performed by the EA-lab in the department of inorganic chemistry, using standard methods for H, C, N, O and photometry (Perkin Elmer) for phosphor and atom-absorption-spectroscopy (Jena Analytik) for cobalt content.

4.2.4 Atomic Force Microscopy (AFM)

Two AFM instruments were used in this thesis, both used in the same modus with similar forces. Namely, these were the JPK nanowizard 3 (group of JAHNSHOFF, instruction by T.T. KLIESCH) and the Asylum Research MFP-3D (group of STEINEM, instruction by I. MEY and O. GRÄB). The author measured all images by himself using tapping AC-Air mode, which was best for hard, flat solids deposited in this thesis ("flat" is used differently here, meaning $R_a < 100$ nm). A type K cantilever with a needle diameter of 4 μm , a length of 125 μm , without coating was used, since thinner and more expensive models often show fast water adherence (within minutes), resulting in contact loose to the surface. The general measuring time scales varied in between a few quarters of an hour for a site of interest (SOI) area of 1000 x 1000 nm with a scanning rate of 0.1-0.5 Hz, and a resolution between 0.2-0.5 nm (set point = 900 mV, dive amplitude = 200-500 mV, integral gain = 10). Purely the roughness can be calculated, using AFM. For data interpretation and delineation of the surfaces, the program *Gwyddion 2.34* was used, applying water shed and tilt correction, if necessary.

4.2.5 Secondary Electron Microscopy with Energy Dispersive X-Ray Spectroscopy and Fast Ion Bombardment (SEM with EDX and SEM with FIB)

Surface images was recorded at two different SEM machines, both of them equipped with additional analysis techniques. Before vacuum was applied to start the electron

beam, the wafers were mounted on SEM-sample holder, glued with special conductive tape. For insulating material, this tape was furthermore folded to connect the top of the wafer too, avoiding charge effects. In general, the electron energy was kept at 5 or 10 keV, because radiation damage at > 20 keV changed the surface very fast. In this work, the Nova NanoSEM 650 (FEI) and the Nova 600 NanoLab (FEI) were used. With SEM the user is able to visualize surface artefacts with nm resolution such as hills or dust impurities giving rise to the homogeneity of the deposition. Furthermore, the amount of backscattered electrons allows to draw conclusions about metallicity of the surface and density.

The first named instrument carried a liquid Ga-ion source for TEM-lamella generation.^[227] The author prepared these lamellas instructed by V. RADISCH using a coverage of 2-originated, electron beam deposited, amorphous platinum. The sample was tilted by 52 ° and lamella surrounding material was sputtered with fast ion bombardment. The lamella was connected with a micromanipulator and transferred to a TEM grid, using furthermore electron-deposited platinum as glue.

The second instrument provides further analysis for energy distribution of backscattered electrons. In this work, EDX^[205] was used intensively with different electron energies (5, 10, 15, 20 kV) translating to different penetration depth. With this, one can calculate the film's composition quantitatively for third and higher row elements and give a good approximation of stoichiometry of the film using correction factors for second row elements. Furthermore, this instrument can utilize up to five different detectors, e.g. for insights in angular distribution of backscattered electrons. This can highlight domain structures, resulting from preliminary island growth in the ALD. With EDX the film thickness (R_n), or if the composition is known, also the film density (ρ) can be approximated using KANAYA's and OKAYAMAN's formula^[228]:

$$R = (0,0276 \cdot M \cdot E_0^{1,67}) / (Z^{0,89} \cdot \rho) \quad (4.2)$$

(R is the electron range, E_0 the beam energy, M the atomic mass and Z the atomic number, respectively.)

4.2.6 Ellipsometry

The thicknesses of the thin transparent oxide films were measured by spectroscopic ellipsometer Nanofilm EP4 (Accurion). Measurements were performed over a wavelength range of 360 to 800 nm at an angle of incidence of 50° . The film thicknesses of Al_2O_3 on SiO_2 were determined by fitting the optical properties of the oxide layer with the Cauchy model.^[229]

4.2.7 Profilometry

For post depositional profilometry use, prior to the deposition a thin Kapton-tape was glued on the wafer. After removal of the tape, the underlying surface remains unexposed, as depicted in figure 2.8. All measurements were performed at the Dektak 150 (Veeco) with a needle diameter of $12\ \mu\text{m}$ and an approximate maximal resolution of 1 nm with respect to the film thickness dimension (this is reduced by tape glue reminders at the step and dust particles on needle and surface). Scan rates were varied but ranged in the area of $10\ \mu\text{m} \cdot \text{s}^{-1}$ with scan distances of 1-3 mm, resulting in a spectrum measuring time of about five minutes. With profilometry, the user is able to investigate film thickness with moderate accuracy very fast. Investigating ALD-samples, the tape may also act as a flow barrier and the films thickness in front of and behind this barrier give rise to the CVD rate.

4.2.8 Scanning tunneling Microscopy (STM)

Data was acquired using a Bruker Standard scanning tunneling microscope (STM) with a constant current of 1 nA. The instrument is equipped with a NanoScope IV (Digital Instruments, Veeco Metrology Group) detector. For highly conductive

films the voltage was set to 10 mV and a pulled to tear tungsten wire is used with very thin needle ending. The data points were interpreted using the *NanoScope Software 6.12* and images were taken for this thesis using the above described *Gwyddion 2.34* program in a similar way AFM samples were treated.

4.2.9 Resistivity

The resistivity/conductivity of a film was estimated using a hand multimeter on at least ten different position of the wafer with a two-point measurement. Since measured data differed widely due to the internal error in measurement of the instrument, making quantitative interpretations unreliable, this method was used to derive the property, whether the film is conductive or insulating, on a qualitative level.

4.2.10 High Resolution Rutherford Back Scattering (HR-RBS)

HRRBS was performed under the guidance of Prof. Hans Hofsäss, using the 500 keV He²⁺ accelerator (II. physics) generating 450 keV He²⁺ particles, impacting the investigated surface. With a resolution of 1 keV, we were able to achieve structural informations in the range of about 1 nm.^[230] With RBS the user gets access to a non invasive depth profile of the sample with several hundreds of nm beam penetration.^[231] It furthermore resolves the relative atomic concentrations in different depth and can therefore be very powerful to evaluate e.g. variation in deposition mechanism in ALD-initiation phases or nucleation reactions.

Excursion: Interpretation of HR-RBS Spectra^[232]

The energy E_1 of the scattered projectile is reduced by a factor of k from the initial energy E_0 by an elastic, hard-sphere collision of the small particle (projectile) on or in the sample (target). This energy loss is displayed in the spectrum (*channel*).

$$E_1 = k \cdot E_0 \quad (4.3)$$

The kinematical factor k is proportional to the scattering angle ($\theta = 180^\circ$) and the unknown ratio of the masses of the projectile (m_1) and the target atom (m_2).

$$k \approx \left[\frac{\cos(\theta) + \sqrt{[m_2/m_1]^2 - \sin^2(\theta)}}{1 + m_2/m_1} \right]^2 \quad (4.4)$$

With this equation, the user is able to determine the mass of the corresponding surface atom. Furthermore, the probability ω of a scattering event is given by the differential cross-section from which the estimated signal intensity arises. This is proportional to the atomic number of the target nuclei (Z_2): the heavier the atom hit, the better the signal is resolved:

$$\omega = \left[\frac{Z_1 \cdot Z_2 \cdot e^2}{4 \cdot E_0} \right]^2 \cdot \frac{1}{(\sin(\theta/2))^4} \quad (4.5)$$

However, E_0 is furthermore reduced not only by nuclei scattering but also by interaction with electrons of the material. The resulting energy decrease is proportional to $\frac{Z_2}{E}$ and the depth, so basically to the amount of electrons passed. With this assumption the signal broadening is therefore proportional to the films thickness and furthermore the shift of a elemental signal with respect to its surface signal position indicates the depth of the nuclei hit. However, for binary compounds in particular and special amorphous elements, Z_2 is given as a mixture of both nuclei or in other words, the nuclei density differs. This is normally given in Atoms/cm² which on the one hand translates to the density, the binary phase stoichiometry or the films thickness. It is therefore useful, to determine the films thickness earlier by SEM, TEM or Profilometry, otherwise literature values are taken into account, which may not fit the actual order of the sample.

Since normally both values, density and thickness, are unknown, the spectrum has to be fitted by both values alternating in an allotted frame.

Presented data in this thesis were best fitted with an underlying 200 nm of amorphous SiO₂ (33% Si) on bulk Si, allowing for interpretation of light atom (C, N, O)

contribution to the top layer although for $Z_1 \approx Z_2$, signals overlapped.

4.2.11 Auger Spectroscopy

Auger Spectroscopy^[233] was performed in the scattering chamber *in situ*, described in chapter 2.3, which was performed by Y. DORENKAMP. All data were collected using a CMA 100 cylindrical mirror analyser (Omicron NanoTechnology) in the range of 20 to 3267.8 eV with a resolution of 0.5 %.^[234] Signal shift were corrected with respect to the zero signal and indexed by comparison with literature.^[220]

4.2.12 X-ray Powder Diffractometry and Reflectometry (XRD and XRR)

The use of non-invasive methods for film investigations is preferable and X-ray analysis, namely XRD and XRR are important tools. X-ray data was measured on a D8 Discover (Bruker AXS) instrument, using Cu-K α -radiation with the wavelength of 1.504 Å and a 1D-Goebelmirror using 1 mm slits to focus the beam on the sample. All spectra were taken using the detector in 1-D mode. The spectra were indexed with the instrument's Leptos 7.7 (Bruker AXS) software, also used for beam centering and intensity optimization in respect of the sample geometry on the sample holder.

For XRD data, a 2- Θ -scan was applied in the range of 5° to 140° preliminary, investigating film composition with five to ten minutes measuring time. For better resolution and increasing intensity, the parameter for the final spectra was set to 0.5 s per 0.01° increment, resulting in a 60 min time per spectrum. With XRD the user is able to determine film composition, crystallinity and orientation of domains, lattice plane dimensions and pair distribution function based calculations on bond distance in amorphous materials (resulting in a very broad signal).

Data for XRR was taken with similar parameters using a 2- Θ -scan in the range of 1° to 10° with slightly longer scan times and larger opening of the automatic slit al-

lowing for evaluable intensity. Spectra of XRR give rise to lattice dimensions in the range of Å for flat interfaces up to interface thicknesses of 150 nm. Furthermore, the electron density profile perpendicular to the surface can be evaluated as well as the interface roughness in the material. Finally, the position of the total reflection edge signal lead to the average assay density.

At this point, it can be mentioned, that during the thesis, based on the instrumental experience with other instruments, over one hundred single crystal service experiments were performed at 100 K on a Bruker D8 three-circle diffractometer, equipped with a PHOTON 100 CMOS detector and an INCOATEC microfocus source with Quazar mirror optics (Mo-K α -radiation, $\lambda = 0.71073$ Å). The data obtained were integrated with SAINT and a semi-empirical absorption correction from equivalents with SADABS was applied. The structure was solved and refined using the Bruker SHELX 2014 software package.^[235]

4.2.13 Schlenk Technique and Inert Gas Box

Sensitivity to oxygen and moisture of all utilized compounds made the handling under inert condition essential. Packing of steel containers, preparation of stability test, storage, cooling and preparation of NMR samples were performed in a MBraun argon filled inert gas box. During preparation, the box atmosphere contained a concentration of < 1 parts per million (ppm) for O₂ and H₂O, respectively. Sublimation tests were performed using a Schlenk line with argon, pumped by a membrane pump (PfeifferVakuum, DUO line, PK D58 112C).

4.2.14 Nuclear Magnetic Resonance (NMR)

NMR spectra were recorded on a Bruker Avance III 300 and were calibrated to the residual proton resonance of the solvent (C₆D₆: δ H = 7.16 ppm; d₈-THF: δ H = 3.58 ppm) at rt. Signal multiplicities are abbreviated as: s (singlet), d (doublet), t (triplet), m (multiplet), br (broad).

4.2.15 Thermogravimetric Analysis (TGA)

Stability tests of cobalt containing precursors were performed at BASF using a NET-ZSCH TG 209F1 Libra TGA209F1D-0106-L by L. HÖRING. The analysis was performed in nitrogen inert gas atmosphere and mass loss was detected in the range of 25 °C to 550 °C with a heating rate of 5 K · min⁻¹ in Al₂O₃-containers.

4.3 Chemicals

Table 4.1: Chemicals in this work with distributor.

chemical	distributor	CAS
MeCpPt(Me) ₃ (99 %)	ABCR	94442-25-5
AlMe ₃ (98 %)	ABCR	75-25-1
Ir(Acac) ₃ (99 %)	ABCR	15635-87-7
Co(NTMS ₂) ₂ (PMe ₃)	Synth. Gerkens	-
Co(NTMS ₂) ₂ (PEt ₃)	Synth. Gerkens	-
Co(NTMS ₂) ₂ (P ^t Bu ⁱ Pr ₂)	Synth. Gerkens	-
(Co(NTMS ₂) ₂) ₂ (TMEDA)	Synth. Gerkens	-
TaCl ₅ (99.99 %)	Alpha Aesar	7721-01-9
Ta(NMe ₂) ₅	ABCR	19824-59-0
Ta(NMe ₂) ₃ N ⁿ Bu (99.99 %)	ABCR	169896-41-7
TaO ^t Bu ₅ (99.99 %)	ABCR	51094-78-1
N(TMS) ₃ (98 %)	Sigma Aldrich	1586-73-8
Me ₂ S (99 %)	Alfa Aesar	642-92-0
MeSSMe (99 %)	ABCR	624-92-0
^t BuSH (99 %)	purified in group of Ackermann	75-66-1
N ₂ (99.999 %)	Linde	7727-37-9
O ₂ (99.999 %)	Linde	7782-44-7
Ar (99.999 %)	Linde	7440-37-1
H ₂ S in Ar (5/95 %)	Linde	7783-06-4

5 Experimental Section

5.1 General Preface

All precursors used in this work were attached to the reactor in Swagelok steel containers. These were filled in an argon glove box (MBraun), closed by a transport valve, which is a bellows-type valve (Swagelok, SS-4H-VCR, $C_V = 0.28$) or a ball valve (Swagelok, SS-62TVCR4, $C_V = 1.2$) and connected with VCR sealing (Swagelok, SS-4-VCR-2) to the chamber. Liquid and very volatile precursors were cooled to about $-30\text{ }^\circ\text{C}$ using small intervals of liquid nitrogen application to avoid distortion. The cavity in between the ALD and closing valve was heated and evacuated at least twenty times (after about ten evacuations no water and oxygen could be detected by the MS). To remove fractions of the remaining box atmosphere in the container the gas was let to the cavity in between ALD and transport valve. Importantly, the transport valve is closed during ALD valve is open but subsequently opened in between the pulses for about fifteen to sixty cycles, depending on the container's volume. If no pressure increase was detectable both valves were opened simultaneously three times. The heating coil was attached with isolating aluminium foil wrapped around the container. The temperature was measured at two positions of different masses, to ensure a homogeneous temperature: on the outside of the container, at the filling level of the precursor in between container and coil and above the closing valve, in between the precursor and ALD-Valve heating zone. Heating is continued for a minimum of 10 min before start of deposition to allow for a uniform heat distribution throughout the unstirred substance in the reservoir.

Unless otherwise stated, during deposition, for purging or gassing N_2 (5.0 Linde) or Ar (5.0 Linde) were used as a carrier gas with an average flow rate of $100\text{--}200\text{ mL} \cdot \text{min}^{-1}$ resulting in an overall pressure of about 5-6 mbar in the chamber and 0.6 mbar in the pump bypass. The chamber was generally heated, evacuated, and purged at least for two hours. As described in chapter 2.1, this was necessary since especially water was detected for hours during purge cycles without heating.

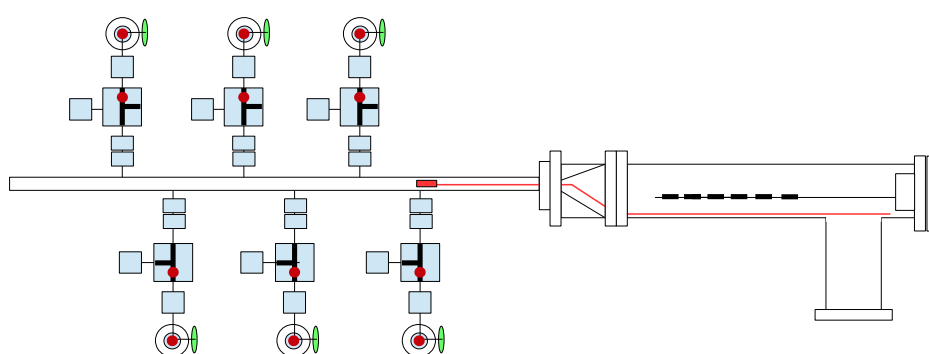


Figure 5.1: Scheme of the deposition reactor utilized in the following experiments. In red superposition: The special position wafer, fixed at a steel wire and positioned in the mix tube, with its flat surface pointing to the front of the outlet of precursor bottle 1.

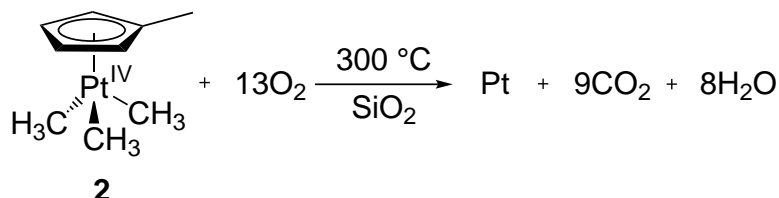
Wafer Pretreatment

Si / SiO_2 wafers were obtained from Si-Mat, Silicon Materials as round substrate with $d = 10\text{ cm}$ with a height of 1.5 mm. The substrates were cut with a water based wafer saw into sixty $10 \cdot 10\text{ mm}^2$ wafers which were stored with the deposition side glued on a plastic foil to avoid contamination. For the final ALD experiment, the wafer is cleaned in an ultrasonic bath in $iPrOH$, rinsed with $iPrOH$ and $MeOH$ twice and dried under a plastic canopy, avoiding dust soiling of the sample. For the final placement in the sample holder, the use of gloves and surgical mask is recommended.

Other substrates used in this work were magnesia oxide (MgO), sapphire (Al_2O_3), and silicon (Si), ordered at Crystal GmbH.

5.2 Metals

5.2.1 Platinum Deposition



Pt(MeCp)Me₃ **2** (500 mg, 1.5 mmol) was used as the platinum source. 0.5-1.0 mg of the precursor were evaporated per deposition cycle (dependent on the pulse length). Pt(MeCp)Me₃ is heated above its melting temperature to 75(±5) °C and the pulse-time was set to 3000-5000 ms. As a second precursor, O₂ (P 5.0, Linde) was applied, to reactivate the surface as described in detail in chapter 1.1.4. Oxygen was used directly from the gas container, without further purification, with a total pressure applied at the ALD-valve of 1050 mbar, so pulse-time kept at 5(±5) ms, increasing the pressure in the chamber by about 5 mbar. Since therefore the concentration of O₂ was quite high, purge-times were set to 120 s which was 3-4 times the value O₂ was still detectable by MS. For every 500 layers generated, a fresh filling of precursor **2** was attached, avoiding the precursor bottle to run empty. The following strategy parameter were used, if not otherwise stated:

$$t_4 = 5000 \text{ ms}, \quad t_{\text{purge } 1} = 120000 \text{ ms}, \quad t_{\text{O}_2} = 5 \text{ ms}, \quad t_{\text{purge } 2} = 120000 \text{ ms}$$

$$T_4 = 75\text{ }^\circ\text{C}, \quad T_{\text{chamber}} = 250\text{ }^\circ\text{C}, \quad T_{\text{Sample holder}} = 325\text{ }^\circ\text{C}, \quad T_{\text{Valve1-6}} = 125\text{ }^\circ\text{C}$$

$$T_{\text{MixTube}} = 120\text{ }^\circ\text{C}, \quad T_{\text{Gas}} = 120\text{ }^\circ\text{C}, \quad T_{\text{Exhaust}} = 120\text{ }^\circ\text{C}, \quad T_{\text{Gasdistributor}} = 120\text{ }^\circ\text{C}$$

$$Q_{\text{N}_2} = 100 \text{ (Mix Tube)} + 30 \text{ (Valves)} \frac{\text{mL}}{\text{min}} \text{ (variable area flowmeter)}$$

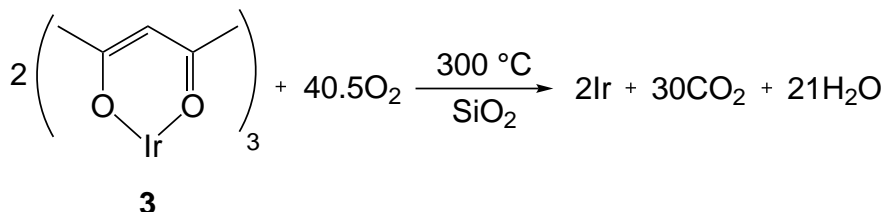
$$p_{\text{Sample holder}} = 3 \text{ mbar}, \quad p_{\text{Pump bypass}} = 0.5 \text{ mbar}$$

In another experiment, several platinum depositions were run at the commercial ALD chamber (6-port GemStar, ARRadianc) in the group of J. BACHMANN. Although metallic platinum film were obtained using the CVD precursor Pt(Acac)₂ **14** (800 mg, 2.0 mmol) together with O₂ (5.0 Linde) these were not investigated further, because of the finding of very high evaporation temperatures for **14** to the benefit of **2**.

Table 5.1: Thin film characterization

AFM:	(set point = 500 mV, drive amplitude = 300 mV, int. gain = 10, Type "K" cantilever): R _a = 0.98 nm, R _{max} = 8.6 nm.
XPS:	(anode voltage= 8 kV, emission current = 20 mA), Pt = 85.6 eV (4f _{7/2}), 91.2 eV (4f _{5/2}), 117 eV (br, 5s), 327.2 eV (4d _{5/2}), 345.0 eV (4d _{3/2}), 531.2 eV (4p _{3/2}), 621.8 eV (4p _{1/2}), C = 287.4 eV (1s), O = 542.8 eV (1s)
EDX:	(10 kV), E = 9.4 eV (L _α), 2.0 eV (M)
SEM:	(10 kV), Grain sizes = 25- 50 nm.
XRD:	(Cu-Kα = 1.504 Å) Pt[111] = 39.6 °

5.2.2 Iridium Deposition



$\text{Ir}(\text{Acac})_3$ (**3**) (1.00 g, 2.0 mmol) and O_2 (P 5.0, Linde) was utilized in this experiment forming metallic iridium layers. Pulse times for **3** are 5000 ms and 5 ms for oxygen, respectively. O_2 was used without further purification, with an overpressure of about 1050 mbar at the ALD-valve. The precursor **3** had to be heated above 170 °C, allowing sublimation, whereby the ALD-valve faced its temperature limit of 200 - 220 °C. The reactor temperatures were set to 200 °C, but some reactor parts maintained a maximum temperature of 180 °C during deposition, namely the inert gas distributor and the connection between gas heating and viscose flow tube. The substrate was heated to 325 °C. Different experiments were made, changing the cycle amount from 300 to 800 cycles.

$$t_4 = 5000 \text{ ms}, \quad t_{\text{purge 1}} = 120000 \text{ ms}, \quad t_{\text{O}_2} = 5 \text{ ms}, \quad t_{\text{purge 2}} = 120000 \text{ ms}$$

$$T_4 = 175 \text{ }^\circ\text{C}, \quad T_{\text{chamber}} = 250 \text{ }^\circ\text{C}, \quad T_{\text{Sample holder}} = 325 \text{ }^\circ\text{C}, \quad T_{\text{Valve1-6}} = 185 \text{ }^\circ\text{C}$$

$$T_{\text{MixTube}} = 200 \text{ }^\circ\text{C}, \quad T_{\text{Gas}} = 200 \text{ }^\circ\text{C}, \quad T_{\text{Exhaust}} = 150 \text{ }^\circ\text{C}, \quad T_{\text{Gasdistributor}} = 150 \text{ }^\circ\text{C}$$

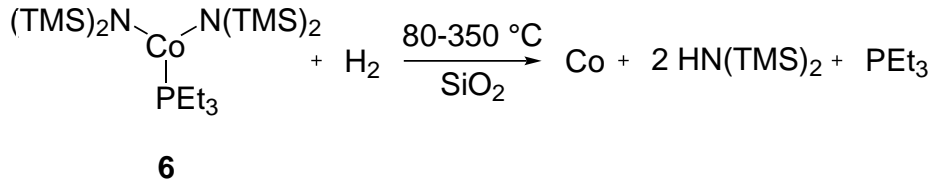
$$Q_{\text{N}_2} = 100 \text{ (Mix Tube)} + 30 \text{ (Valves)} \frac{\text{mL}}{\text{min}} \text{ (variable area flowmeter)}$$

$$p_{\text{Sample holder}} = 3 \text{ mbar}, \quad p_{\text{Pump bypass}} = 0.2 \text{ mbar}$$

Table 5.2: Thin film characterization.

AFM:	(set point = 500 mV, drive amplitude = 300 mV, int. gain = 10, Type “K” cantilever): $R_a = 1.30\text{nm}$, $R_{\text{max}} = 7.0\text{ nm}$.
XPS:	(anode voltage = 8 kV, emission current = 20 mA), Ir = 75.1 eV ($4f_{7/2}$), 78.1 eV ($4f_{5/2}$), 308.6 eV ($4d_{5/2}$), 324.6 eV ($4d_{3/2}$), 506.1 eV ($4p_{3/2}$), 614 eV (br, $4p_{1/2}$), 695 eV (4s) C = 297.1 eV (1s), O = 543.1 eV (1s).
SEM/TEM:	(10 kV), $G_{\text{pc}} = 0.5\text{ \AA/cycle}$.

5.2.3 Cobalt Deposition



Co(NTMS)₂(PEt₃) (300 mg, 0.60 mmol) **6** and H₂ was used in this deposition experiment. Pulse times for **6** were 1000 ms in the first and 3000 ms in later experiments. H₂ was used without further purification with a special manometer (Linde, HiQ, C200HV/2-2) and a total pressure applied at the ALD-valve of 150 mbar, so pulse-time kept at 5(±5) ms, increasing the pressure in the chamber by about 1-2 mbar. In all experiments, 1000 deposition cycles were applied to a 200 °C SiO₂ surface. During this depositions, the construction was changed by adding the QCM to the setup.

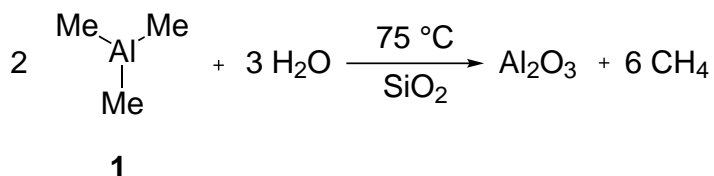
- 1.) $t_4 = 1000 \text{ ms}$, $t_{\text{purge 1}} = 30000 \text{ ms}$, $t_{\text{H}_2} = 5 \text{ ms}$, $t_{\text{purge 2}} = 125000 \text{ ms}$
 $T_4 = 105\text{ }^\circ\text{C}$, $T_{\text{chamber}} = 200\text{ }^\circ\text{C}$, $T_{\text{Sample holder}} = 200\text{ }^\circ\text{C}$, $T_{\text{Valve1-6}} = 185\text{ }^\circ\text{C}$
 $T_{\text{MixTube}} = 200\text{ }^\circ\text{C}$, $T_{\text{Gas}} = 75\text{ }^\circ\text{C}$, $T_{\text{Exhaust}} = 95\text{ }^\circ\text{C}$, $T_{\text{Gasdistributor}} = 120\text{ }^\circ\text{C}$
 $Q_{\text{N}_2} = 60 \text{ (Mix Tube)} + 20 \text{ (Valves)} \frac{\text{mL}}{\text{min}}$ (variable area flowmeter)
 $p_{\text{Sample holder}} = 2 \text{ mbar}$, $p_{\text{Pump bypass}} = 0.2 \text{ mbar}$
- 2.) $t_4 = 3000 \text{ ms}$, $t_{\text{purge 1}} = 40000 \text{ ms}$, $t_{\text{H}_2} = 5 \text{ ms}$, $t_{\text{purge 2}} = 60000 \text{ ms}$
 $T_4 = 105\text{ }^\circ\text{C}$, $T_{\text{chamber}} = 200\text{ }^\circ\text{C}$, $T_{\text{Sample holder}} = 200\text{ }^\circ\text{C}$, $T_{\text{Valve1-6}} = 185\text{ }^\circ\text{C}$
 $T_{\text{MixTube}} = 125\text{ }^\circ\text{C}$, $T_{\text{Gas}} = 75\text{ }^\circ\text{C}$, $T_{\text{Exhaust}} = 95\text{ }^\circ\text{C}$, $T_{\text{Gasdistributor}} = 150\text{ }^\circ\text{C}$
 $Q_{\text{N}_2} = 100 \text{ (Mix Tube)} + 30 \text{ (Valves)} \frac{\text{mL}}{\text{min}}$ (variable area flowmeter)
 $p_{\text{Sample holder}} = 2 \text{ mbar}$, $p_{\text{Pump bypass}} = 0.2 \text{ mbar}$

Table 5.3: Thin film characterization

XPS: (anode voltage= 8 kV, emission current = 20 mA), Co = 793.0 eV (2p_{3/2}), C = 296.0 eV (1s), O = 542.4 eV (1s).

5.3 Oxides and Sulfides

5.3.1 Aluminum Oxide Deposition



Trimethylaluminium **15** is pyrophory, explosive and had to be handled with special care. Additionally to the described procedure above, TMA was taken from a half frozen liquid with a cooled syringe, transferred to the chilled precursor bottle. After bringing out TMA from the inert gas box, it was stored in a fume hood for at least an hour, and controlled for temperature increase due to leakage and subsequent reaction. Because of the high vapor pressure it was again cooled before removing the box atmosphere carefully. Thus **15** was not heated, temperature was taken at the outside of the steel container during deposition to ensure continuous room temperature.

In 10 mL steel containers, 5.0 mL TMA (4.05 g, 56 mmol) **15** and 5 mL H₂O were attached to the reactor, lasting for about 3000 deposition cycles for both materials. Pulse times for both, TMA and water, taken as the second precursor and oxygen source, were set to 150 ms in general procedures, increasing the chamber pressure by 0.2-0.5 mbar. Both precursors did not need to be heated above room temperature while the substrate was heated to 75 °C and all other parts of the chamber to 65 °C, avoiding water condensation and long purge times as a consequence thereof. For the plot 2.9, the pulse time for TMA was changed from 5 ms to 1000 ms keeping all other parameters constant. Increasing the pulse length, the times were 5, 50, 100, 225, 500, and 1000 ms. The amount of deposition cycles differed with experiments: Thin films on Pt (chapter 2.3) were generated using 1 and 5 cycles. Experiments aiming for increased anchoring strength of Ru-based water oxidizing catalysts used 5 and 10 cycles. Reactor tests (chapter 2.2.1) employed 50 to 500

cycles in about fifty different experiments. Interlayers of Al_2O_3 , utilized in thermal conductivity measurements (chapter 2.3), were build using 300 cycles and 2000 cycles for reference material avoiding SiO_2 influence. Acting as a seed layer for TaS_x deposition, Al_2O_3 was used with 100 cycles.

$$t_{\text{TMA}} = 150 \text{ ms}, \quad t_{\text{purge 1}} = 120000 \text{ ms}, \quad t_{\text{H}_2\text{O}} = 150 \text{ ms}, \quad t_{\text{purge 2}} = 120000 \text{ ms}$$

$$T_{\text{TMA}} = T_{\text{H}_2\text{O}} = \text{RT}, \quad T_{\text{chamber}} = 65 \text{ }^\circ\text{C}, \quad T_{\text{Sample holder}} = 75 \text{ }^\circ\text{C}$$

$$T_{\text{Valve1-6}} = 65 \text{ }^\circ\text{C}, \quad T_{\text{MixTube}} = 65 \text{ }^\circ\text{C}, \quad T_{\text{Gas}} = 65 \text{ }^\circ\text{C}, \quad T_{\text{Exhaust}} = 65 \text{ }^\circ\text{C}$$

$$T_{\text{Gasdistributor}} = 65 \text{ }^\circ\text{C}$$

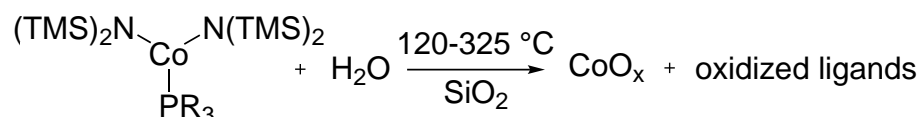
$$Q_{\text{N}_2} = 100 \text{ (Mix Tube)} + 30 \text{ (Valves)} \frac{\text{mL}}{\text{min}} \text{ (variable area flowmeter)}$$

$$p_{\text{Sample holder}} = 2 \text{ mbar}, \quad p_{\text{Pump bypass}} = 0.2 \text{ mbar}$$

Table 5.4: Thin film characterization.

AFM:	(set point = 500 mV, drive amplitude = 300 mV, int. gain = 10, Type "K" cantilever): $R_a = 0.66 \text{ nm}$, $R_{\text{max}} = 3.7 \text{ nm}$.
EDX:	(5 kV), $E_{\text{O}} = 0.52 \text{ eV (K}_\alpha)$, $E_{\text{Al}} = 1.49 \text{ eV (K}_\alpha)$, $\rho = 3.05 \pm 0.3 \frac{\text{g}}{\text{cm}^3}$
TEM, SE:	$G_{\text{pc}} = 1.94 \text{ \AA/cycle}$.

5.3.2 Cobalt Oxide Deposition



5 / 6

ALD with $\text{Co}(\text{NTMS}_2)_2(\text{PMe}_3)$:

$\text{Co}(\text{NTMS}_2)_2(\text{PEt}_3)$ **6** (200 mg, 0.40 mmol) and H_2O (5 mL). The pulse time for water was 150 ms. Previous findings using MS (can be found in detail in L. KOCHANNEK, 2015^[222]) identified the evaporation temperature to be $> 85\text{ }^\circ\text{C}$. For testing purposes with different parameters listed in the following table, the cycle amount was kept in between 100 and 1000.

In one experiment the substance was sublimed into the connection part, directly in front of the ALD-valve. Here, the precursor bottle was evacuated, heated to $> 85\text{ }^\circ\text{C}$ and the valve was opened to the cold area above.

Parameter changed:

$$t_x = 200, 1000, 3000, 5000 \text{ ms}$$

$$t_{\text{purge } 1/2} = 15, 30, 40 \text{ s}$$

$$T_x = 85, 95, 105\text{ }^\circ\text{C}$$

$$T_{\text{Sample holder}} = 140, 200, 325\text{ }^\circ\text{C}$$

Constant parameter:

$$T_{\text{chamber}} = 120\text{ }^\circ\text{C}, T_{\text{Valve1-6}} = 120\text{ }^\circ\text{C}$$

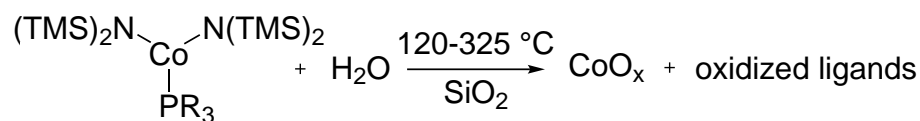
$$T_{\text{MixTube}} = 120\text{ }^\circ\text{C}, T_{\text{Gas}} = 75\text{ }^\circ\text{C}, T_{\text{Exhaust}} = 95\text{ }^\circ\text{C}, T_{\text{Gasdistributor}} = 100\text{ }^\circ\text{C}$$

$$Q_{\text{N}_2} = 100 \text{ (Mix Tube)} + 30 \text{ (Valves)} \frac{\text{mL}}{\text{min}} \text{ (variable area flowmeter)}$$

$$p_{\text{Sample holder}} = 1.5 - 2.0 \text{ mbar}, p_{\text{Pump bypass}} = 0.2 \text{ mbar}$$

Table 5.5: Thin film characterization

XPS: (anode voltage= 8 kV, emission current = 20 mA), Co = 73.2 eV ($3p_{1/2}$), 76.6 eV ($3p_{3/2}$), 782 eV ($2p_{1/2}$), 792.0 eV ($2p_{3/2}$), P = 145.8 (2s), 203.0 (2s), C = 295.8 eV (1s), O = 542.4 eV (1s).

**5 / 6**ALD with Co(NTMS₂)₂(PMe₃):

200 mg of Co(NTMS₂)₂(PMe₃) **5** (0.40 mmol) and H₂O (5 mL). The pulse time for water was 150 ms. Previous findings using MS (can be found in detail in L. KOCHANNEK, 2015^[222]) identified the evaporation temperature to be > 85 °C. For testing purposes with different parameters listed in the following table, the cycle amount was kept in between 100 and 1000.

In one experiment the substance was sublimed into the connection part, directly in front of the ALD-valve. Here, the precursor bottle was evacuated, heated to > 85 °C and the valve was opened to the cold area above.

Parameter changed:

$$t_5 = 200, 1000, 3000, 5000 \text{ ms}$$

$$t_{\text{purge } 1/2} = 15, 30, 40 \text{ s}$$

$$T_5 = 85, 95, 105 \text{ }^\circ\text{C}$$

$$T_{\text{Sample holder}} = 140, 200, 325 \text{ }^\circ\text{C}$$

Constant parameter:

$$T_{\text{chamber}} = 120 \text{ }^\circ\text{C}, T_{\text{Valve1-6}} = 120 \text{ }^\circ\text{C}$$

$$T_{\text{MixTube}} = 120 \text{ }^\circ\text{C}, T_{\text{Gas}} = 75 \text{ }^\circ\text{C}, T_{\text{Exhaust}} = 95 \text{ }^\circ\text{C}, T_{\text{Gasdistributor}} = 100 \text{ }^\circ\text{C}$$

$$Q_{\text{N}_2} = 100 \text{ (Mix Tube)} + 30 \text{ (Valves)} \frac{\text{mL}}{\text{min}} \text{ (variable area flowmeter)}$$

$$p_{\text{Sample holder}} = 1.5 - 2.0 \text{ mbar}, p_{\text{Pump bypass}} = 0.2 \text{ mbar}$$

Table 5.6: Thin film characterization

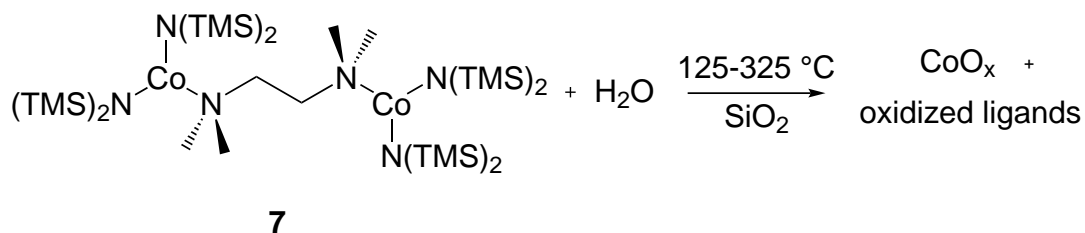
XPS: (anode voltage= 8 kV, emission current = 20 mA), Co = 73.2 eV (3p_{1/2}), 76.6 eV (3p_{3/2}), 782 eV (2p_{1/2}), 792.0 eV (2p_{3/2}), P = 145.8 (2s), 203.0 (2s), C = 295.8 eV (1s), O = 542.4 eV (1s).

CVD with $\text{Co}(\text{NTMS}_2)_2(\text{PEt}_3)$:

$\text{Co}(\text{NTMS}_2)_2(\text{PEt}_3)$ **6** (200 mg, 0.40 mmol) is heated to 85 and 95 °C in two different experiments and sublimed onto a hot SiO_2 surface. Pulse times of 60 s were applied with purge times of 10 s without using a second precursor. All reactor parts remained at temperatures described in previous experiments with **6** but the substrate was heated to 325 °C.

Table 5.7: Thin film characterization

XPS: (anode voltage= 8 kV, emission current = 20 mA), Co = 65.8 eV ($3p_{1/2}$), 68.8 eV ($3p_{3/2}$), 508.0 (LMM), 776.8 eV, 776.8 eV ($2p_{1/2}$), 792.0 eV ($2p_{3/2}$), P = 140.0 (2s), 203.0 (2s), C = 298.8 eV (1s), O = 542.4 eV (1s).



(Co(NTMS₂)₂)₂(TMEDA) **7** (200 mg, 0.23 mmol) and H₂O (5 mL) were separately pulsed to the substrate SiO₂ in three experiments. The pulse time for water was 150 ms. Previous findings using MS (can be found in detail in L. KOCHANNEK, 2015^[222]) identified the evaporation temperature to be > 50 °C. For testing purposes with different parameters listed in the following table, the cycle amounts used were 230, 270 and 400.

Elevated numbers refer to the experiment:

$$t_7 = 1500 \text{ ms}, \quad t_{\text{purge } 1} = 15000^{(1)}, 30000^{(2,3)} \text{ ms}, \quad t_{\text{H}_2\text{O}} = 100 \text{ ms}, \quad t_{\text{purge } 2} = 60000 \text{ ms}$$

$$T_7 = 50^{(1)}, 60^{(2)}, 75^{(3)} \text{ }^\circ\text{C}, \quad T_{\text{chamber}} = 65 \text{ }^\circ\text{C}, \quad T_{\text{Sample holder}} = 250^{(1)}, 125^{(2)}, 325^{(3)} \text{ }^\circ\text{C},$$

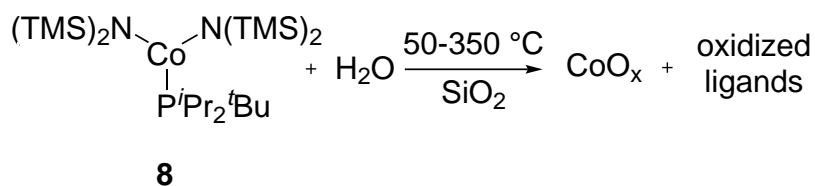
$$T_{\text{Valve1-6}} = 125 \text{ }^\circ\text{C}, \quad T_{\text{MixTube}} = 125 \text{ }^\circ\text{C}, \quad T_{\text{Gas}} = 125 \text{ }^\circ\text{C}, \quad T_{\text{Exhaust}} = 125 \text{ }^\circ\text{C}$$

$$T_{\text{Gasdistributor}} = 125 \text{ }^\circ\text{C}$$

$$Q_{\text{N}_2} = 60 \text{ (Mix Tube)} + 20 \text{ (Valves)} \frac{\text{mL}}{\text{min}} \text{ (variable area flowmeter)}$$

$$p_{\text{Sample holder}} = 2 \text{ mbar}, \quad p_{\text{Pump bypass}} = 0.2 \text{ mbar}$$

No films could be obtained.



500 mg of $\text{Co}(\text{NTMS})_2(\text{P}^i\text{Bu}^i\text{Pr}_2)$ **8** in a normal steel container was attached to the chamber and the reservoir was evacuated. The compound was heated to 75 °C and sequentially pulsed to a SiO_2 surface, using water as the second precursor. 10 mL of H_2O was demineralized and boiled with a slow purge flow of Ar is led through the hot liquid for purification. the pulse time of water was 150 ms, increasing the chamber pressure by about 0.3 mbar. In addition to the changed parameter, the construction was changed: firstly, the closing valve (SS-4-VCR) was exchanged by a ball valve (Swagelok, SS-62TVCR4), increasing the C_V value by a factor of ten. In several experiments, the flow was varied resulting in a chamber pressure of 1, 3 and 10 mbar.

In another experiment, a bubbler (Precision Fabricators Ltd., PF-25CCHBC-G) was connected to a secondary nitrogen inert gas steam, evacuated and pulse times was chosen to be 200 ms. Here, 5 g of $\text{Co}(\text{NTMS})_2(\text{P}^i\text{Bu}^i\text{Pr}_2)$ **8** was attached to the chamber and pulsed to a SiO_2 surface. The compound was heated to 75 °C and sequentially pulsed to a SiO_2 surface, using water as the second precursor. 10 mL of H_2O was demineralized and boiled with a slow purge flow of Ar is led through the hot liquid for purification. The pulse time of water was 150 ms, increasing the chamber pressure by about 0.3 mbar.

$$T_{\mathbf{8}} = 75\text{ }^\circ\text{C}, \quad T_{\text{chamber}} = 65 - 200\text{ }^\circ\text{C}, \quad T_{\text{Sample holder}} = 50 - 300\text{ }^\circ\text{C}, \quad T_{\text{Valve1-6}} = 90\text{ }^\circ\text{C}$$

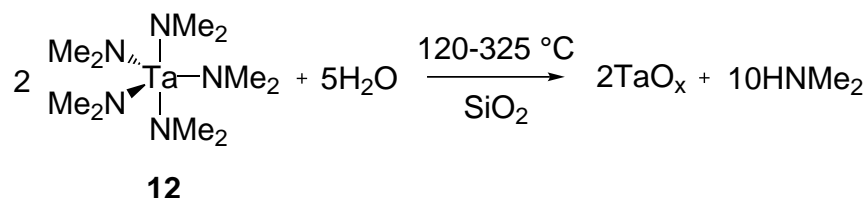
$$T_{\text{MixTube}} = 85\text{ }^\circ\text{C}, \quad T_{\text{Gas}} = 85\text{ }^\circ\text{C}, \quad T_{\text{Exhaust}} = 85\text{ }^\circ\text{C}, \quad T_{\text{Gasdistributor}} = 85\text{ }^\circ\text{C}$$

$$Q_{\text{N}_2} = 10 - 500 \text{ (Mix Tube)} + 3 - 500 \text{ (Valves)} \frac{\text{mL}}{\text{min}} \text{ (variable area flowmeter)}$$

$$p_{\text{Sample holder}} = 1, 3, 10 \text{ mbar}, \quad p_{\text{Pump bypass}} = 0.2, 0.8, 2.1 \text{ mbar}$$

No films could be obtained.

5.3.3 Tantalum Oxide Deposition



2.0 g of Ta(NMe₂)₅ **16** (5 mmol) were attached to the chamber, evacuated and reacted with water on a SiO₂ substrate, heated to various temperatures in between 120 and 300 °C. The flow was changed to result in different chamber pressures of 0.5, 3, 5 and 10 mbar.

$$t_{12} = 5000 \text{ ms}, \quad t_{\text{purge } 1} = 60 - 120 \text{ s}, \quad t_{\text{H}_2\text{O}} = 150 \text{ ms}, \quad t_{\text{purge } 2} = 120 \text{ s}$$

$$T_{12} = 60 - 130 \text{ }^\circ\text{C}, \quad T_{\text{chamber}} = 65 - 200 \text{ }^\circ\text{C}, \quad T_{\text{Sample holder}} = 80 - 325 \text{ }^\circ\text{C},$$

$$T_{\text{MixTube}} = 85 \text{ }^\circ\text{C}, \quad T_{\text{Gas}} = 85 \text{ }^\circ\text{C}, \quad T_{\text{Exhaust}} = 85 \text{ }^\circ\text{C}, \quad T_{\text{Gasdistributor}} = 85 \text{ }^\circ\text{C}$$

$$T_{\text{Valve1-6}} = 90 \text{ }^\circ\text{C}, \quad T_{\text{specialposition}} = 110 \text{ }^\circ\text{C}$$

$$Q_{\text{N}_2} = 100 \text{ (Mix Tube)} + 30 \text{ (Valves)} \frac{\text{mL}}{\text{min}} \text{ (variable area flowmeter)}$$

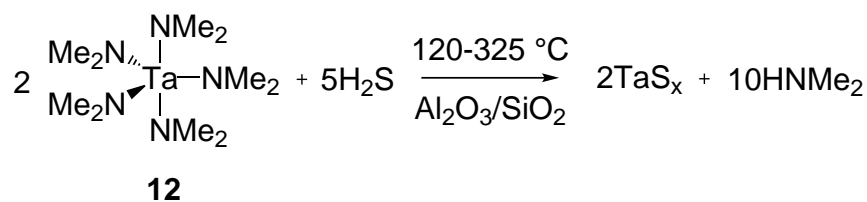
$$p_{\text{Sample holder}} = 1, 8 \text{ mbar}, \quad p_{\text{Pump bypass}} = 0.2, 1.3 \text{ mbar}$$

Table 5.8: Thin film characterization (special position):

EDX:	(10 keV), Ta: 1.33 keV, 1.72 keV (K α), 1.96 keV O: 0.52 keV (K α), C: 0.27 keV (K α)
AFM:	(set point = 500 mV, drive amplitude = 300 mV, int. gain = 10, Type "K" cantilever): R _a = 0.45 nm.
RBS:	(450 keV), Ta = 19 %, O = 41 %, C = 10 %, N = 30 %

5.3.4 Tantalum Sulfide Deposition

Thin films could be obtained using a bubbler with the following parameters. Sublimation temperature and stability properties were obtained using normal steel bottles in previous experiments. Furthermore, different sulphur sources were tested with respect to concentration to pulse length dependency. However, the parameters shall not be explained in more detail, because films only could be observed using H₂S. The experimental can be reviewed in the electronic lab journal of the reactor and additionally in T. MÜNCH, 2017^[223]. In conclusion, precursor **9**, **11** and **12** were exposed to ^tBuSH, MeSMe and MeSSMe on a SiO₂ surface at different temperatures each.



A bubbler (Precision Fabricators Ltd., PF-25CCHBC-G), filled with 5.0 g of $\text{Ta}(\text{NMe}_2)_5$ **12** (12.5 mmol) was attached to the chamber. The in-between space of ALD-valve and bubbler was heated and evacuated. Reminders of box atmosphere were removed and the bubbler was connected to the secondary N_2 stream. This was evacuated several times using an additional membrane pump (Pfeiffer, Duo0004B). The overall pressure increase of a pulse into the reactor, after two minutes of continuous inlet was tested, applying minimal pressure to the bubbler, reducing the secondary nitrogen flow by three valves with very small C_V values. Reaching a pressure increase of about 3 mbar, the deposition was started, using 200 ms pulse time for **12** and 5 ms for H_2S , respectively. H_2S was used without further purification, applying a total pressure of 1.10 bar to the ALD-valve. The pulse of H_2S in Ar increased the pressure of the chamber by 5 mbar.

$$t_{12,\text{bubbler}} = 200 \text{ ms}, \quad t_{\text{purge 1}} = 120\text{s}, \quad t_{\text{H}_2\text{S}} = 5 \text{ ms}, \quad t_{\text{purge 2}} = 120\text{s}$$

$$T_{12} = 95, 110\text{ }^\circ\text{C}, \quad T_{\text{chamber}} = 100 - 200\text{ }^\circ\text{C}, \quad T_{\text{Sample holder}} = 120 - 325\text{ }^\circ\text{C},$$

$$T_{\text{Valve1-6}} = 110\text{ }^\circ\text{C}, \quad T_{\text{MixTube}} = 110\text{ }^\circ\text{C}, \quad T_{\text{Gas}} = 110\text{ }^\circ\text{C}, \quad T_{\text{Exhaust}} = 125\text{ }^\circ\text{C}$$

$$T_{\text{Gasdistributor}} = 110\text{ }^\circ\text{C}, \quad T_{\text{Specialposition}} = 110\text{ }^\circ\text{C},$$

$$Q_{\text{N}_2} = 60 \text{ (Mix Tube)} + 20 \text{ (Valves)} \frac{\text{mL}}{\text{min}} \text{ (variable area flowmeter)}$$

$$p_{\text{Sample holder}} = 2 \text{ mbar}, \quad p_{\text{Pump bypass}} = 0.2 \text{ mbar}$$

Table 5.9: Thin film characterization:

EDX:	(5 and 10 keV), Ta: 1.33 keV, 1.95 keV Si, Ta: 1.74 keV ($K\alpha$), S: 2.31 keV ($K\alpha$), O: 0.52 keV ($K\alpha$), C: 0.27 keV ($K\alpha$)
AFM:	(set point = 500 mV, drive amplitude = 300 mV, int. gain = 10, Type "K" cantilever): $R_a^{SiO_2} = 0.45$ nm, $R_a^{Al_2O_3} = 0.42$ nm.
RBS:	(450 keV), Sample 95 °C: Ta = 25 %, S = 11 %, O = 64 %, C = 0 %, N = 0 %; Sample 110 °C: Ta = 23 %, S = 18 %, O = 49 %, C = 0 %, N = 0 %

6 Appendix

6.1 Abbreviations

Acac	acetylacetylen	60
AFM	atomic force microscopy	
ALD	Atomic Layer Deposition	1
AMM	acoustic mismatch model	24
AMRSFs	average matrix relative sensitivity factors	109
CBS	circular backscatter	
CDW	charge density wave	31
cm	centimetre	
Cp	cyclopentadienyl	41
CVD	chemical vapour deposition	3
DMM	diffuse mismatch model	24
DOS	density of states	34
EA	elemental analysis	89
EDX	energy dispersive X-ray spectroscopy (X-ray spectroscopy)	
EELS	electron energy loss spectroscopy	55
EI-MS	electron ionisation mass spectrometry	
eV	electronvolt	

FTIR	Fourier transform IR	15
g	gram	
GI	grazing incidence	21
gpc	growth per cycle [$\text{\AA}/\text{cycle}$]	6
GUI	graphical user interface	47
h	hour	
HER	hydrogen evolution reaction	31
hPa	hectopascal	
HR-TEM	high resolution transition electron microscopy	57
HR	high resolution	79
HRRBS	high resolution Rutherford back scattering	
Hz	Hertz	
ICP	inductively coupled plasma	20
IR	infra-red spectroscopy	
K	Kelvin	
keV	kilo electron Volt	
kV	kilo Volt	109
LEED	low angle electron-electron diffraction	21
mA	milliampere	
mbar	millibar	44
MCD	multi current detection	41
Me	methyl	41
mg	milligram	
MHz	megahertz	

min	minutes	
mK	millikelvin	
mL	milliliter	
ML	monolayer	
mm	millimetre	
mmol	millimol	
MS	mass spectrometry	21
ms	milliseconds	
MSD	mean squared displacement	18
mV	millivolt	
nA	nanoampere	
nm	nanometre	
NMR	Nuclear magnetic resonance	88
OES	optical emission spectroscopy	21
PE	plasma-enhanced	10
PEALD	plasma enhanced ALD	15
PEEM	photoemission electron microscopy	31
PES	Photoemission Studies	15
PLD	pulsed laser deposition	3
ppb	parts per billion	42
ppm	parts per million	116
QCM	quartz crystal microbalance	15
RAT	Rydberg atom tagging	28
RBS	Rutherford backscattering spectroscopy	96

ROI	reagion of interest	53
rpm	rounds per minute	
rt	room temperature.....	22
s	seconds	
SAXS	small angle X-ray scattering	21
sccm	standard cubic centimeter per minute	18
SE	spectroscopic ellipsometry	21
SEM	electron multiplier	105
SEM	scanning electron microscopy or microscope	
SERS	surface-enhanced Raman spectroscopy	21
SMFD	synchronously modulated flow and draw	20
SOI	site of interest	110
SR-PES	synchrotron radiation photoemission spectroscopy	21
STM	scanning tunnelling microscopy	65
TDLAS	tunable diode laser absorption spectroscopy	21
TEM	tranistion electron microscopy.....	53
TGA	thermogravimetric analysis	
THF	tetrahydrofuran	93
THz	terahertz	
TM	transition metal	33
TMA	trimethylaluminium	5
TMDs	transition metal dichalcogenides.....	31
TOF	time of flight	
TTR	transient temperaturedependent reflectivity.....	26

UHV	ultra high vacuum.....	55
UPS	ultraviolet photoelectron spectroscopy.....	21
W	Watt	
XAFS	X- ray absorption fine structure.....	21
XANES	X-ray absorption near-edge spectroscopy.....	21
XAS	X-ray absorption spectroscopy.....	21
XPS	X-Ray photoelectron spectroscopy.....	62
XRD	X-ray diffraction.....	57
XRF	X-Ray fluorescence.....	21
XRR	X-Ray reflectometry.....	21

Table 6.1: Sum formula and corresponding reference number of applied chemicals in this document.

formula	textlabel
AlMe_3	1
$\text{Pt}(\text{MeCp})(\text{Me})_3$	2
$\text{Ir}(\text{Acac})_3$	3
$\text{Co}(\text{NTMS}_2)(\text{C}_4\text{H}_8\text{O})$	4
$\text{Co}(\text{NTMS}_2)(\text{PMe}_3)$	5
$\text{Co}(\text{NTMS}_2)(\text{PEt}_3)$	6
$\text{Co}(\text{NTMS}_2)(\text{P}^i\text{Pr}^t\text{Bu})$	8
$(\text{Co}(\text{NTMS}_2)_2)_2(\text{TMEDA})$	7
TaCl_5	9
$\text{Ta}(\text{O}^n\text{Bu})_5$	10
$\text{Ta}(\text{NEt}_2)_3(\text{N}^t\text{Bu})$	11
$\text{Ta}(\text{NMe}_2)_5$	12
$\text{Si}(\text{OEt})_3((\text{CH}_2)_2\text{SH})$	13
$\text{Pt}(\text{Acac})_2$	14

List of Figures

1.1	PSE of ALD possibilities.	2
1.2	ALD Schema	2
1.3	Al ₂ O ₃ on trench structure	4
1.4	ALD window	6
1.5	Common ALD precursors with examples.	7
1.6	Thermal ALD metal deposition.	10
1.7	ALD initiation phase during deposition of Co.	11
1.8	Display of direct third row transition metals ALD for various metals.	12
1.9	General description of a noble metal ALD cycle	13
1.10	Discussed Platinum ALD self-limiting mechanisms.	14
1.11	SEM image of shrinking size of transistors from 2009 to today	16
1.12	First example of a ALD chamber in a patent.	18
1.13	Schematic representation of the three different types of plasma-assisted atomic layer deposition	20
1.14	Specular versus diffuse scattering, can be nm to μm	24
1.15	TTR setup.	27
1.16	Set up of the RAT-experiment.	29
1.17	Energy loss spectrum of scattered hydrogen atoms from a Gold and Xenon surface.	29
1.18	Tantalum AACVD shown by Peters et al..	31
1.19	Proposed ALD-cycle forming TaS ₂ thin films with different precursors.	32

2.1	Scheme of the deposition chamber.	39
2.2	Calculation on laminar flow in the chamber and mixing tube.	40
2.3	Flow diagram of the bubbler.	40
2.4	Simplified flow diagram of the execution sequence running a deposition.	45
2.5	Flow diagram of reactor control	47
2.6	GUI first page	48
2.7	GUI second page	49
2.8	Colour of Al_2O_3	51
2.9	Test of ALD to CVD ration in the novel set-up using Al_2O_3 deposition with increasing TMA concentration/amount in the gas stream.	52
2.10	Thickness to cycle ratio of Al_2O_3	52
2.11	AFM image of Al_2O_3	54
2.12	Ellipsometry Δ and Ψ plots of Al_2O_3 on SiO_2	54
2.13	EDX of aluminium oxide	55
2.14	Catalyst anchored by ALD.	58
2.15	Detailed description of an iridium metal ALD cycle with oxygen	59
2.16	MS investigations on Iridium depositions using 3 and O_2	60
2.17	AFM image of iridium.	61
2.18	SEM image of 30 nm metallic iridium.	61
2.19	XPS of metallic iridium layer.	62
2.20	SEM images of SiO_2 wafer exposed to 25, 50 and 100 cycles of Pt deposition using MeCpPtMe_3 and Oxygen and Pt domains by CBS detector.	64
2.21	STM of Pt.	65
2.22	AFM image of Platinum.	66
2.23	XRR spectrum of an about 15 nm platinum film on 200 nm SiO_2 on Si.	66
2.24	XPS of 15 nm Pt	67
2.25	TEM image of a sandwich structure showing reproducibility of Pt	69

2.26 TEM image of a sandwich structure with increasing Pt thickness and constant Al ₂ O ₃ thickness showing eleven interfaces.	70
2.27 Schematic view on the TTR experiment with TEM image of the investigated structure	71
2.28 TTR measurement of three different samples showing the effect of interlayer on energy dissipation.	72
2.29 TTR measurement of three different samples showing the effect of interlayer on energy dissipation.	72
2.30 Phononic DOS in utilized materials in the presented nanolaminates. .	74
2.31 Samples utilized in RAT-experiments.	76
2.32 Hydrogen flux at the detector scattered from different interfaces. . . .	77
2.33 Auger spectrum of different samples in RAT experiment.	78
2.34 Energy loss spectrum of hydrogen and deuterium atoms scattering from different Al ₂ O ₃ samples.	78
2.35 TEM image of a 50 nm Pt sample on SiO ₂ (a) and EELS mapping showing thickness of five cycles Al ₂ O ₃	80
2.36 RAT experiment angular distributioscattering hydrogen from bulk and thin Al ₂ O ₃	81
2.37 Hydrogen scattering from ML-fraction on Pt with different v_s compared with Pt.	82
2.38 Energy loss spectrum of H-Atoms of different energies impacting different surfaces.	82
2.39 Precursor for SiO ₂ -ALD	83
2.40 MS track of SiO ₂ deposition	83
2.41 Employed Co containing Precursor for Co and CoOx deposition	84
2.42 Aperatus for stability test of Co containing precursor.	84
2.43 TGA of 6 and 7) and 8	85
2.44 MS spectrum of Co(NTMS ₂) ₂ (P ⁱ BuPr ₂)	86
2.45 Pressure dependence of the sublimation of (8)	87

2.46 3D-MS spectrum of 8	88
2.47 QCM track of a Co deposition experiment with $\text{Co}(\text{NTMS}_2)_2\text{PEt}_3$ and Water and XPS data of this sample.	90
2.48 MS spectrum of $\text{Co}(\text{NTMS}_2)(\text{P}^t\text{Bu}^i\text{Pr})$	91
2.49 NMR spectrum of $\text{Co}(\text{NTMS}_2)_2\text{PEt}_3$ residue after Deposition	91
2.50 MS spectrum of $\text{Co}(\text{NTMS}_2)(\text{P}^t\text{Bu}^i\text{Pr})$	92
2.51 MS spectrum of $\text{Co}(\text{NTMS}_2)(\text{P}^t\text{Bu}^i\text{Pr})$	92
2.52 Employed Tantalum containing precursors for TaS_x deposition.	93
2.53 EDX spectrum of a TaS film.	94
2.54 HRRBS data of different deposition parameters aimin for Ta deposition.	95
2.55 Profilometry spectra of 300 and 600 ALD cycles of TaS at 130 °C.	97
2.56 AFM image of TaS_xO_x	97
2.57 SEM image of a TaS film showing debonding of the film.	99
3.1 Room temperature heat capacities compared with literature values	102
4.1 Scheme of in situ analysis in Reactor1.	106
4.2 Characterisation methods utilized in this thesis.	108
5.1 Scheme of the Reactor1 with illustration of the special position wafer.	120

List of Schemes

1.4.1 Mechanism of cobalt ALD with primary amines	35
2.1.1 Schematic drawing of the flow conditions.	37

List of Tables

2.1	Comparisment of prepared and best literature Ir material.	63
2.2	Comparisment of prepared and literature Pt material.	68
2.3	RAT assays and their properties.	81
2.4	Elemental analysis of filled compound 8 and 8 after ALD-Experiment.	90
2.5	Elemental analysis of the precursor bottle (bubbler) reminders.	98
4.1	Source of chemicals.	118
5.1	Platinum properties.	122
5.2	Iridium film properties.	124
5.3	Platinum properties.	125
5.4	Iridium film properties.	127
5.5	Platinum properties.	129
5.6	Platinum properties.	130
5.7	Platinum properties.	131
5.8	Tantalum sulfide properties.	134
5.9	Tantalum sulfide properties.	137
6.1	Chemicals with reference number	144

Bibliography

- [1] E. Ahvenniemi, A. R. Akbashev, S. Ali, M. Bechelany, M. Berdova, S. Boyadjiev, D. C. Cameron, R. Chen, M. Chubarov, V. Cremers, A. Devi, V. Drozd, L. Elnikova, G. Gottardi, K. Grigoras, D. M. Hausmann, C. S. Hwang, S.-H. Jen, T. Kallio, J. Kanervo, I. Khmel'nitskiy, D. H. Kim, L. Klibanov, Y. Koshtyal, A. O. I. Krause, J. Kuhs, I. Kärkkäinen, M.-L. Kääriäinen, T. Kääriäinen, L. Lammagna, A. A. Łapicki, M. Leskelä, H. Lipsanen, J. Lyytinen, A. Malkov, A. Malygin, A. Mennad, C. Militzer, J. Molarius, M. Norek, Ç. Özgit-Akgün, M. Panov, H. Pedersen, F. Pierrat, G. Popov, R. L. Puurunen, G. Rampelberg, R. H. A. Ras, E. Rauwel, F. Roozeboom, T. Sajavaara, H. Salami, H. Savin, N. Schneider, T. E. Seidel, J. Sundqvist, D. B. Suyatin, T. Törndahl, J. R. van Ommen, C. Wiemer, O. M. E. Ylivaara, O. Yurkevich, *Journal of Vacuum Science & Technology A: Vacuum, Surfaces, and Films* **2017**, 35(1), 010801.
- [2] R. W. Johnson, A. Hultqvist, S. F. Bent, *Materials Today* **2014**, 17(5), 236–246.
- [3] R. L. Puurunen, *Chem. Vap. Depos.* **2014**, 20(10-12), 332–344.
- [4] J. Suntola, T.; Antson, *International patent* **1977**, FIN 52359, US 4058430(5), 1–9.
- [5] V. B. Aleskovskii, S. I. Koltsov, *Abstract of Scientific and Technical Conference, Goskhimizdat, Leningrad* **1965**, 67.
- [6] C. Guan, J. Wang, *Advanced Science* **2016**, 3(10), 1–23.

- [7] J. Niinistö, K. Kukli, M. Heikkilä, M. Ritala, M. Leskelä, *Advanced Engineering Materials* **2009**, *11*(4), 223–234.
- [8] N. P. Dasgupta, H.-B.-R. Lee, S. F. Bent, P. S. Weiss, *Chemistry of Materials* **2016**, *28*(7), 1943–1947.
- [9] M. Bechelany, S. Balme, P. Miele, *Pure and Applied Chemistry* **2015**, *87*(8), 751–758.
- [10] N. Cheng, Y. Shao, J. Liu, X. Sun, *Nano Energy* **2016**, *29*, 220 – 242, electrocatalysis.
- [11] S. P. Jiang, P. K. Shen, *Nanostructured and Advanced Materials for Fuel Cells*, CRC Press, Boca Raton, London, New York, **2014**, p. 249–289.
- [12] W. Niu, X. Li, S. K. Karuturi, D. W. Fam, H. Fan, S. Shrestha, L. H. Wong, A. I. Y. Tok, *Nanotechnology* **2015**, *26*(6), 064001.
- [13] H. Van Bui, F. Grillo, J. R. van Ommen, *Chem. Commun.* **2017**, *53*(1), 45–71.
- [14] H. C. Guo, E. Ye, Z. Li, M.-Y. Han, X. J. Loh, *Materials Science and Engineering: C* **2017**, *70*, 1182–1191.
- [15] R. L. Puurunen, *Journal of Applied Physics* **2005**, *97*, 121301.
- [16] V. Miikkulainen, M. Leskelä, M. Ritala, R. L. Puurunen, *Journal of Applied Physics* **2013**, *113*(2).
- [17] M. Ritala, J. Niinistö, *Chemical Vapor Deposition* **2009**, 158–206.
- [18] K. Bernal, M. J. Saly, Y. J. Chabal, *Coordination Chemistry Reviews* **2013**, *257*(23-24), 3271–3281.
- [19] M. S. T. Suntola, *Atomic Layer Epitaxy*, Chapman and Hall, New York, **1990**.
- [20] M. Ritala, M. Leskelä, J. Dekker, C. Mutsaers, P. J. Soininen, J. Skarp, *Chem. Vap. Depos.* **1999**, *5*(1), 7–9.

- [21] R. Mueller, H. K. Kammler, K. Wegner, S. E. Pratsinis, *Langmuir* **2003**, *19*(1), 160–165.
- [22] S. E. Koponen, P. G. Gordon, S. T. Barry, *Polyhedron* **2016**, *108*(August), 59–66.
- [23] J. S. Ponraj, G. Attolini, M. Bosi, *Critical Reviews in Solid State and Materials Sciences* **2013**, *38*(3), 203–233.
- [24] S. M. George, *Chem. Rev.* **2010**, *110*(1), 111–131.
- [25] T. J. Knisley, L. C. Kalutarage, C. H. Winter, *Coord. Chem. Rev.* **2013**, *257*(23–24), 3222–3231.
- [26] J. Hämäläinen, M. Ritala, M. Leskelä, *Chem. Mater.* **2014**, *26*(1), 786–801.
- [27] F. Munnik, M. Ritala, M. Leskela, *Chem. Mater.* **2008**, *20*(9), 6840–6846.
- [28] C. A. Hoover, *ECS Transactions* **2006**, *1*(10), 95–101.
- [29] T. Gougousi, *Progress in Crystal Growth and Characterization of Materials* **2016**, *62*(4), 1 – 21, special Issue: Recent Progress on Fundamentals and Applications of Crystal Growth; Proceedings of the 16th International Summer School on Crystal Growth (ISSCG-16).
- [30] N. P. Dasgupta, X. Meng, J. W. Elam, A. B. F. Martinson, *Accounts of Chemical Research* **2015**, *48*(2), 341–348.
- [31] F. C. Frank, J. H. van der Merwe, *Proceedings of the Royal Society of London. Series A, Mathematical and Physical Sciences* **1949**, *198*(1053), 205–216.
- [32] F. C. Frank, J. H. van der Merwe, *Proceedings of the Royal Society of London. Series A, Mathematical and Physical Sciences* **1949**, *198*(1053), 216–225.
- [33] F. C. Frank, J. H. van der Merwe, *Proceedings of the Royal Society of London. Series A, Mathematical and Physical Sciences* **1949**, *200*(1060), 125–134.

- [34] W. F. a. Besling, E. Young, T. Conard, C. Zhao, R. Carter, *Journal of Non-Crystalline Solids* **2002**, *303*, 123–133.
- [35] Z. A. Sechrist, F. H. Fabreguette, O. Heintz, T. M. Phung, D. C. Johnson, S. M. George, *Chemistry of Materials* **2005**, *17*(13), 3475–3485.
- [36] G. S. Higashi, C. G. Fleming, *Appl. Phys. Lett.* **1989**, *55*(19), 1963.
- [37] M. Leskelä, M. Ritala, *Thin Solid Films* **2002**, *409*(1), 138–146.
- [38] M. Leskelä, L. Niinisto, T. Suntola, M. Simpson, *Atomic Layer Epitaxy*, Blackie, Glasgow, **1990**.
- [39] N. Pinna, M. Knez, *Atomic Layer Deposition of Nanostructured Materials*, Wiley-VCH Verlag, **2012**.
- [40] S. D. Elliott, *Langmuir* **2010**, *26*(12), 9179–9182.
- [41] J. Geng, D. Haehnel, *Womag* **2013**, 1–4.
- [42] T. Aaltonen, P. Alen, M. Ritala, M. Leskelä, *Chem. Vap. Depos.* **2003**, *9*(1), 45–49.
- [43] T. Aaltonen, M. Ritala, K. Arstila, J. Keinonen, M. Leskelä, *Chem. Vap. Depos.* **2004**, *10*(4), 215–219.
- [44] H. Wang, R. G. Gordon, R. Alvis, R. M. Ulfing, *Chem. Vap. Depos.* **2009**, *15*(10-12), 312–319.
- [45] T. Aaltonen, M. Ritala, M. Leskelä, *Electrochem. Solid-State Lett.* **2005**, *8*(8), C99.
- [46] J. Hämäläinen, T. Sajavaara, E. Puukilainen, M. Ritala, M. Leskelä, *Chem. Mater.* **2012**.
- [47] T. Aaltonen, M. Ritala, V. Sammelselg, M. Leskelä, *J. Electrochem. Soc.* **2004**, *151*(8), G489.

- [48] J. Hämäläinen, E. Puukilainen, M. Kemell, L. Costelle, M. Ritala, M. Leskelä, *Chemistry of Materials* **2009**, 21(20), 4868–4872.
- [49] T. Aaltonen, M. Ritala, T. Sajavaara, , J. Keinonen, M. Leskelä, *Chem. Mater.* **2003**, 15(17), 1924–1928.
- [50] J. P. Klesko, M. M. Kerrigan, C. H. Winter, *Chem. Mater.* **2016**, 8–11.
- [51] A. W. M. Volmer, *Z. Phys. Chem.* **1926**, 119, 277–301.
- [52] I. J. Hsu, B. E. McCandless, C. Weiland, B. G. Willis, *J. Vac. Sci. Technol. A Vacuum, Surfaces, Film.* **2009**, 27(4), 660–667.
- [53] Z. Lia, R. G. Gordona, D. B. Farmerb, Y. Linb, J. Vlassakb, *Electrochem. Solid-State Lett.* **2005**, 8, G182–G185.
- [54] Q. Ma, H. Guo, R. G. Gordon, F. Zaera, *Chem. Mater.* **2011**, 23(14), 3325–3334.
- [55] R. Solanki, B. Pathangey, *Electrochem. Solid-State Lett.* **2000**, 3(10), 479–480.
- [56] B. H. Lee, J. K. Hwang, J. W. Nam, S. U. Lee, J. T. Kim, S. M. Koo, A. Baunemann, R. A. Fischer, M. M. Sung, *Angew. Chemie - Int. Ed.* **2009**, 48(25), 4536–4539.
- [57] G. Dey, S. D. Elliott, *J. Phys. Chem. A* **2012**, 116(35), 8893–8901.
- [58] T. J. Knisley, T. C. Ariyasena, T. Sajavaara, M. J. Saly, C. H. Winter, *Chem. Mater.* **2011**, 23(20), 4417–4419.
- [59] B. Vidjayacoumar, D. J. H. Emslie, S. B. Clendenning, J. M. Blackwell, J. F. Britten, A. Rheingold, *Chem. Mater.* **2010**, 22(17), 4844–4853.
- [60] J. Chae, H.-S. Park, S.-w. Kang, *Electrochem. Solid-State Lett.* **2002**, 5(6), C64.

- [61] K.-W. Do, C.-M. Yang, I.-S. Kang, K.-M. Kim, K.-H. Back, H.-I. Cho, H.-B. Lee, S.-H. Kong, S.-H. Hahm, D.-H. Kwon, J.-H. Lee, J.-H. Lee, *Japanese Journal of Applied Physics* **2006**, 45(4S), 2975.
- [62] B. Lim, A. Rahtu, R. G. Gordon, *Nat. Mater.* **2003**, 2(Nov.), 749–754.
- [63] J.-M. Kim, H.-B.-R. Lee, C. Lansalot, C. Dussarrat, J. Gatineau, H. Kim, *Japanese Journal of Applied Physics* **2010**, 49(5S2), 05FA10.
- [64] K. Kim, K. Lee, S. Han, T. Park, Y. Lee, J. Kim, S. Yeom, H. Jeon, *Japanese Journal of Applied Physics* **2007**, 46(3L), L173.
- [65] H. Sun, X. Qin, F. Zaera, *J. Phys. Chem. Lett.* **2011**, 2(20), 2525–2530.
- [66] X. Qin, H. Sun, F. Zaera, *J. Vac. Sci. Technol. A Vacuum, Surfaces, Film.* **2012**, 30(1), 01A112.
- [67] S. M. Rossnagel, A. Sherman, F. Turner, *J. Vac. Sci. Technol. B Microelectron. Nanom. Struct.* **2000**, 18(4), 2016–2020.
- [68] S. O. Kucheyev, J. Biener, T. F. Baumann, Y. M. Wang, A. V. Hamza, Z. Li, D. K. Lee, R. G. Gordon, *Langmuir* **2008**, 24(3), 943–948.
- [69] D.-Y. Moon, D.-S. Han, J.-H. Park, S.-Y. Shin, J.-W. Park, B. M. Kim, J. Y. Cho, *Thin Solid Films* **2012**, 521, 146–149.
- [70] H. Kim, *Surf. Coatings Technol.* **2006**, 200(10), 3104–3111.
- [71] J. Huo, R. Solanki, J. McAndrew, *J. Mater. Res.* **2002**, 17(09), 2394–2398.
- [72] Z. Li, R. G. Gordon, *Chem. Vap. Depos.* **2006**, 12(7), 435–441.
- [73] T. Waechtler, S.-F. Ding, L. Hofmann, R. Mothes, Q. Xie, S. Oswald, C. Detavernier, S. E. Schulz, X.-P. Qu, H. Lang, T. Gessner, *Microelectronic Engineering* **2011**, 88(5), 684 – 689, the 2010 International workshop on “Materials for Advanced Metallization” - {MAM}.

- [74] S. M. Geyer, R. Methaapanon, B. Shong, P. A. Pianetta, S. F. Bent, *J. Phys. Chem. Lett.* **2013**, 4(1), 176–179.
- [75] W. M. M. Kessels, H. C. M. Knoop, S. A. F. Dielissen, A. J. M. MacKus, M. C. M. Van De Sanden, *Appl. Phys. Lett.* **2009**, 95(1), 1–4.
- [76] A. J. M. MacKus, N. Leick, L. Baker, W. M. M. Kessels, *Chem. Mater.* **2012**, 24(10), 1752–1761.
- [77] R. H. E. C. Bosch, F. L. Bloksma, J. M. M. Huijs, M. A. Verheijen, W. M. M. Kessels, *J. Phys. Chem. C* **2016**, 120(1), 750–755.
- [78] I. J. M. Erkens, A. J. M. Mackus, H. C. M. Knoop, P. Smits, T. H. M. van de Ven, F. Roozeboom, W. M. M. Kessels, *ECS J. Solid State Sci. Technol.* **2012**, 1(6), P255–P262.
- [79] T. Aaltonen, A. Rahtu, M. Ritala, M. Leskellä, *Electrochem. Solid-State Lett.* **2003**, 6(9), C130.
- [80] T. Aaltonen, M. Ritala, *J. Mater. Res.* **2004**, 19(11).
- [81] S. T. Christensen, J. W. Elam, *Chem. Mater.* **2010**, 22(8), 2517–2525.
- [82] M. Filez, H. Poelman, R. K. Ramachandran, J. Dendooven, K. Devloo-Casier, E. Fonda, C. Detavernier, G. B. Marin, *Catal. Today* **2014**, 229, 2–13.
- [83] J. Hämäläinen, F. Munnik, M. Ritala, M. Leskelä, *Chem. Mater.* **2008**, 21(20), 6840–6846.
- [84] J. Hamalainen, E. Puukilainen, M. Sajavaara, Timo; Ritala, M. Leskela, *Thin Solid Films* **2013**, 531, 243–250.
- [85] D. Löffler, T. Adermann, W. Hagen, *Cooperation Kick-off meeting* **2015**.
- [86] R. G. Charles, P. G. Haverlack, *J. inorg. nucl. Chem.* **1969**, 31(1969), 995–1005.

- [87] H.-b.-r. Lee, H. Kim, *ECS Trans.* **2008**, *16*, 219–225.
- [88] H. B. R. Lee, W. H. Kim, J. W. Lee, J.-M. Kim, K. Heo, I. C. Hwang, Y. Park, S. Hong, H. Kim, *J. Electrochem. Soc.* **2010**, *157*, D10–D15.
- [89] H. B. R. Lee, J. Kim, H. Kim, W. H. Kim, J. W. Lee, I. Hwang, *J. Korean Phys. Soc.* **2010**, *56*, 104–107.
- [90] L. C. Kalutarage, P. D. Martin, M. J. Heeg, C. H. Winter, *J. Am. Chem. Soc.* **2013**, *135*, 12588–12591.
- [91] M. M. Kerrigan, J. P. Klesko, S. M. Rupich, C. L. Dezelah, R. K. Kanjolia, J. Yves, C. H. Winter, M. M. Kerrigan, J. P. Klesko, S. M. Rupich, C. L. Dezelah, R. K. Kanjolia, Y. J. Chabal, C. H. Winter, *The Journal of Chemical Physics* **2017**, *052813*.
- [92] I. Kovacs, F. Ungvary, L. Marko, *Organometallics* **1994**, *13*(9), 1927–1933.
- [93] H. A. Jun-ichi Nishizawa, T. Kurabayashi, *J. Electrochem. Soc.* **1985**, *132*(5), 1197–1200.
- [94] A. Ott, J. Klaus, J. Johnson, S. George, *Thin Solid Films* **1997**, *292*(1-2), 135–144.
- [95] O. Sneh, M. L. Wise, A. W. Ott, L. A. Okada, S. M. George, *Surf. Sci.* **1995**, *334*(1-3), 135–152.
- [96] T. Suntola, J. Antson, *In: Handbook of Crystal Growth Part B: Growth Mechanisms and Dynamics, Chapter 14: Atomic Layer Epitaxy.* , Bd. 3, Elsevier, Amsterdam, **1994**.
- [97] J. I. Skarp, P. J. Soininen, P. T. Soininen, *Appl. Surf. Sci.* **1997**, *112*(0), 251–254.
- [98] M. Juppo, A. Rahtu, M. Ritala, M. Leskelä, *Langmuir* **2000**, *16*(8), 4034–4039.

- [99] S. Dushman, *Scientific Foundations of Vacuum Technique, 2nd ed.*, John Wiley and Sons, New York, **1962**.
- [100] A. Roth, *Vacuum Technology, 2nd, Revised Edition*, Elsevier Ltd, Amsterdam, **1986**.
- [101] A. Sommerfeld, *Proc. 4th Int. Congr. Math. III 1908*, 174(1883), 116–124.
- [102] C. Company, *Technical Paper 1988*, 410(TP 410).
- [103] O. Sneh, *U.S. Patent 2005*, 410(US 6,911,092 B2).
- [104] H. Kim, C. Cabral, C. Lavoie, S. M. Rossnagel, *J. Vac. Sci. Technol. B Microelectron. Nanom. Struct.* **2002**, 20(4), 1321.
- [105] S. B. S. Heil, J. L. van Hemmen, C. J. Hodson, N. Singh, J. H. Klootwijk, F. Roozeboom, M. C. M. van de Sanden, W. M. M. Kessels, *J. Vac. Sci. Technol. A Vacuum, Surfaces, Film.* **2007**, 25(5), 1357–1366.
- [106] D. K. Nandi, U. K. Sen, A. Dhara, S. Mitra, S. K. Sarkar, *RSC Adv.* **2016**, 6(44), 38024–38032.
- [107] M. S. Weimer, R. F. McCarthy, J. D. Emery, M. J. Bedzyk, F. G. Sen, A. Kinaci, M. K. Chan, A. S. Hock, A. B. Martinson, *Chem. Mater.* **2017**, 29(7), 2864–2873.
- [108] L. Lamagna, C. Wiemer, M. Perego, S. Spiga, J. Rodríguez, D. Santiago Coll, M. E. Grillo, S. Klejna, S. D. Elliott, *Chem. Mater.* **2012**, 24(6), 1080–1090.
- [109] Y. Zheng, S. Hong, G. M. Psafogiannakis, G. B. Rayner, Jr., S. Datta, A. C. van Duin, R. Engel-Herbert, *ACS Appl. Mater. Interfaces* **2017**, acsami.7b01618.
- [110] S. Y. Lee, C. Jeon, S. H. Kim, Y. Kim, W. Jung, K.-S. An, C.-Y. Park, *Japanese Journal of Applied Physics* **2012**, 51(3R), 031102.

- [111] R. Zhao, Y. Gao, Z. Guo, Y. Su, X. Wang, *ACS Appl. Mater. Interfaces* **2017**, 9(2), 1885–1890.
- [112] E. Levrau, K. Devloo-Casier, J. Dendooven, K. F. Ludwig, P. Verdonck, J. Meersschat, M. R. Baklanov, C. Detavernier, *Langmuir* **2013**, 29(39), 12284–9.
- [113] M. Tallarida, D. Schmeisser, *Semicond. Sci. Technol.* **2012**, 27(7), 074010.
- [114] E. Janocha, A. Hofmann, C. Pettenkofer, *Radiation Physics and Chemistry* **2013**, 93, 72 – 76, proceedings of the 11th International School and Symposium on Synchrotron Radiation in Natural Science (ISSRNS).
- [115] S.-J. Park, W.-H. Kim, W. Maeng, Y. Yang, C. Park, H. Kim, K.-N. Lee, S.-W. Jung, W. Seong, *Thin Solid Films* **2008**, 516(21), 7345 – 7349.
- [116] J. A. Klug, M. S. Weimer, J. D. Emery, A. Yanguas-Gil, S. Seifert, C. M. Schlepütz, A. B. F. Martinson, J. W. Elam, A. S. Hock, T. Proslie, *Rev. Sci. Instrum.* **2015**, 86(11), 113901–1–11.
- [117] K. Devloo-Casier, K. F. Ludwig, C. Detavernier, J. Dendooven, *J. Vac. Sci. Technol. A Vacuum, Surfaces, Film.* **2014**, 32(1), 010801.
- [118] M. Schuisky, J. W. Elam, S. M. George, *Appl. Phys. Lett.* **2002**, 81(1), 180–182.
- [119] T. D. Gould, A. M. Lubers, A. R. Corpuz, A. W. Weimer, J. L. Falconer, J. W. Medlin, *ACS Catal.* **2015**, 5(2), 1344–1352.
- [120] A. J. M. Mackus, C. Macisaac, W. H. Kim, S. F. Bent, *J. Chem. Phys.* **2017**, 146(5).
- [121] J. W. DuMont, S. M. George, *J. Chem. Phys.* **2017**, 146(5).
- [122] J. W. DuMont, S. M. George, *J. Phys. Chem. C* **2015**, 119(26), 14603–14612.

- [123] S. Masango, P. C. Stair, R. P. Van Duyne, *Abstracts of Papers, 250th ACS National Meeting & Exposition, Conference; Meeting Abstract; Online Computer File* **2015**, PHYS-454.
- [124] M. Kaipio, T. Blanquart, Y. Tomczak, J. Niinistö, M. Gavagnin, V. Longo, H. D. Wanzenböck, V. R. Pallem, C. Dussarrat, E. Puukilainen, M. Ritala, M. Leskelä, *Langmuir* **2014**, *30*(25), 7395–404.
- [125] J. T. Tanskanen, C. Hagglund, S. F. Bent, *Chem. Mater.* **2014**, *26*(9), 2795–2802.
- [126] D. Longrie, D. Deduytsche, J. Haemers, K. Driesen, C. Detavernier, *Surf. Coatings Technol.* **2012**, *213*, 183–191.
- [127] O. Nilsen, H. Fjellvåg, *J. Therm. Anal. Calorim.* **2011**, *105*(1), 33–37.
- [128] G. Fang, L. Xu, Y. Cao, A. Li, *Coordination Chemistry Reviews* **2016**, *322*, 94–103.
- [129] T. Ahmido, W. A. Kimes, B. A. Sperling, J. T. Hodges, J. E. Maslar, *J. Vac. Sci. Technol. A Vacuum, Surfaces, Film.* **2016**, *34*(3), 031512.
- [130] G. J. Snyder, E. S. Toberer, *Nat. Mater.* **2008**, *7*(2), 105–114.
- [131] K. Biswas, J. He, I. D. Blum, Chun-IWu, T. P. Hogan, D. N. Seidman, V. P. Dravid, M. G. Kanatzidis, *Nature* **2012**, *490*(7421), 570–570.
- [132] B. Tian, X. Zheng, T. J. Kempa, Y. Fang, N. Yu, G. Yu, J. Huang, C. M. Lieber, *Nature* **2007**, *449*(7164), 885–889.
- [133] B. C. Steele, *Nature* **2001**, *414*(414), 345–352.
- [134] N. P. Padture, *Science* **2002**, *296*(5566), 280–284.
- [135] R. M. Costescu, D. G. Cahill, F. H. Fabreguette, Z. A. Sechrist, S. M. George, *Science* **2004**, *303*(5660), 989–990.

- [136] M. Maldovan, *Nat. Mater.* **2015**, *14*(7), 667–674.
- [137] J. A. Johnson, A. A. Maznev, J. Cuffe, J. K. Eliason, A. J. Minnich, T. Kehoe, C. M. S. Torres, G. Chen, K. A. Nelson, *Physical Review Letters* **2013**, *110*(2), 1–5.
- [138] M. Zebarjadi, K. Esfarjani, M. S. Dresselhaus, Z. F. Ren, G. Chen, *Energy Environ. Sci.* **2012**, *5*(1), 5147–5162.
- [139] C. J. Vineis, A. Shakouri, A. Majumdar, M. G. Kanatzidis, *Adv. Mater.* **2010**, *22*(36), 3970–3980.
- [140] D. G. Cahill, P. V. Braun, G. Chen, D. R. Clarke, S. Fan, K. E. Goodson, P. Keblinski, W. P. King, G. D. Mahan, A. Majumdar, H. J. Maris, S. R. Phillpot, E. Pop, L. Shi, *Appl. Phys. Rev.* **2014**, *1*(1).
- [141] C. Kittel, *Introduction to Solid State Physics (Eighth Edition)*, John Wiley & Sons, **2005**.
- [142] J. Ravichandran, A. K. Yadav, R. Cheaito, P. B. Rossen, A. Soukiassian, S. J. Suresha, J. C. Duda, B. M. Foley, C.-H. Lee, Y. Zhu, A. W. Lichtenberger, J. E. Moore, D. A. Muller, D. G. Schlom, P. E. Hopkins, A. Majumdar, R. Ramesh, M. A. Zurbuchen, *Nat. Mater.* **2013**, *13*(2), 168–172.
- [143] C. Gang, *Nanoscale Energy Transport and Conversion: A Parallel Treatment of Electrons, Molecules, Phonons, and Photons.*, Oxford, New York: Oxford University, **2005**.
- [144] C. Dames, G. Chen, *Thermoelectrics Handbook: Macro to Nano (ed. Rowe, D.) Ch. 42*, CRC Press, New York, **2005**.
- [145] H. Budd, J. Vannimenus, *Physical Review Letters* **1971**, *26*(26).
- [146] E. T. Swartz, R. O. Pohl, *Reviews of Modern Physics* **1989**, *61*(3), 605–668.

- [147] I. Khalatnikov, *An Introduction to the Theory of Superfluidity*, Benjamin, New York, **1965**.
- [148] D. A. Young, H. J. Maris, *Physical Review B* **1989**, *40*(6), 3685–3693.
- [149] S. Pettersson, G. D. Mahan, *Physical Review B* **1990**, *42*(12), 7386–7390.
- [150] B. N. J. Persson, H. Ueba, *Journal of Physics: Condensed Matter* **2010**, *22*(46), 462201.
- [151] A. M. Schwartzberg, D. Olynick, *Advanced Materials* **2015**, *27*(38), 5778–5784.
- [152] Y. K. Koh, Y. Cao, D. G. Cahill, D. Jena, *Advanced Functional Materials* **2009**, *19*(4), 610–615.
- [153] P. Hyldgaard, G. D. Mahan, *Physical Review B* **1997**, *56*(17), 10754–10757.
- [154] M. V. Simkin, G. D. Mahan, *Phys. Rev. Lett.* **2000**, *84*(5), 927–930.
- [155] B. K. Ridley, *Physical Review B* **1994**, *49*(24), 17253–17258.
- [156] A. A. Kiselev, K. W. Kim, M. A. Strosio, *Physical Review B - Condensed Matter and Materials Physics* **2000**, *62*(11), 6896–6899.
- [157] S. Y. Ren, J. D. Dow, *Journal of Chemical Information and Modeling* **1982**, *25*(6), 3750.
- [158] S. Chakraborty, C. A. Kleint, A. Heinrich, C. M. Schneider, J. Schumann, M. Falke, S. Teichert, *Applied Physics Letters* **2003**, *83*(20), 4184–4186.
- [159] S.-M. Lee, D. G. Cahill, R. Venkatasubramanian, *Applied Physics Letters* **1997**, *70*(22), 2957–2959.
- [160] K. Esfarjani, G. Chen, H. T. Stokes, *Phys. Rev. B - Condens. Matter Mater. Phys.* **2011**, *84*(8), 1–11.

- [161] E. L. T. Martin Maldovan, *Periodic Materials and Interference Lithography: For Photonics, Phononics and Mechanics*, Wiley-VCH, Weinheim, Germany, **2008**.
- [162] B. C. Gundrum, D. G. Cahill, R. S. Averback, *Phys. Rev. B* **2005**, *72*, 1–5.
- [163] R. B. Wilson, D. G. Cahill, *Physical Review Letters* **2012**, *108*(25), 1–5.
- [164] V. Rawat, Y. K. Koh, D. G. Cahill, T. D. Sands, V. Rawat, K. Koh, D. G. Cahill, T. D. Sands, *Journal of Applied Physics* **2009**, *105*, 1–7 (024909).
- [165] F. Döring, *Dissertation* **2016**.
- [166] J. H. Bechtel, *Journal of Applied Physics* **1975**, *46*(4), 1585–1593.
- [167] R. Wolfe, *Proceedings of the Physical Society. Section A* **1955**, *68*(2), 121–127.
- [168] D. Guidotti, J. G. Wilman, *Applied Physics Letters* **1992**, *60*(5), 524–526.
- [169] L. Schnieder, K. Seekamp-Rahn, F. Liedeker, H. Steuwe, K. H. Welge, *Faraday Discussions of the Chemical Society* **1991**, *91*, 259.
- [170] N. Bartels, K. Golibrzuch, C. Bartels, L. Chen, D. J. Auerbach, A. M. Wodtke, T. Schäfer, *Proceedings of the National Academy of Sciences* **2013**, *110*(44), 17738–17743.
- [171] B. C. Krüger, S. Meyer, A. Kandratsenka, A. M. Wodtke, T. Schäfer, *Journal of Physical Chemistry Letters* **2016**, *7*(3), 441–446.
- [172] N. Bartels, T. Schäfer, J. Hühnert, R. W. Field, A. M. Wodtke, *Journal of Chemical Physics* **2012**, *136*(21).
- [173] Y. Huang, C. T. Rettner, D. J. Auerbach, A. M. Wodtke, *Science* **2000**, *290*(5489), 111–114.

- [174] O. Bünermann, H. Jiang, Y. Dorenkamp, A. Kandratsenka, S. M. Janke, D. J. Auerbach, A. M. Wodtke, *Science* **2015**, *350*(6266), 1346–1349.
- [175] A. Amirav, M. J. Cardillo, *Physical Review Letters* **1986**, *57*(18), 2299–2302.
- [176] J. K. Nørskov, B. I. Lundqvist, *Surface Science* **1979**, *89*(1-3), 251–261.
- [177] G. Ertl, *Angewandte Chemie - International Edition* **2008**, *47*(19), 3524–3535.
- [178] E. S. Peters, C. J. Carmalt, I. P. Parkin, D. A. Tocher, *European Journal of Inorganic Chemistry* **2005**, *20*(20), 4179–4185.
- [179] A. B. Kaul, *Journal of Materials Research* **2014**, *29*(03), 348–361.
- [180] H. G. Kim, H.-B.-R. Lee, *Chemistry of Materials* **2017**, *29*(9), 3809–3826.
- [181] S. Das, M. Kim, J.-w. Lee, W. Choi, *Critical Reviews in Solid State and Materials Sciences* **2014**, *39*(4), 231–252.
- [182] K. S. Novoselov, D. Jiang, F. Schedin, T. J. Booth, V. V. Khotkevich, S. V. Morozov, A. K. Geim, *Proceedings of the National Academy of Sciences* **2005**, *102*(30), 10451–10453.
- [183] M. Bosi, *RSC Advances* **2015**, *5*(92), 75500–75518.
- [184] P. Sekar, E. C. Greyson, J. E. Barton, T. W. Odom, *Journal of the American Chemical Society* **2005**, *127*, 2054–2055.
- [185] X. Wang, H. Feng, Y. Wu, L. Jiao, *Journal of the American Chemical Society* **2013**, *135*(14), 5304–5307.
- [186] S. Cadot, O. Renault, M. Frégnaux, D. Rouchon, E. Nolot, K. Szeto, C. Thieuleux, L. Veyre, H. Okuno, F. Martin, E. A. Quadrelli, *Nanoscale* **2016**, *00*(2), 1–3.
- [187] P. Sun, W. Zhang, X. Hu, L. Yuan, Y. Huang, *Journal of Materials Chemistry A* **2014**, *2*(10), 3498.

- [188] Q. Xiang, J. Yu, M. Jaroniec, *Journal of the American Chemical Society* **2012**, *134*, 6575–6578.
- [189] Y. Yan, B. Xia, Z. Xu, X. Wang, *ACS Catalysis* **2014**, *4*, 1693–1705.
- [190] B. J. O'Neill, D. H. K. Jackson, J. Lee, C. Canlas, P. C. Stair, C. L. Marshall, J. W. Elam, T. F. Kuech, J. A. Dumesic, G. W. Huber, *ACS Catalysis* **2015**, *5*(3), 1804–1825.
- [191] J. Lu, J. W. Elam, P. C. Stair, *Surface Science Reports* **2016**, *71*(2), 410–472.
- [192] S. Nagata, T. Aochi, T. Abe, S. Ebisu, T. Hagino, Y. Seki, K. Tsutsumi, *Journal of Physics and Chemistry of Solids* **1992**, *53*(10), 1259–1263.
- [193] S. Mathias, S. Eich, J. Urbancic, S. Michael, A. V. Carr, S. Emmerich, A. Stange, T. Popmintchev, T. Rohwer, M. Wiesenmayer, A. Ruffing, S. Jakobs, S. Hellmann, P. Matyba, C. Chen, L. Kipp, M. Bauer, H. C. Kapteyn, H. C. Schneider, K. Rossnagel, M. M. Murnane, M. Aeschlimann, *Nature Communications* **2016**, *7*, 12902.
- [194] S. Eich, M. Plötzing, M. Rollinger, S. Emmerich, R. Adam, C. Chen, H. C. Kapteyn, M. M. Murnane, L. Plucinski, D. Steil, B. Stadtmüller, M. Cinchetti, M. Aeschlimann, C. M. Schneider, S. Mathias, *Science Advances* **2017**, *3*(March), 1602094.
- [195] L. Karvonen, A. Säynätjoki, M. Roussey, M. Kuittinen, S. Honkanen, *Opto-electronic Devices and Materials* **2014**, *1–10*, 89880Z.
- [196] A. Ruge, J. S. Park, R. G. Gordon, S. H. Tolbert, *Journal of Physical Chemistry B* **2005**, *109*(9), 3764–3771.
- [197] H. P. Latscha, G. Schilling, H. A. Klein, *Chemie-Datensammlung, 2. Auflage*, Springer Verlag, **1993**.

- [198] W. Georgi, E. Metin, *Einführung in LabVIEW (5., überarbeitete und erweiterte Auflage)*, Carl Hanser Verlag, München, **2012**.
- [199] B. Mütterlein, *Handbuch für die Programmierung mit LabVIEW: mit Studentenversion LabVIEW 2009*, Spektrum Akademischer Verlag, Heidelberg, **2009**.
- [200] W. Shen, B. Fang, Y. Zhang, C. Yang, W. Yuan, K. Mao, R. Fan, *Chinese Patent* **2016**, CN 105349962(2016:310567), 1–10.
- [201] C. Henkel, S. Abermann, O. Bethge, E. Bertagnolli, *Semicond. Sci. Technol.* **2009**, 24(24), 125013–6.
- [202] M. S. McConnell, L. C. Schneider, G. Karbasian, S. Rouvimov, A. O. Orlov, G. L. Snider, *J. Vac. Sci. Technol. A Vacuum, Surfaces, Film.* **2016**, 34(1), 01A139.
- [203] W.-S. Jeon, S. Yang, C.-s. Lee, S.-W. Kang, *J. Electrochem. Soc.* **2002**, 149(6), C306.
- [204] Y. Xiong, L. Sang, Q. Chen, L. Yang, Z. Wang, Z. Liu, *Plasma Sci. Technol.* **2013**, 15(1), 52–55.
- [205] D. Bell, A. Garratt-Reed, *Energy Dispersive X-ray Analysis in the Electron Microscope*, Garland Science, Oxford, **2003**.
- [206] A. K. Vannucci, L. Alibabaei, M. D. Losego, J. J. Concepcion, B. Kalanyan, G. N. Parsons, T. J. Meyer, *Proc. Natl. Acad. Sci. U. S. A.* **2013**, 110, 20918–20922.
- [207] A. M. Lapidés, B. D. Sherman, M. K. Brennaman, C. J. Dares, K. R. Skinner, J. L. Templeton, T. J. Meyer, *Chem. Sci.* **2015**, 6(11), 6398–6406.
- [208] T. Aaltonen, M. Ritala, V. Sammelselg, M. Leskelä, *J. Electrochem. Soc.* **2004**, 151(8), G489–G492.

- [209] B. A. Macklin, J. C. Withers, *Proc. Conf. Chem. Vapor Deposition Refract. Metals, Alloys, Compounds* **1967**, -(), 161–173.
- [210] S. Yang, X. Yu, C. Tan, Y. Wang, H. Ma, K. Liu, H. Cai, *Applied Surface Science* **2015**, 329, 248–255.
- [211] H. C. M. Knoop, A. J. M. Mackus, M. E. Donders, M. C. M. van de Sanden, P. H. L. Notten, W. M. M. Kessels, *Electrochemical and Solid State Letters* **2009**, 12(7), G34–G36.
- [212] F. Döring, C. Volkmann, S. Schneider, *unpublished results* **2016, 2017**.
- [213] H. U. Krebs, O. Bremert, *Appl. Phys. Lett.* **1993**, 62(19), 2341–2343.
- [214] H.-U. Krebs, M. Weisheit, J. Faupel, E. Süske, T. Scharf, C. S. M. Fuhse, K. Sturm, M. Seibt, H. Kijewski, D. Nelke, E. Panchenko, M. Buback, *Pulsed Laser Deposition (PLD) – A Versatile Thin Film Technique. In: Advances in Solid State Physics.*, Springer, Berlin, Heidelberg, **2003**, p. 505–518.
- [215] B. L. Wang, J. C. Han, S. Y. Du, *Journal of Thermal Stresses* **2000**, 23, 143–168.
- [216] B. Y. Terada, K. Ohkubo, T. Mohri, *Platinum Metals Rev* **2005**, 49(1), 21–26.
- [217] V. A. Korshunov, *Soviet Physics Journal* **1980**, 22(8), 903–905.
- [218] Y. Wang, J. J. Wang, W. Y. Wang, Z. G. Mei, S. L. Shang, L. Q. Chen, Z. K. Liu, *Journal of Physics: Condensed Matter* **2010**, 22(20), 1–5 (202201).
- [219] J. Maris, R. Stoner, *Physical Review B* **1993**, 48(22), 16373–16387.
- [220] G. McGuire, *Auger Electron Spectroscopy Reference Manual, A Book of Standard Spectra for Identification and Interpretation of Auger Electron Spectroscopy Data*, Springer US, New York, **1979**, p. 4, 10, 16, 125.

- [221] Y. Dorenkamp, *unpublished results, (presented within the scope of the work group seminar)* **2017**.
- [222] L. Kochanneck, *Bachelorthesis* **2015**.
- [223] T. Münch, *Bachelorthesis* **2017**.
- [224] K. E. Goodson, *Science* **2007**, 315(5810), 342–343.
- [225] S. Tanuma, *Surface and Interface Analysis* **2006**, 38, 178–180.
- [226] M. P. Seah, I. S. Gilmore, S. J. Spencer, *J. Electron Spectrosc.* **2001**, 120, 93–111.
- [227] G. L. A., *Introduction to focused ion beams*, Springer Science and Business Media, Inc., Boston, **2005**.
- [228] K. Kanaya, S. Okayama, *Journal of Physics D, Applied Physics* **1972**, 5, 43–58.
- [229] W. K. D. Y. Smith, Mitio Inokuti, *Journal of Physics: Condensed Matter* **2001**, 13(17), 3883—3893.
- [230] C. Borschel, M. Schnell, C. Ronning, H. Hofsäss, *Nuclear Instruments and Methods in Physics Research, Section B: Beam Interactions with Materials and Atoms* **2009**, 267(8-9), 1737–1739.
- [231] M. Uhrmacher, H. Hofsäss, *Nuclear Instruments and Methods in Physics Research, Section B: Beam Interactions with Materials and Atoms* **2005**, 240(1-2), 48–54.
- [232] K. Oura, V. Lifshits, A. Saranin, A. Zotov, M. Katayama, *Surface Science, An Introduction*, Springer, Berlin, Heidelberg, **2003**.
- [233] L. E. Davis, *Handbook of Auger Electron Spectroscopy, 2nd edition*, Physical Electronics Industries, Inc., Eden Prairie, Minnesota, **1976**.

[234] R. Piedras, *Vacuum* **1990**, 41(7-9), 1605–1607.

[235] G. M. Sheldrick, *Acta Cryst.* **2015**, A71(9), 3–8.

6.2 List of Scientific Contributions

6.2.1 Patents

"Process for the Generation of Thin Inorganic Films" T. Adermann, D. Loeffler, H. Wilmer, K. Schierle-Arndt, J. Gerken, C. Volkmann, S. Schneider, *WO2017093283* (A1), 2017.

6.2.2 Publications in Scientific Journals

"Inelastic H-Atom Scattering from Ultrathin Aluminum Oxide Films Grown by Atomic Layer Deposition", Y. J. Dorenkamp, C. Volkmann, V. Roddatis, S. Schneider, A. M. Wodtke, O. Bünermann, manuscript in progress.

"Four- and Five-coordinate Osmium(IV) Nitrides and Imides: Circumventing the 'Nitrido-Wall'", J. Abbenseth, S. Bete, M. Finger, C. Volkmann, C. Würtele, S. Schneider, *Organometallics*, **2017**, tba.

"Dinitrogen Splitting Coupled to Protonation" G. A. Silantsev, M. Förster, B. Schluschaß, J. Abbenseth, C. Würtele, C. Volkmann, M. C. Holthausen, S. Schneider, *Angew. Chem. Int. Ed.*, **2017**, *56*, 5872-5876; *Angew. Chem.* **2017**, *129*, 5966-5970.

"A Square-Planar Osmium(II) Complex" J. Abbenseth, M. Diefenbach, S. C. Bete, C. Würtele, C. Volkmann, S. Demeshko, M. C. Holthausen, S. Schneider, *Chem. Commun.* **2017**, *53*, 5511-5514.

"A Terminal Osmium(IV) Nitride: Ammonia Formation and Ambiphilic Reactivity." F. S. Schendzielorz, M. Finger, C. Volkmann, C. Würtele, S. Schneider, *Angew. Chem. Int. Ed.* **2016**, *55*, 11417-11420.

"On the temperature dependence of H-U iso in the riding hydrogen model" J. Luebben, C. Volkmann, S. Grabowsky, A. Edwards, W. Morgenroth, F. P. A. Fabbiani, G. M. Sheldrick, B. Dittrich, *Acta Cryst. A*, **2014**, *70(4)*, 309-316.

6.2.3 Oral Contributions to Conferences and Workshops

"ALD in a nutshell", CRC 1073, Graduiertenkolleg, Göttingen, 23.05.14.

"Verhalten von dreifach koordinierten Cobaltkomplexen im ALD-Versuch", Ludwigshafen
20.07.2015.

"A04 - Controlling surface energy dissipation via tailored interface properties: Atomic
Layer Deposition", CRC 1073 Annual Meeting, 18.02.2015, Drübeck.

"Overview of the Material Section of the CRC 1073", Graduate School Meeting,
Berlin, 2016.

6.2.4 Poster Presentations on Conferences

Christian Volkmann, Sven Schneider, "Special Interface Properties via Atomic Layer Deposition", CRC 1073 Kick-off Meeting, Göttingen, 2013.

Christian Volkmann, Sven Schneider, "Special interface properties via Atomic Layer Deposition, Material Design and Synthesis", San Sebastian, Interfaces2014, 2014.

Christian Volkmann, Sven Schneider, "Special interface properties via Atomic Layer Deposition, 17. Vortragstagung für Anorganische Chemie (Wöhler-Vereinigung), Saarbrücken, 2014.

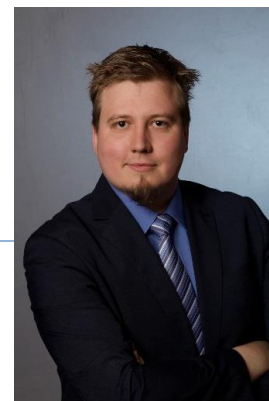
Christian Volkmann, Sven Schneider, "Controlling Surface energy dissipation via tailored interface properties", CRC 1073 Annual Meeting, Drübeck, 2015.

Christian Volkmann, Sven Schneider, "Atomic Layer Deposition: A Manifold Tool for Tailored Interfaces", 4th Lower Saxony Catalysis Symposium (NIKAS), Braunschweig, 2016.

Alec Wodtke, Sven Schneider, Oliver Bünermann, "Controlling Surface energy dissipation via tailored interface properties, Atomic Layer Deposition", Second funding phase CRC 1073, Göttingen, 2017.

6.3 Curriculum Vitae

Christian Volkmann
Ginsterweg 6 | 37077 Göttingen | Deutschland
Tel. 0171-1160669 | E-Mail: Christian.Volkmann@chemie.uni-goettingen.de



Curriculum Vitae

Personal Data

Date of birth	July 03, 1987
Place of birth	Halle, Westf.
Nationality	German
Address	Ginsterweg 6, 37077 Göttingen

Professional Experience

Since 02.2013

PHD student at the University of Göttingen

Institute of Inorganic Chemistry, CRC1073, Prof. Schneider

Project: "Atomic layer deposition of metal and metal chalcogenide thin films and nanolaminate composites"

- Setting up a novel ALD reactor (Hard- and Software)
- Phonon blocking structures using Al_2O_3 and Pt ALD
- Cobalt deposition with novel $\text{Co}(\text{NTMS}_2)_2\text{PR}_3$ precursor (BASF)
- Tantalum sulfide deposition for heterogeneous catalysis

05.2012 – 11.2012

Master Thesis

Institute of Inorganic Chemistry, Prof. Sheldrick/Dr. Dittrich

Project: "ONIOM cluster calculations on displacement parameter temperature dependency on N-Acetyl-(2S,4R)-4-Hydroxyproline Monohydrate at 9, 30, 50 and 67 K"

- Calculation using Gaussian, various basis sets and Hirshfeld refinement
- Interpretation of vibrational calculation to physical displacement
- Comparing theoretical with synchrotron data
- Automatization programming, Website responsibility

11.2011 – 03.2015

Bachelor Thesis

Institute of Inorganic Chemistry, Prof. Stalke

Project: "C3-Symmetrische Iminophosphanliganden mit Heterocyclen zur Synthese von heterometallischen Komplexen"

- Synthesis of air and moisture sensitive compounds
- Crystallization for single crystal X-Ray studies

Christian Volkmann
Ginsterweg 6 | 37077 Göttingen | Deutschland
Tel. 0171-1160669 | E-Mail: Christian.Volkmann@chemie.uni-goettingen.de

Academic Education

Since 02.2013	PhD student at the University of Göttingen Thesis title: "Atomic layer deposition of metal and metal chalcogenide thin films and nanolaminate composites"
10.2010 – 11.2012	MSc student at the University of Göttingen Thesis title: "ONIOM cluster calculations on displacement parameter temperature dependency on N-Acetyl-(2S,4R)-4-Hydroxyproline Monohydrate at 9, 30, 50 and 67 K"
10.2007 – 10.2010	B.Sc. student at the University of Göttingen Thesis title: "C3-Symmetrische Iminophosphanliganden mit Heterocyclen zur Synthese von heterometallischen Komplexen"
08.1998 – 05.2007	grammar school
07.1994 – 05.1998	elementary school

Key Skills and Competencies

Expertise	Atomic Layer Deposition (Reactor setup, deposition, theory), precursor design and evaluation, inorganic and organic syntheses; analytical and physical chemistry; air-free techniques (Schlenk line and glove box); scientific writing, computational chemistry
Methods	AFM, STM, XRR, XRD(powder and single crystal), TEM, (FIB-)SEM, EDX, LEED, XPS, Auger-spectroscopy, QMB, Profilometry, NMR, Ellipsometry, UV/Vis spectroscopy, (<i>in situ</i> -)mass-spectrometry, schlenk techniques, crystallization.
Languages	English (fluent) German (mother tongue) Latin (basic knowledge) Sign language (basic knowledge) HTML5 and LabView (advanced user)
Computer Skills	LaTeX, MS Office (Word, Excel, PowerPoint), ChemOffice, Origin, MestReNova, HTML5, Python, Gaussian, LabView, ShelXle, Gwyddion, DigitalMicrograph, SciFinder, Mendeley.

Christian Volkmann
Ginsterweg 6 | 37077 Göttingen | Deutschland
Tel. 0171-1160669 | E-Mail: Christian.Volkmann@chemie.uni-goettingen.de

Internships

06.2013, 08.2013, **Visiting student at the University Erlangen**
Institute of Chemie und Pharmazie, Prof. Dr. Julien Bachmann

- Ir and Pt ALD in commercial and self-build no-flow ALD reactor
- Thin gold films via sputter deposition

Social commitment

12.2013 – 02.2015 head of the post graduate programme of the CRC1073
06.2014 – today refugees integration, e.g. “*Physik für Flüchtlinge*”[link](#), weekly meetings
2004-2007 advisor in Teutolab: chemistry for elementary students[link](#)
2003-2007 head of the badminton AG
Prestudy youth leader in SK Halle 1946 e.V.[link](#) and 1. Haller Sportfischerverein e.V.[link](#)

References

Prof. Dr. Sven Schneider Institute of Inorganic Chemistry • University of Göttingen
Tammannstr. 4 • 37077 Göttingen
Tel. 0551 39 22829 • Email: sven.schneider@chemie.uni-goettingen.de

Christian Volkmann, Göttingen, 18.08.2017